Remote Sensing of Atmospheric Water Vapor with the Global Positioning System

A Dissertation

John Joseph Braun

B. A., University of Colorado, 1991

M. S., University of Colorado, 1997

A thesis submitted to the

Faculty of the Graduate School of the

University of Colorado in partial fulfillment

of the requirements for the degree of

Doctor of Philosophy

Department of Aerospace Engineering Sciences

2004

This thesis entitled:
Remote Sensing of Atmospheric Water Vapor with the Global Positioning System

Written by John Joseph Braun
Has been approved for the Department of Aerospace Engineering Sciences.

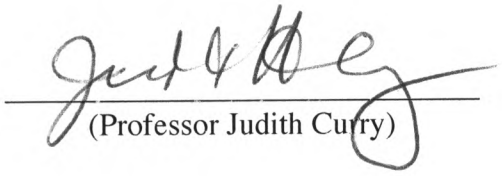

(Professor Judith Curry)

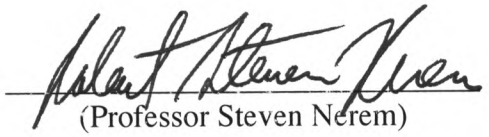

(Professor Steven Nerem)

Date:_____

The final copy of this thesis has been examined by the signatories, and we find that both the content and the form meet acceptable presentation standards of scholarly work in the above mentioned discipline.

Abstract

Braun, John Joseph (Ph. D., Aerospace Engineering Sciences)
Remote Sensing of Atmospheric Water Vapor with the Global Positioning System
Thesis directed by Professor Judith Curry

Signals from the Global Positioning System (GPS) are used to retrieve the integrated amount of water vapor along the path between a transmitting satellite and a receiving station. This integrated quantity is called slant water vapor (SW). Measurements of SW allow for an improved assessment of the spatial distribution of water vapor within the atmosphere. This technique is developed and validated through simulations and comparisons to similar measurements from a pointing microwave water vapor radiometer. Absolute accuracy of zenith scaled SW is found to be 1.5 mm with a relative precision that is better than 0.5 mm. Dual and single frequency GPS stations are used to measure SW. Previously, only dual frequency GPS stations have been used for atmospheric remote sensing. The use of single frequency stations, which are significantly less expensive than dual frequency ones, allows for a denser placement of stations. The effects of the ionosphere on single frequency GPS observations are eliminated using global ionosphere models and double difference processing with short station separation. Networks of GPS stations are deployed in the Southern Great Plains of the United States. Combining SW measurements from all stations within a dense network allows for an estimation of the three dimensional distribution of water vapor above the network. This tomographic technique is improved by including vertical profiles from radiosondes. The retrieval of SW is utilized during the International H_20 Project 2002 (IHOP_2002). Significant water vapor structure is observed within the atmospheric boundary layer, including dryline convergence and horizontal convective rolls. Tomography results computed during squall line passage indicate elevated levels of water vapor in the free troposphere prior to the onset of rainfall. A statistical analysis of the results obtained during IHOP_2002 show coherent water vapor structure across horizontal lengths ranging from less than 1 to almost 100 kilometers. A significant diurnal cycle of atmospheric water vapor variability is also found.

Dedication

To Stephanie, Jackson and Riley.

Acknowledgements

This research was supported through a graduate student fellowship from the Advanced Study Program at the National Center for Atmospheric Research (NCAR); and by the Biological and Environmental Research Program (BER), U. S. Department of Energy Grant DE-FG03-02ER63327.

Various people and groups supplied data that were used in this research. Joel Van Baelen at Centre National de la Recherché Scientifique (CNRS), France provided data from GPS stations deployed by CNRS during the International H_20 Project 2002 (IHOP_2002). Meteorological data were obtained from the Atmospheric Radiation Measurement (ARM) Program sponsored by the U.S. Department of Energy, Office of Science, Office of Biological and Environmental Research, Environmental Sciences Division. Surface meteorological data during IHOP_2002 were used from the Oklahoma Mesonet Network.

Victoria Andreatta and Chuck Kurnik at the University NAVSTAR Consortium (UNAVCO) helped deploy the single frequency GPS stations. Their work was greatly appreciated. "Corky," Fred Mack, and Sandy Mack assisted in contacting farmers, station installation, station maintenance, and the use of their farm as a base of operations was invaluable. The members of the "L1" team at UNAVCO deserve recognition for their help in building and testing the single frequency GPS stations. This included Dr. Chuck Meertens, Dr. Lou Estey, Dave Mencin, and Curt Conquest.

The thesis committee of Dr. Judith Curry, Dr. Steve Nerem, Dr. Kristine Larson, Dr. Peter Molnar, Dr. Christian Rocken, and Dr. Bill Kuo provided useful comments and questions about this research. Their input was greatly appreciated. In particular, Dr. Rocken and Dr. Kuo offered insightful analysis throughout the project.

The researchers in the COSMIC program also deserve recognition for their critique and support of this research. This group includes Stick Ware, Jim Johnson, Teresa Van Hove, So-Young Ha, Doug Hunt and Bill Schreiner.

The majority of the figures were created with the Generic Mapping Tools (GMT) software package [*Wessel and Smith*, 1998].

Contents

Remote Sensing of Atmospheric Water Vapor with the Global Positioning System i
Abstract iii
Dedication iv
Acknowledgements v
Contents vi
List of Tables viii
List of Figures ix
Chapter 1: Introduction 1
1.1 The Significance of Water Vapor in the Atmosphere 1
1.2 Previous Research 1
1.3 Scientific Achievements from this Research 2
1.4 Thesis Organization 3
Chapter 2: Atmospheric Water Vapor 5
2.1 The Need for Improved Observational Techniques 5
2.2 Water Vapor Within the Boundary Layer 5
2.3 Moisture and Convection 6
2.4 Temporal and Spatial Variability of Water Vapor 7
2.5 Chapter Summary 9
Chapter 3: The Global Positioning System 10
3.1 Overview 10
3.2 Satellite Constellation 10
3.3 GPS Signals and Observations 11
3.4 International GPS Service 13
3.5 Observation Equation 15
3.6 Linear Combinations of Observations 15
3.7 Differences of Observations 16
3.8 GPS Analysis Software 17
3.9 Other GNSS Systems 19
Chapter 4: Slant Water Vapor 20
4.1 Overview 20
4.2 The Neutral Atmosphere and GPS 20
4.3 Scaling ZWD to PW 23
4.4 Slant Water Vapor Retrieval 24
4.5 Simulation Experiment 29
4.6 Slant Water Vapor Experiment - Platteville, CO 39
4.7 Slant Water Vapor Experiment - Lamont, OK 41
4.8 Chapter Summary 43
Chapter 5: Single Frequency GPS Stations 45
5.1 Overview 45
5.2 System Components 45
5.2.1 GPS Receiver 46
5.2.2 GPS Antenna 48
5.2.3 Radio Modem 51

5.2.4 Power/Battery Backup 52
5.3 CMC Receiver Performance 53
5.4 Processing Strategy 55
5.5 Network Deployment 57
5.6 Geodetic Results 58
5.7 Atmospheric Results 60
5.8 Ionospheric Error 61
Chapter 6: Tomography of the Atmosphere 63
6.1 Overview 63
6.2 The Inverse Problem 63
6.3 Horizontal Constraints 66
6.4 Improvement of the Vertical Profile 69
6.5 Solution Using Constraints 72
6.6 Simulation 72
6.7 Sequential Estimation 75
Chapter 7: The International H_20 Project (IHOP_2002) 77
7.1 Overview 77
7.2 GPS Network 77
7.3 Boundary Layer Structures – the Dryline 78
7.3.1 May 22, 2002 79
7.3.2 May 30, 2002 85
7.4 Boundary Layer Structures – Horizontal Convective Rolls 91
7.5 Spatial Correlation of SW and S_i^k 96
7.6 Diurnal Evolution of the Boundary Layer 100
7.7 Tomography Solutions 102
7.7.1 Squall Line – June 12, 2002 103
7.7.2 Nested Tomography – June 12, 2002 108
7.7.3 Tomography Solutions – Comparison to Raman Lidar 111
Chapter 8: Conclusions 114
8.1 Summary 114
8.2 Discussion 116
Bibliography 119
Appendix 1 124
Appendix 2 125

List of Tables

Table 1: GPS Satellite Constellation Characteristics 11
Table 2: GPS Signal Characteristics..... 11
Table 3: IGS Derived Data Products 14
Table 4: Significant Components of Single Frequency GPS Stations 45

List of Figures

Figure 1: Map of "global" IGS stations (http://igscb.jpl.nasa.gov) 14
Figure 2: Diagram of processing steps in the computation of GPS SW 28
Figure 3: Model output fields used in the SW simulation – pressure and temperature (top), precipitable water (middle), hourly accumulation of rainfall (bottom) 30
Figure 4: Simulated, zenith scaled, hydrostatic delay (lower), wet delay (middle), and total delay (upper). Each color represents a different satellite. 32
Figure 5: Simulated delays for station NDSK 33
Figure 6: The network of stations used in the SW simulation. Red diamonds represent stations within the 3-km domain. Black diamonds represent stations in the 25-km domain 34
Figure 7: Comparison of Simulated SWD (red) and retrieved SWD (blue) for station LMNO. 35
Figure 8: Simulated SWD (red) and retrieved SWD (blue) for station PRCO 35
Figure 9: Individual satellite traces for LMNO. Simulated SW plotted as the thinner red line. Retrieved SWD plotted as the thinner blue line. Half hour averages of simulated zenith scaled SWD are shown as red dots. Half-hour ZWD estimates are shown as blue dots. 36
Figure 10: Individual satellite traces for station PRCO. The labeling is the same as Figure 9. 37
Figure 11: Linear correlation of simulated SWD against retrieved ZWD (black) and retrieved SWD (red). The error in the ZWD estimate has been removed in the retrieved SWD. 39
Figure 12: SW signal, GPS measurement noise, and MWR measurement noise plotted as a function of satellite elevation angle. Figure originally from Braun et al. 2001 41
Figure 13: GPS antenna (left) and MWR (right) collocated at ARM Central Facility 42
Figure 14: Examples of retrieved SW from Braun 2003 et al. 43
Figure 15: Single frequency GPS stations operating in north-central Oklahoma. The station on the right continued operation after being vandalized with a shotgun. 46
Figure 16: Zero difference residuals from single frequency receiver. The 50-point running standard deviation is plotted as the red line. 47
Figure 17: Zero difference residuals from dual frequency receiver. The 50-point running standard deviation is plotted as the red line. 48
Figure 18: Signal-to-Noise (SNR) values in dBm for Micropulse patch antenna without multipath suppression 50
Figure 19: SNR values in dBm of Micropulse antenna with rolled edge ground plane. 50
Figure 20: Data collection statistics for station 1N1W 52
Figure 21: Diagram of baseline formation using single frequency stations (green) and dual frequency stations (red). 57
Figure 22: Map of single frequency GPS stations (black diamonds) relative to ARM SGP central facility (red star). 58
Figure 23: Time series of coordinate solutions for single frequency station 0N1E. 59

Figure 24: Time series of coordinate solutions for single frequency station 2N2W...60
Figure 25: Scatter plot of dual frequency SW vs. single frequency SW collected during IHOP_2002.....61
Figure 26: Scatter plot of zero difference residuals from a single frequency station and the rate of change of the ionosphere.....62
Figure 27: Cartoon representation approximating SW measurement within voxels...65
Figure 28: Graphical representation of the number of different stations containing a ray path passing through each voxel.....67
Figure 29: A ground based GPS station would measure the same integrated SW for a homogeneous layer of water vapor located at any height.....69
Figure 30: Improvement in Vertical Profile Using Additional Information.....71
Figure 31: Scatter plot (left) of simulated vs. retrieved densities for each voxel. Density plotted as function of altitude (right) for simulated (black) and retrieved (red) values.....74
Figure 32: Simulated (left) and retrieved (right) water vapor fields for layer from ground level to 0.5 km.....74
Figure 33: Simulated (left) and retrieved (right) water vapor fields between 1.5 and 2.0 km altitude.....75
Figure 34: GPS stations in the Southern Great Plains region during the IHOP_2002 experiment.....78
Figure 35: Surface conditions from the Oklahoma Mesonet at 21:30 UTC (4:30 CST) on May 22, 2002.....81
Figure 36: S-Pol surface refractivity field at 2145 UTC (4:45 CST) on May 22, 2002. The location of the GPS station is shown as the red star.....81
Figure 37: Time-height cross section of water vapor mixing ratio as measured by the GSFC scanning Raman Lidar on May 22, 2002.....82
Figure 38: Vertically scaled GPS SW (blue diamonds) from the Oklahoma panhandle station SA14. The half hour GPS PW estimates are in red.....82
Figure 39: Zenith scaled SW from station SA14 to satellite 3 is shown in red. The average of all zenith scaled SW is plotted in black. The satellite azimuth and elevation is plotted in the small sky plot in the lower left corner.....83
Figure 40: Zenith scaled SW from station SA14 to satellite 9. The data in the plot are represented in the same manner as Figure 39.....83
Figure 41: Zenith scaled SW from station SA14 to satellite 29. The data in the plot are represented in the same manner as Figure 39.....84
Figure 42: S-Pol surface refractivity field at 2245 UTC (5:45 CST) on May 22, 2002. The location of the GPS station is shown as the red star. As satellite 29 set, it passed through the moist cell identified with the red arrow.....85
Figure 43: GOES-8 visible imagery at 1 km resolution on 30/May/2002 at 1908 UTC. 87
Figure 44: GOES-8 visible imagery at 1 km resolution on 30/May/2002 at 2233 UTC. Small cumulus clouds had formed along the dryline running southwest to northeast through the Oklahoma panhandle.....88
Figure 45: Time-height cross section of water vapor mixing ratio as measured by the GSFC scanning Raman Lidar on May 30, 2002.....89

Figure 46: GPS PW (red diamonds) and zenith scaled SW (blue diamonds) at the SA14 station located in the panhandle of Oklahoma. 89
Figure 47: Zenith scaled SW from station SA14 to satellite 3 on May 30, 2002. The data in the plot are represented in the same manner as Figure 39. 90
Figure 48: Zenith scaled SW from station SA14 to satellite 15. The data in the plot are represented in the same manner as Figure 39. 90
Figure 49: Comparisons of GPS (red) and MWR (blue) from Braun et al 2003 paper. The top panel plots the S_i^k component of SW, the lower panel plots zenith scaled SW. 92
Figure 50: GOES-8 visible imagery at 1 km resolution on June 9, 2002 at 2039 UTC. Horizontal convective rolls exist over large sections of Oklahoma. 93
Figure 51: Surface conditions from the Oklahoma Mesonet at 2030 UTC (3:30 CST) on June 9, 2002. 94
Figure 52: GPS PW (red diamonds) and zenith scaled SW (blue diamonds) station SG01 on June 9, 2002. 94
Figure 53: Zenith scaled SW from station SG01 to satellite 15 on June 9, 2002. The data in the plot are represented in the same manner as Figure 39. 95
Figure 54: Zenith scaled SW from station SG01 to satellite 18 on June 9, 2002. The data in the plot are represented in the same manner as Figure 39. 96
Figure 55: Linear correlation of SW (bottom) and S_i^k (top) as a function of station separation for May 23, 2002 98
Figure 56: Linear correlation of SW (bottom) and S_i^k (top) as a function of station separation for May 31, 2002 99
Figure 57: Diurnal variation in the non-isotropic component of SW (S_i^k) for Lamont, OK during the IHOP_2002 campaign 101
Figure 58: Diurnal variation in the non-isotropic component of SW (S_i^k) for Oklahoma Panhandle station SA14 during IHOP_2002. 102
Figure 59: Composite WSR-88D radar reflectivity on June 12, 2002 at 1200 UTC (top) and 1300 UTC (bottom) 105
Figure 60: Interpolated maps of 30-minute PW estimates on June 12, 2002 beginning at 1200 UTC (top) and 1330 UTC (bottom). The stations used in the interpolation are shown as diamonds. 106
Figure 61: Surface meteorological observations (top panel) and GPS derived water vapor amounts (bottom panel) for station BURB on June 12, 2002. In the top panel the surface temperature is in red, the dew point temperature in blue, accumulated rain is plotted in black and the wind speed and direction is plotted using the vectors at the top. In the bottom panel the GPS PW are the red diamonds and the zenith scale SW are the blue diamonds 107
Figure 62: Surface meteorological observations (top) and time-height profile of water vapor density (bottom) for station BURB on June 12, 2002 108
Figure 63: Graphical representation of the number of different stations containing a ray path passing through each voxel. 110
Figure 64: Time vs. height profile of water vapor density using a nested tomography domain and 500 m vertical resolution 111

Figure 65: Time and height cross-section of water vapor density measured by the ARM Raman Lidar. The vertical resolution of the Lidar has been smoothed to match the 1 km resolution of the tomography..... 112
Figure 66: Time and height cross-section of tomography solution above ARM CF. 113

Chapter 1: Introduction

1.1 The Significance of Water Vapor in the Atmosphere

Water, in its three phases, is a foundation for life on Earth. The transitions of water from one phase to another regulate the temperature of the Earth's surface making it hospitable for mankind. The global transport of water acts to redistribute energy around the world and is a driving force in its climate and weather system. The research presented here improves the characterization of one component of the Earth's hydrological cycle, atmospheric water vapor.

Water vapor is both the most abundant and most variable green house gas in the atmosphere. It affects the Earth's radiation budget, energy transfer, cloud formation, and precipitation distribution. For radiation transfer, water vapor absorbs both downwelling solar and upwelling longwave radiation. For energy transfer, the latent heat of evaporation is a principal path for the transport of energy from the equator to higher latitudes. The energy released when vapor condenses to form clouds affects the dynamics of the atmosphere. Through this interaction, the vertical stability of the atmosphere is modified, influencing weather systems and their associated precipitation patterns.

While being such a key element in the atmosphere, accurate measurements of water vapor are not readily available. Improving and expanding the techniques to measure water vapor has been identified as a key area of research by the U.S. Weather Research Program [*Dabberdt and Schlatter*, 1996; *Emanuel*, 1996]. The lack of detailed and accurate measurements hinders our ability to model and predict the Earth's climate and forecast weather.

1.2 Previous Research

The Global Positioning System (GPS) provides a relatively inexpensive method to remotely sense atmospheric water vapor in all weather conditions. Initial investigations focused on the measurement of the vertically integrated amount of

water vapor as observed by a ground based GPS station [*Bevis et al.*, 1992; *Rocken et al.*, 1991; *Rocken et al.*, 1995]. Vertically integrated water vapor is commonly termed precipitable water vapor (PW). GPS methods to remotely sense PW are now well developed and the technique has been implemented in an operational mode [*Hagemann et al.*, 2003; *Ohtani and Naito*, 2000; *Rocken et al.*, 1997; *Wolfe and Gutman*, 2000].

GPS PW has been used to investigate the accuracy of moisture fields in numerical weather models [*Haase et al.*, 2003]. GPS PW has also been directly assimilated into models to improve their predictive capability [*Cucurull et al.*, 2004; *De Pondeca and Zou*, 2001; *Kuo et al.*, 1993; *Kuo et al.*, 1996]. Additionally, continuous time series of GPS PW are now being used to detect and quantify spatial and temporal variations in water vapor on seasonal and diurnal time scales [*Dai et al.*, 2002; *Hagemann et al.*, 2003].

1.3 Scientific Achievements from this Research

There are three significant achievements presented in this thesis. First, a new technique to measure atmospheric water vapor is developed. This technique measures the integrated amount of water vapor along the path between a transmitting GPS satellite and a receiving antenna. This integral, termed slant water vapor (SW) differs from PW in that it quantifies the amount of water vapor in a specific direction. While PW is a column average of atmospheric water vapor over both space and time, SW provides an instantaneous measurement to individual satellites visible from a station and therefore provides an improved sampling of the spatial distribution of atmospheric water vapor. The remote sensing technique used to obtain SW is described and verified through a simulation and comparisons to other instruments.

The second innovation is the use of single frequency GPS stations as atmospheric remote sensing instruments. These single frequency stations were developed, built, installed, and operated as part of this research. These stations are low cost and can be deployed in relatively large quantities to form a dense array. Special processing methods have been developed to minimize errors associated with the ionosphere. A network of stations is currently in operation in the Southern Great

Plains of the United States. Their primary purpose is to observe the variability of water vapor on horizontal scales of 1-2 km or less.

The third innovation is the combination of data collected from a network of GPS stations to derive the three dimensional distribution of water vapor with horizontal scales of less than 100 km and vertical scales of less than 1 km. SW measurements are combined into four-dimensional estimates of the water vapor field using tomographic inversion techniques. The spatial density of the stations allows for the resolution of mesoscale and microscale variations of the water vapor field.

The results presented were primarily obtained in the Southern Great Plains region of the Central United States. The variation and severity of the weather events in this area makes it an ideal test bed for evaluating new measurement techniques. The precise location is around the Department of Energy's (DOE) Atmospheric Radiation Measurements (ARM) Southern Great Plains (SGP) central facility near Lamont, OK. The meteorological instruments at this facility are used for validation and to provide constraints on the vertical structure of the atmosphere around the network. The results are primarily from instrument comparisons from the summer of 2000 and during the International H_20 Project in May and June of 2002 (IHOP_2002). The objective of IHOP_2002 was to characterize the water vapor field using state of the art instrumentation and quantify how useful these observations are in helping to improve warm season rainfall prediction, a forecast where numerical weather prediction lacks the most skill.

1.4 Thesis Organization

Following the introduction in this chapter, Chapter 2 outlines the need and application of GPS sensed water vapor observations. Chapter 3 describes the basics of GPS with an emphasis on the elements that are relevant to this research. Chapter 4 details the technique of retrieving SW from GPS, outlining a simulation experiment as well as a summary of two validation experiments which are more completely presented in Appendices 1 and 2. Chapter 5 describes the single frequency GPS stations that were developed. Chapter 6 presents the tomographic technique that was implemented. Chapter 7 presents a summary of results from the IHOP_2002

experiment. Finally, Chapter 8 summarizes this research and outlines areas of improvement and application for further studies.

Chapter 2: Atmospheric Water Vapor

2.1 The Need for Improved Observational Techniques

The primary goal of the research presented here is to improve the capability to measure atmospheric water vapor. This topic was discussed in the "NCAR-UCAR Lower Tropospheric Water Vapor Workshop" summarized by Weckwerth et al [1999]. The meeting highlighted the need for observations covering all time and space scales, temporally ranging from seconds to days and spatially varying from a few meters to hundreds of kilometers. There were six major recommendations contained within this summary. The research conducted in this thesis directly addresses two of the recommendations. (1) "*The community should explore ground-based tomography techniques for four- dimensional water vapor analyses.*" and (2) "*The community should develop a low-cost ($100,000 - $200,000), continuously operating, moderate resolution water vapor profiler to operate as part of a network.*" Areas of atmospheric research that were mentioned in the report that could benefit from the techniques developed here include boundary layer studies, atmospheric chemistry, climate, polar research, and numerical weather prediction (including precipitation, severe weather forecasts and convection initiation). This chapter reviews three fields of research in atmospheric science that benefit from this thesis.

2.2 Water Vapor Within the Boundary Layer

The boundary layer represents the lowest 1-3 km of the atmosphere and typically contains the majority of water vapor within the column. Moisture observations are not readily available within this region. Surface measurements are strongly related to land-air interactions and do not accurately represent the entire boundary layer, while conventional satellite sounding instruments do not work well at low altitudes. The boundary layer is most commonly measured using (1) ground based sounding instruments such as radiosondes and Lidars, (2) towers with meteorological sensors placed at various altitudes, and (3) in-situ aircraft

measurements. These techniques are all relatively expensive, and are not suitable for continuous monitoring over significant time and/or space scales. Detailed observations of boundary layer moisture are needed to validate and understand the processes that occur and how they affect the broader atmospheric system.

Horizontal convective rolls can be described as horizontal vortices whose spin axes are aligned with the boundary layer wind field [*Peckham et al.*, 2004; *Weckwerth et al.*, 1997]. They can have wavelengths of 2-10 km and initiate convection by concentrating and lifting water vapor within the boundary layer. Convective rolls have been directly observed with measurements from aircrafts, towers, and sounding instruments such as Lidars and radiosondes. Previous simulations and observational studies indicate that rolls can alter the water vapor mixing ratio by as much as 1-2.5 g/kg within the boundary layer. Under proper conditions, this increase can induce cloud formation and possibly convection.

The dryline, and it's strong influence on weather events has been discussed in numerous papers [*Hane et al.*, 1997; *McCarthy and Koch*, 1982; *Parsons et al.*, 1991; *Ziegler et al.*, 1997]. The dryline that commonly occurs in the Southern Great Plains is essentially a low level atmospheric boundary between dry air that undergoes adiabatic heating as it subsides from the Rocky Mountains and moist air that is advected north and west from the Gulf of Mexico. It is often times associated with intense convection and severe weather. The horizontal boundary of a dryline can vary in width between 2 and 20 km, and model analysis indicates it can be as deep as 4-5 km in areas where strong low-level convergence has occurred. Analysis of moisture variability of dryline events has mostly involved surface dew point measurements from surrounding mesonet stations and aircraft observations for specific experiments. In a numerical modeling study of three storms initiated along drylines [*Ziegler et al.*, 1997], mixing ratio variations of up to 8 g/kg over horizontal and vertical length scales of a few km were computed.

2.3 Moisture and Convection

Convection in the absence of external forcing is directly related to the convergence of moisture in the planetary boundary layer. This convergence of

moisture aids in the removal of convective inhibition (CIN) in a strict parcel lifting theory of convection. Xin and Reuter [1996] simulated a convective storm in the absence of vertical wind shear using an axisymetric model. The result of this simulation was to reveal that rainfall is controlled by the moisture convergence below clouds. They also showed that the timing and quantity of rainfall varied with the depth of the convergence zone, given a fixed vertical mass flux. This can be explained that for a given mass flux in the boundary layer, the moisture flux tends to be largest in the lowest levels of the convergence field. Shallow convergence zones injected more moisture above the level of free convection and subsequently increased the rainfall within the simulation. In another study of convection in the absence of larger scale forcing, Crook [1996] determined that once convection was well developed, the strength of the convection (defined as the maximum vertical velocity (w_{max})) was 2.5 times more sensitive to variations in moisture than temperature in the convective boundary layer.

Severe storm prediction is limited by moisture observations throughout the troposphere. Sensitivity studies [*Park and Droegemeier*, 1999; *Park and Droegemeier*, 2000] indicate that a lack of accurate observational moisture measurements throughout the troposphere limits the forecast of severe storms over time scales as short as 30 minutes. In these studies, a 1% variation in water vapor within and around a storm cell had a significant and measurable affect on storm intensity. It was also reported that the variation in water vapor above the convective boundary layer directly affected the entrainment and vertical velocity characteristics of the storm.

2.4 Temporal and Spatial Variability of Water Vapor

There is relatively little information available on the variability of water vapor over short time (shorter than a few hours) and spatial scales (smaller than a few hundreds of kilometers). Knowledge of realistic spatial and temporal variations of moisture allows climate and weather modelers to compare statistics of their simulated moisture fields to realistic observations. These comparisons are essential in quantifying how well the models perform.

Radiosondes, being the most frequently used platform to measure atmospheric water vapor, do not possess either the temporal or the spatial resolution to infer information about the state of the atmosphere smaller than synoptic scales. Satellites provide measurements of upper troposphere humidity [*Bates and Jackson*, 2001; *Soden*, 1998] and can continuously monitor the atmosphere, but do not have the spatial resolution to observe features smaller than a few tens of kilometers. Generally, the studies of small-scale atmospheric water vapor utilize either microwave water vapor radiometers (MWRs) or GPS estimates of total column water vapor. These studies mostly focus on the measurement of precipitable water (PW) measured in units of mm, relating the integrated amount of water vapor in a column of air to an equivalent column of liquid water.

The temporal structure of the atmosphere has been studied by Hogg et al., [1981] and Jarlemark et al., [1995]. Both studies tried to find a power structure relationship between PW variability and time ($S(\tau) = c\tau^{\alpha}$, where $S(\tau)$ is the variance and τ is the period), spanning time periods of up to one or two days. In both studies, they found that the exponential term that best fit the variability was very nearly one. They found a linear relationship between the magnitude of the PW variability and time. A similar analysis on the spatial structure of water vapor was conducted by Emardson et al. [1998]. Using the Swedish GPS network (SWEPOS), they studied the structure of water vapor variance over scales of 10 to 100's of km and fit the variance according to a power law ($S(r) = cr^{\alpha}$, where r is the distance between stations). As was the case for the temporal variations, the structure function that worked best was one that varied linearly with distance (instead of some type of geometric scaling). These results differ somewhat from theoretical results discussed by Treuhaft and Lanyi [1987]. In their research, they assumed that the water vapor field should behave according to Kolmogorov turbulence theory. This theory implies that the variability of the water vapor structure function should behave according to a 5/3-power law over time scales less than a few minutes and space scales shorter than 1 km and smoothly transition into a 2/3-power law variation as the time and length scales increase.

Studies by Rocken et al., [1991] and Davis et al., [1993] observed variations in the PW content by scanning the sky at various elevation and azimuth angles. These investigations involved the use of MWR instruments that were configured so that they would measure the equivalent amount of PW in predefined directions, normally taking measurements at a specific elevation angle, and then stepping through a series of azimuth angles to observe the sky variability. These studies found that there can be azimuthal asymmetries as large as 25% of the total PW measurement. In the paper by Davis et al., they utilized a radiometer that measured the equivalent amount of PW in 10° azimuth steps at an elevation angle of 30°. For one particular example, they observed 5 mm of azimuthal PW variability with a mean estimate of approximately 20 mm. Assuming that most of the water vapor was contained within the first 2 km of the atmosphere, and a scanning elevation angle of 30°, the 5 mm of variability was distributed over a diameter of approximately 7 km.

2.5 Chapter Summary

Improved measurements of water vapor are needed in many topics of atmospheric research. Multiple reports and prospectuses highlight this need. Boundary layer studies require water vapor measurements to quantify the moisture convergence associated with convective rolls and drylines. Studies of convection initiation and severe storms show that accurate water vapor measurements improve the intensity and onset forecasting of storms. A detailed spatial and temporal sampling of atmospheric water vapor allows for improved statistical description of moisture to help validate and improve atmospheric models. The results of the research conducted in this thesis improve the observational capabilities available for all these topics.

Chapter 3: The Global Positioning System

3.1 Overview

The Global Positioning System is the most widely used constellation of satellites within the broader definition of Global Navigation Satellite Systems (GNSS). The GPS constellation is a United States Department of Defense (DoD) satellite system whose primary mission is to provide timing and ranging information to military users. Military applications of GPS include troop tracking and missile guidance systems. Civilian applications of GPS technology include land surveying, vehicle guidance and control, as well as high precision science [*Herring*, 1996]. There are three components to the GPS system: a space segment (the satellite constellation), a control segment (the network of monitoring and tracking stations which are operated by the military), and a user segment. For the user segment, GPS is designed to be a passive system. There is no interaction from the user segment to the satellite or control segment and there can be an infinite number of users of the system. There are numerous books describing the concepts of GPS. Notable to this list are works by Hofmann-Wellenhof et al. [1992], Kaplan [1996] and Parkinson et al. [1996]. This chapter reviews the key components of GPS that are relevant to this research. Those interested in pursuing a more detailed description of GNSS systems should refer to one of the references in the bibliography.

3.2 Satellite Constellation

Originally designed to be a constellation of 24 satellites, distributed in six orbital planes with four satellites in each plane, the current constellation consists of 28 satellites within the original six orbital planes. The characteristics of the satellite constellation are shown in Table 1. A list of satellites and their relative location within the constellation is available from the URL: ftp://tycho.usno.navy.mil/pub/gps/gpsb2.txt.

The constellation was designed to provide a global distribution of satellites so that at least four would be visible from any location on Earth. This minimum geometry allows for a unique and independent triangulation for position and time determination. With the current distribution, users at mid-latitudes are typically able to track at least six satellites at any moment.

Table 1: GPS Satellite Constellation Characteristics

Number of Satellites	24 (planned), 28 (current)
Number of Orbital Planes	6
Satellites per Orbital Plane	4
Orbital Period	~12 Hours
Orbital Radius	~26,400 Km
Inclination	~55°
Eccentricity	~0.0

3.3 GPS Signals and Observations

GPS satellites can be considered to be orbiting atomic oscillators. The fundamental frequency (f_0) of these oscillators is 10.23 MHz and all GPS signals are derived from f_0. GPS transmits on two L-band frequencies, generally referred to as the L_1 (1575.2 MHz or ~19 cm) and L_2 (1227.6 MHz or ~24 cm) carrier frequencies. Two different pseudorandom codes are modulated on top of the carrier frequencies. The first code is the Clear Acquisition code (C/A-code), which is only modulated on the L_1 carrier. Users of C/A-code observations are primarily civilians. The second code, known as the precise code (P-code), is modulated on both carrier frequencies and can be encrypted so that only military users have access to the signal. When encrypted, it is called the Y-code. Advanced civilian GPS receivers are now able to provide Y-code measurements, although at reduced accuracy compared to military receivers. Table 2 lists the characteristics of the basic GPS signals.

Table 2: GPS Signal Characteristics

Observation Name	Frequency Multiplier	Frequency	Wavelength	Precision
C/A	$f_0/10$	1.23 MHz	300 m	~10 m
P1 (Y1), P2(Y2)	$1* f_0$	10.23 MHz	30 m	~3 m
L1	$154* f_0$	1.23 MHz	19.0 cm	~ 1-2 mm
L2	$120* f_0$	1227.60 MHz	24.4 cm	~1-2 mm

The measurements of the pseudorandom codes (C/A, P_1, and P_2) are measures of the travel time between the satellite and receiver. The GPS receiver generates its own copy of the pseudorandom code and compares it to the one arriving from the satellite. An autocorrelation function computes the time offset between the received pseudorandom code and the one generated by the receiver. This offset is a combination of the time for the signal to travel from the satellite to receiver and the mis-synchronization of the satellite and receiver clocks. These measurements are called pseudorange measurements. Pseudorange measurements typically have a precision on the order of 1-10 meters.

In addition to the pseudorange, the two GPS carrier frequencies (L_1 and L_2) can also be used to make a phase measurement. In this method, the receiver first removes the pseudorandom codes from the carrier phase and combines the received signal with one generated internally using a phase lock loop (PLL) algorithm. The carrier frequency from the transmitting satellite is shifted when it arrives at the receiving GPS antenna. This Doppler shift is caused by the movement of the satellite relative to the receiving station. The integration of the synthesized signal output from the PLL represents the range (distance) between the satellite and receiver. The precision of this measurement is on the order of 1-2 mm. There is an ambiguity in this precise measurement. The receiver is not able to determine the initial distance to the satellite, it is only able to account for the change in range relative to the moment it begins tracking. To utilize the carrier phase, this ambiguity must be estimated in the inversion of the observation equations to derive station position, atmospheric delay and other geophysical properties.

The choice of L-band frequencies makes GPS an all-weather instrument. The tracking characteristics of the system are not dependent on atmospheric conditions (there is no significant attenuation), but the signal is delayed and bent according to the index of refraction of the atmosphere. A careful analysis of the GPS observations allows for the determination this delay and bending. These methods are the basis of atmospheric remote sensing with GPS and will be discussed in more detail in Chapter 4.

3.4 International GPS Service

The International GPS Service (IGS) is a volunteer collection of research groups, mainly consisting of government agencies and participating universities. Their goal is to provide high quality data and products for use in high precision science applications. The key components of the IGS include a network of continuously operating GPS stations, data centers who collect and distribute data through the Internet, analysis centers who produce products based on data collected from the network, and a governing body (including working groups and a central bureau) to guide the development and progress of the IGS.

The IGS collects data from more than 360 stations worldwide. Of these stations, 130 are considered global stations. The IGS definition of a global station is one whose data is used by more than three analysis centers, with one of the centers being located on a different continent than the station. The list of global stations is a compromise between location, distribution with respect to other stations, the latency of the data availability, and other issues such as receiver tracking performance and monument stability. A map of the "global" stations is plotted in Figure 1. This network is the backbone of the IGS and is the basis for which it generates its products. Individual institutions voluntarily operate and contribute the data collected by their station to the IGS for analysis.

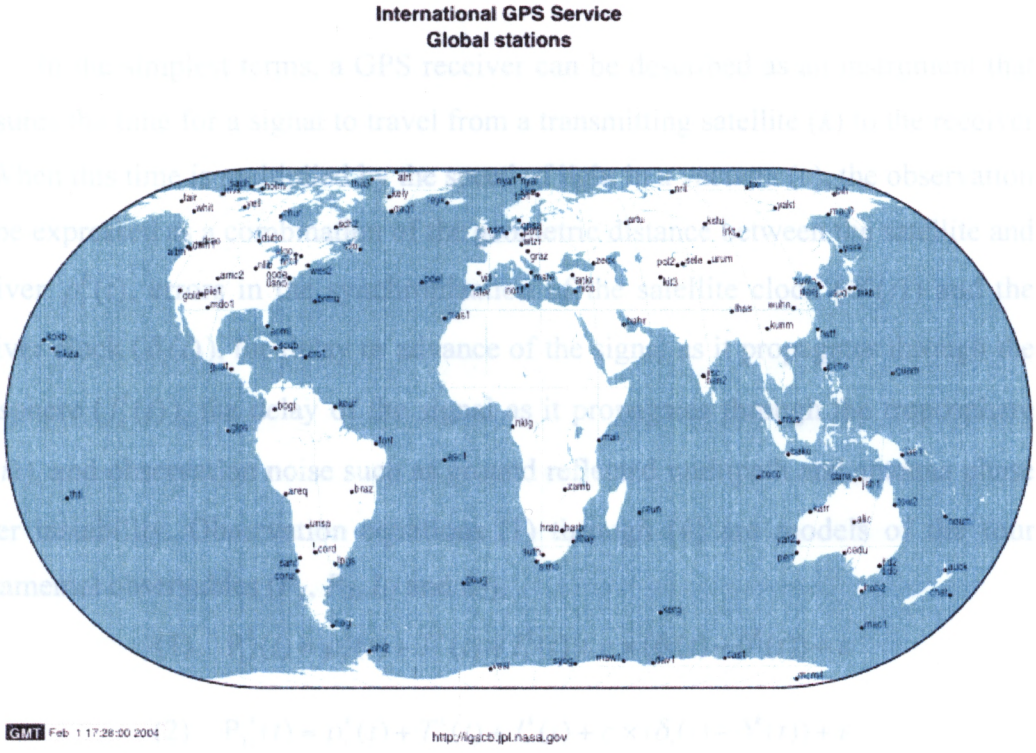

Figure 1: Map of "global" IGS stations (http://igscb.jpl.nasa.gov)

The data collected from the global stations are used by the analysis centers to compute products for general scientific use. A list of IGS products is shown in Table 3.

Table 3: IGS Derived Data Products

IGS Product Type	Accuracy (units)	Comment
Satellite Ephemeredes	2 (cm)	Final orbits available with about 2 week latency
Earth Rotation Parameters	0.05 (mas) Polar Motion 0.02 (ms) Length of Day	Polar Motion, Polar Motion Rate, and Length of Day.
Zenith Tropospheric Path Delay	4 (mm) Zenith Path Delay	ZTD at IGS global stations estimated with 2-hour time steps.
Total Electron Content	2-8 (TECU)	Global grid with 5° x 2.5° resolution
Geocentric Coordinates and Velocities	3 (mm) horizontal 6 (mm) vertical	Referenced to the ITRF

3.5 Observation Equation

In the simplest terms, a GPS receiver can be described as an instrument that measures the time for a signal to travel from a transmitting satellite (k) to the receiver (i). When this time is multiplied by the speed of light in a vacuum (c), the observation can be expressed as a combination of the geometric distance between the satellite and receiver $\rho_i^k(t)$, errors in the synchronization of the satellite clock ($\delta^k(t)$) and the receiver clock ($\delta_i(t)$), the delay or advance of the signal as it propagates through the ionosphere ($I_i^k(t)$), the delay of the signal as it propagates through the troposphere ($T_i^k(t)$), and observation noise such as ground reflected multipath and antenna phase center instability. Observation equations (1) through (4) are models of the four fundamental observables (P_1, P_2, L_1 and L_2).

$$(1)\quad \mathrm{P}_{1i}^k(t) = \rho_i^k(t) + T_i^k(t) + I_i^k(t) + c \times (\delta_i(t) - \delta^k(t)) + \varepsilon$$

$$(2)\quad \mathrm{P}_{2i}^k(t) = \rho_i^k(t) + T_i^k(t) + I_i^k(t) + c \times (\delta_i(t) - \delta^k(t)) + \varepsilon$$

$$(3)\quad L_{1i}^k(t) = \rho_i^k(t) + N_{1i}^k\lambda_1 + T_i^k(t) - I_i^k(t) + c \times (\delta_i(t) - \delta^k(t)) + \varepsilon$$

$$(4)\quad L_{2i}^k(t) = \rho_i^k(t) + N_{2i}^k\lambda_2 + T_i^k(t) - I_i^k(t) + c \times (\delta_i(t) - \delta^k(t)) + \varepsilon$$

The carrier phase equations (L_1 and L_2) include a term ($N_{f_i}^k$) called the ambiguity. This ambiguity was discussed previously in the section on GPS signals. It represents the distance between the satellite and receiver when it begins tracking the satellite. The affect of the ionosphere is opposite in sign for the pseudorange measurements (P_1 and P_2) and carrier phase measurements (L_1 and L_2). The ionosphere induces a delay of the signal in pseudorange measurements and an advance of the carrier phase. This difference in sign is related to the phase and group velocity of the microwave signal as it passes through the ionosphere.

3.6 Linear Combinations of Observations

The pseudorange and carrier phase observables (P_1, P_2, L_1 and L_2), expressed in units of distance (meters), can be linearly combined to eliminate and isolate certain

components of the observation equation. For instance, a linear combination can be formed to remove the effect of the ionosphere. Similarly, a linear combination can be formed that isolates the ionosphere. These combinations are listed below, followed by a brief description.

$$(5) \quad L_3 = \frac{1}{f_1^2 - f_2^2}(f_1^2 L_1 - f_2^2 L_2)$$

Equation (5) eliminates the phase advance of the ionosphere on the carrier phase observables. The disadvantage of this linear combination is that the noise from the L_1 and L_2 carrier phase measurements is increased by nearly a factor of three. For receivers that have dual frequency capability, the L_3 combination is usually the preferred method to use in geodetic and atmospheric applications. The only times when L_1 or L_2 observations are used individually are when networks of stations are operated over such short distances that ionospheric effects can be eliminated through differencing or other methods.

$$(6) \quad L_4 = L_1 - L_2$$

Equation (6) differences away the geometric, tropospheric, and clock synchronization components of the carrier phase equation. The effect of the ionosphere and the ambiguities remain. This linear combination is used to estimate global, regional, and high resolution ionosphere models [*Rocken et al.*, 2000].

$$(7) \quad L_5 = \frac{1}{f_1 - f_2}(f_1 L_1 - f_2 L_2)$$

Equation (7) is called the widelane linear combination. The combined wavelength of L1 and L2 carrier phase measurements is 84 cm. This long wavelength simplifies ambiguity resolution. It is commonly used in the analysis of stations that are separated by more than a few tens of km.

3.7 Differences of Observations

In addition to the linear combinations of different observables, observations from pairs of stations and satellites can be differenced. Differencing is commonly used to eliminate satellite and receiver clock errors. The three most common

differencing equations used are the single difference, the double difference and the triple difference. A single difference observation is the combination of observations from two stations and one satellite. It is used to eliminate the receiver clock errors.

$$(8) \quad L_{Fi,j}^{k} = L_{Fi}^{k} - L_{Fj}^{k}$$

A double difference is the difference of two single differences. It is the combination of observations from two stations and two satellites. In this combination, satellite clocks are eliminated.

$$(9) \quad L_{Fi,j}^{k,l} = L_{Fi,j}^{k} - L_{Fi,j}^{l}$$

A third combination is the triple difference; it is the time derivative of sequential double difference observations (equation (9)). It is primarily used to check for continuous carrier phase observations. These breaks are known as cycle slips and must be identified, repaired, and/or removed to ensure accurate modeling of the observations.

3.8 GPS Analysis Software

There are only a handful of GPS software packages available for atmospheric and geodetic scientific applications. The most commonly used packages are GAMIT [*King and Bock*, 2002], GIPSY [*Zumberge et al.*, 1997], and Bernese [*Hugentobler et al.*, 2001]. GAMIT uses the double difference measurement as the fundamental observable. GIPSY uses the un-differenced one-way phase measurement. Bernese can analyze data using both un-differenced and double differenced observations. As mentioned earlier, differencing removes satellite and receiver clock errors. In order for GIPSY and Bernese to use un-differenced observations, the software estimates the clock errors as additional random walk parameters.

Although the software packages are different in terms of the types of observations used (un-differenced or double-differenced) and in the implementation of the estimator (Kalman filter, or Least Squares Estimator), they all use a similar method in designing the inversion problem. First, the observations (y_i, i = 1, n) are collected into a single column matrix (**y**). The observations could be one-way observations, differenced observations, or linear combinations of observations. The

observation model is then linearized about some a priori state ($\mathbf{x_0}$) using a Taylor expansion.

$$(10)\quad \mathbf{y} = \mathbf{y}(\mathbf{x_0}) + \mathbf{A}\mathbf{x}$$

$$(11)\quad \mathbf{l} = \mathbf{y} - \mathbf{y}(\mathbf{x_0}) = \mathbf{A}\mathbf{x}$$

The apriori state vector is a column matrix of the parameters that will be estimated from the observations. It consists of any and possibly all components of the observation model represented in equations (1) - (4). Common parameters that are estimated include station position, satellite orbital elements, ambiguities, satellite and receiver oscillator offsets, and tropospheric delays. The matrix **A** represents the Jacobian, or matrix of partial derivatives, of the observation model with respect to the state vector.

$$(12)\quad \mathbf{A} = \begin{bmatrix} \delta y_1(x_o)/\delta x_1 & \delta y_1(x_o)/\delta x_2 & \cdots & \delta y_1(x_o)/\delta x_m \\ \delta y_2(x_o)/\delta x_1 & \ddots & & \\ \vdots & & \ddots & \\ \delta y_n(x_o)/\delta x_1 & & & \delta y_n(x_o)/\delta x_m \end{bmatrix}$$

The software used in the research presented here is Bernese. It uses the method of weighted least squares [*Strang*, 1988] to solve equation (11). With this method, the solution of the system (**x**) that minimizes the variance of the residuals is given by the following equation.

$$(13)\quad \mathbf{x} = (\mathbf{A}^T\mathbf{P}\mathbf{A})^{-1}\mathbf{A}^T\mathbf{P}\mathbf{l}$$

The matrix **P** represents the weighting matrix of the observations and can be diagonal or have off diagonal terms that represent the correlations between parameters. Since the original observations were first linearized, the estimate is only the improvement to the a priori state (**x**). The a priori and the estimate must therefore be combined.

$$(14)\quad \hat{\mathbf{x}} = \mathbf{x_0} + \mathbf{x}$$

The residuals (**r**) to the solution can also be computed.

$$(15) \quad \mathbf{r} = \mathbf{Ax} - \mathbf{l} = \mathbf{Ax} - (\mathbf{y} - \mathbf{y}(\mathbf{x}_0))$$

They represent the un-modeled component, if any, of the observation equation and measurement noise. Because of the statistical properties of Least Square Estimation algorithms, these residuals will be zero mean and have a Gaussian distribution. This is an important point, and one that will be utilized in the retrieval of SW.

3.9 Other GNSS Systems

While GPS is the largest and most complete GNSS system, there are others including the now decommissioned TRANSIT system, the Russian GLONASS system, and there are plans for a European Union system named Galileo [*Lachapelle et al.*, 2002]. The TRANSIT system consisted of six satellites, with a nearly circular orbit whose radius was approximately 1100 km. The TRANSIT system was decommissioned in 1996. The GLONASS and proposed Galileo constellations are similar to GPS in their use of L-band frequencies, and orbital parameters. In fact, combined GPS-GLONASS systems are now available and the IGS is computing GLONASS based products such as satellite orbits and time transfer information. The GLONASS system has been severely limited due to the lack of available funds within the Russian government, but the constellation is still in operation and does provide reliable data. The Russian government recently made a commitment to continue funding and support of the constellation and it appears that it will undergo an expansion in the upcoming years. The Galileo constellation is being principally funded by the European Union (with some support from China and other countries) as an alternative to GPS, whose program operation is controlled by the United States Department of Defense. It should be noted that the Galileo system is being designed to work in harmony with GPS, which provides the possibility to double the number of satellites available to users. This is a positive development for atmospheric sensing with GNSS systems in that it will allow a denser sampling of the atmosphere.

Chapter 4: Slant Water Vapor

4.1 Overview

Slant water vapor is the integral amount of water vapor along the path between two points. When used in the context of GPS, these two points are the transmitting satellite and the receiving antenna. The development and validation of GPS SW retrieval techniques is presented in this chapter. To make the chapter more complete, the retrieval of precipitable water vapor and its relationship to atmospheric delay is described first. The development and validation of SW has lead to two published manuscripts [*Braun et al.*, 2003; *Braun et al.*, 2001]. They are included as appendices and summarized here. In addition, a simulation experiment is presented to illustrate the capabilities and limitations of the techniques used to measure SW.

4.2 The Neutral Atmosphere and GPS

The technique of measuring atmospheric water vapor with GPS relates the delay and bending of a GPS signal as it propagates through the atmosphere to the integral of the water vapor density. The excess delay (ΔL) caused by the neutral atmosphere can be expressed as the integral of the refractivity ($N(s)$) along the path (S) between the transmitting GPS satellite and the receiving GPS antenna.

$$(16) \quad \Delta L = 10^{-6} \int_S N(s) ds + S - G$$

The term excess delay describes the additional delay of a signal when compared to one propagating through a vacuum (G). Refractivity is related to the index of refraction (n).

$$(17) \quad N = 10^6 (n - 1)$$

The refractivity is a function of atmospheric pressure (p, expressed in millibars), vapor pressure (e_w, in millibars) and temperature (T, in Kelvin) and is approximated by equation (18) [*Smith and Weintraub*, 1953].

$$(18)\quad N \approx 77.6(\frac{P}{T}) + 3.73\times 10^5(\frac{e_w}{T^2})$$

This relationship between refractivity and atmospheric composition is considered accurate to approximately 0.5%. See Bevis et al., [1992] and Bevis et al., [1994] for further discussion on the mathematical expression of refractivity. Substituting equation (18) into equation (16) yields the following integral.

$$(19)\quad \Delta L = 10^{-6}\int_S \left[77.6(\frac{P}{T}) + 3.73\times 10^5(\frac{e_w}{T^2})\right]ds + S - G$$

If atmospheric bending is ignored, a reasonable assumption for satellites above 5° elevation angle [*Sokolovskiy et al.*, 2001], Equation (19) can be simplified to contain only the integral of refractivity.

$$(20)\quad \Delta L = 10^{-6}\int_S \left[77.6(\frac{P}{T}) + 3.73\times 10^5(\frac{e_w}{T^2})\right]ds$$

The delay described by the first term in the integral is called the slant hydrostatic delay (SHD). The second term is known as the slant "wet" delay (SWD). The summation of the two is the slant total delay (STD=SHD+SWD). Equation (19) represents the T_i^k term in observation equations (1)-(4).

The integral in equation(19) is dependent on both the atmospheric composition and the path of the signal. As the elevation angle of a satellite decreases, the length of the path through the neutral atmosphere increases. Scaling the slant path delay to its equivalent delay if the satellite was at zenith is expressed below.

$$(21)\quad ZTD = ZHD + ZWD = \frac{SHD}{m_h(\theta)} + \frac{SWD}{m_w(\theta)}$$

Where ZTD is the zenith total delay, ZHD is the zenith hydrostatic delay, and ZWD is the zenith-wet delay. ZTD is equivalent to the vertical integral of equation (19). ZHD and ZWD are the vertical integrals of each component of equation (19). The terms $m_h(\theta)$ and $m_w(\theta)$ are called the hydrostatic mapping function and the wet mapping function. Analytic expressions of these mapping functions have been formulated by Davis et al. [1985] and Niell [1996]. They are based on the continued fraction of 1/sin(θ).

$$(22)\quad m(\theta)=\frac{\dfrac{1}{1+\dfrac{a}{1+\dfrac{b}{1+c}}}}{\sin(\theta)+\dfrac{a}{\sin(\theta)+\dfrac{b}{\sin(\theta)+c}}}$$

In the case of Niell, the coefficients in equation (22) were computed by ray tracing through the U.S. Standard Atmosphere. These coefficients vary as a function of station latitude, day of year, and altitude. Rocken et al [2001] and Niell [2001] developed a method where the mapping function is computed for a specific time and location using a numerical weather model. The advantage of this "direct mapping" or "dynamic mapping" should be in its improved representation of current atmospheric conditions.

Hydrostatic and wet mapping functions are similar but not identical. The wet mapping function is slightly larger and much more variable. The difference is related to the scale heights of water vapor (2-3 km) and the neutral atmosphere (closer to 8 km). At 10° elevation angle, the hydrostatic mapping function is between five and six. At 5° elevation it is approximately 10.

In standard GPS analysis packages, the tropospheric delay is assumed to be adequately defined with either a time varying zenith value that is the same for all satellites, or a time varying delay with an additional linear horizontal gradient [*Bar-Sever et al.*, 1998; *Davis et al.*, 1993]. The ZHD can be computed using a surface pressure measurement [*Davis et al.*, 1985; *Saastamoinen*, 1972] and can be scaled to a SHD using the $m_h(\theta)$ mapping function.

The amount of water vapor in the atmosphere is poorly correlated to surface humidity measurements. Therefore, the ZWD (and therefore SWD) cannot be accurately computed using surface measurements. ZWD is therefore included as an estimated parameter in the inverse modeling of the observation equations [*Rocken*, 1988]. The output of the estimation results in a time varying ZWD value that represents the following integral.

$$(23)\quad ZWD=(3.73x10^5)(10^{-6})\int\frac{e_w}{T^2}dz=(3.73x10^5)(10^{-6})R_v\int\frac{\rho_v}{T}dz$$

Where R_v is the gas constant for water vapor and ρ_v is the water vapor density.

4.3 Scaling ZWD to PW

Precipitable water (PW) is defined as the integrated water vapor density (IWV) divided by the density of liquid water. The path of the integral is in the zenith direction, directly above a location.

$$(24)\quad PW = \frac{1}{\rho} IWV = \frac{1}{\rho}\int \rho_v dz = \frac{1}{\rho R_v}\int \frac{e_w}{T} dz$$

The units of IWV are typically expressed as (kg/m^2). The units of PW are expressed as millimeters of liquid water. The ratio of equations (23) and (24) can be computed and simplified.

$$\Pi = \frac{PW}{ZWD} = \frac{\frac{1}{\rho R_v}\int \frac{e_w}{T} dz}{\left(3.73\times 10^5\right)\left(10^{-6}\right)\int (e_w/T^2) dz} = \frac{1}{0.373 \rho R_v} T_m$$

(25) where

$$T_m = \frac{\int \frac{e_w}{T} dz}{\int \frac{e_w}{T^2} dz} = \frac{\int \rho_v dz}{\int \frac{\rho_v}{T} dz}$$

The ratio of the two vertical integrals in (25) is called the weighted "mean temperature" T_m. Bevis et al. [1992] used approximately 9,000 radiosonde observations from the United States to derive a relationship between T_m and surface temperature (T_s).

$$(26)\quad T_m = 70.2 + 0.72 \times T_s$$

Using Equation (26) for locations within the continental United States should yield T_m values that are accurate to approximately 2%. Equation (27) provides a simple relationship to scale the estimated GPS quantity of ZWD to PW.

$$(27)\quad PW = \frac{IWV}{\rho} = \Pi \bullet ZWD$$

The ratio of PW to ZWD is typically somewhere near 0.15. This implies that a PW value of 1 mm will correspond to a ZWD of 6.5 mm.

The methods described above have been used extensively to show that GPS is an accurate, all-weather, instrument for measuring PW [*Rocken et al.*, 1995; *Rocken et al.*, 1997]. Instruments like microwave water vapor radiometers (MWR) are able to measure PW with better than 5% accuracy [*Revercombe et al.*, 2003]. Comparisons between GPS and MWRs indicate their agreement to approximately 5%. In an absolute comparison, this represents a root mean square agreement of 1.5 mm for stations in mid-latitudes where PW amounts commonly range from 10-50 mm and average around 30 mm. Comparisons of GPS PW to data collected from radiosondes also show agreement of approximately 1.5 mm or better. For a mid-latitude, continental location, PW values can range between 10 and 50 mm throughout a year.

The relatively good agreement between GPS and MWR techniques is encouraging in that the fundamental physics in the two methods are different. An MWR relies on the emission of radiation from atmospheric water vapor to derive a brightness temperature measurement, which is then related to PW. GPS relates path delay to PW. In addition to the different physical principles implemented in the retrieval methods, there is another difference between PW derived from an MWR and GPS. The two instruments sample vastly different volumes of atmosphere. The beam width of an MWR is between 5° and 10°. The small solid angle associated with this narrow beam width ensures that an MWR provides a true measure of the water vapor directly over an instrument. This is in contrast to GPS. GPS software packages frequently use all observations collected above an elevation angle of 5° or 10°. This low elevation mask creates a volume of atmosphere that is quite large and often times contain significant variations. When there is significant variability in water vapor amounts, the GPS PW estimate might not accurately represent what is directly above a station. Enhancing the GPS method to resolve the water vapor amount in each satellite direction provides the opportunity to characterize the atmosphere in a more detailed and precise manner. This leads to the concept of SW.

4.4 Slant Water Vapor Retrieval

The method of using GPS to estimate PW is described above. To summarize, a GPS receiver measures the elapsed time for a signal to propagate from a satellite to

the receiving antenna. As part of this travel time, the signal is delayed and bent by the atmosphere. A portion of this atmospheric delay, the hydrostatic portion, can be calculated and removed using a surface pressure measurement. The remaining portion of the delay, which corresponds to the wet component of the excess delay, is estimated as a parameter in the inversion of the observation equations. This inversion assumes that the wet delay to all satellites can be accurately modeled using a time varying zenith parameter that is scaled to the elevation angle of the satellite by a mapping function $m_w(\theta)$. Most GPS analysis packages try to improve on this simple, horizontally homogeneous, model with the additional estimation of horizontal atmospheric gradient terms [*Bar-Sever et al.*, 1998; *Davis et al.*, 1993]. While gradients do provide some increased spatial resolution of the water vapor fields, the atmospheric structure is often times highly variable and cannot accurately be described with this simple linear model. This has been confirmed in a recent analysis by Aonashi [2004] which indicates that when estimating horizontal gradients with a pointing MWR, the residuals from the estimate represent a larger portion of the azimuthal variability than the estimated gradient term.

At first glance, it seems that the optimal method of determining SW would be to estimate it directly during the inversion of the observation equations. This is not possible using traditional, over-determined least squares techniques. The estimation of station coordinates and ambiguities makes the independent parameterization of rapidly changing delays in the direction of individual satellites impossible. If this method were implemented, it would lead to a parameterization with an underdetermined set of linearly independent observations. This is especially true when satellite and receiver clock errors are not removed through double differences. Instead, the retrieval of SW combines the ZWD estimate and the un-modeled residuals (S_i^k) from the estimation to create the slant-wet delay. The SWD is scaled to SW through the same Π factor that is used to scale ZWD to PW. The expression of SW can be represented by equation (28).

$$(28) \quad SW_i^k = \Pi \times (m_w(\theta) \times ZWD + S_i^k)$$

The term (S_i^k) corresponds to the residual that is saved in the estimation step and is equivalent to **r** in equation (15). If the observations are accurately modeled, and the estimated parameters are not biased, the residuals contain information on how the model differs from the actual observations. By constraining the estimate of the station coordinates to precisely determined values, resolving ambiguities, and using precise IGS satellite orbit products, the parameter that is modeled most inaccurately is the ZWD parameter. The resulting residuals then contain information on how well (or poorly) the observations matched the model. If the residual of an observation is negative, the ray to that satellite path passes through atmosphere that contains less water vapor compared to the mapped ZWD estimate. If the residual is positive, it represents a ray that traveled through a volume of atmosphere that is wetter than the ZWD estimate. Combining the ZWD value with the residual produces the SW value.

The use of double difference observations eliminates the errors associated with satellite and receiver clock errors. This makes the double difference observation more accurate than one between a single satellite and receiver. However if there are N ground stations, and M satellites at any instance in time, there can only be (N-1) x (M-1) linearly independent double difference observations. The direct transformation from double-difference residuals to one-way residuals is therefore impossible. The use of constraints has been used to unwrap the double difference residuals into so called "zero difference" residuals. The term "zero difference" is used because they are derived from double difference residuals. The transformation of double-difference residuals to zero difference residuals is described in Alber et al. [2000].

The steps involved in transforming GPS observations into estimates of SW are diagramed in Figure 2. The GPS observations are collected and stored in individual files grouped by station. The observations are combined into double differences to remove satellite and receiver clock errors. These double differences are scanned (by computing the time derivative) for data outliers and blunders. Where possible, the double difference observations are repaired. Once outliers have been edited and repaired, the double difference observations are used as input in the parameter estimation routine. Initially, the observations are processed by individual baseline (all observations between two stations) to resolve carrier phase ambiguities. Ambiguities

are estimated as parameters (first using the L_5, then the L_3 linear combination) and stored with the observations so that they can be reintroduced as known values later. Ambiguities are solved in a separate step because they are essentially nuisance parameters that are not correlated between stations. In the final analysis step, the following parameters are estimated: station coordinates, unresolved phase ambiguities, and zenith wet troposphere delays. The station coordinate parameters are tightly constrained to the previous week's coordinate solution. Constraining the coordinates to these accurate a priori values improves the estimation of the ZWD parameters. Once the ZWD values are estimated, they are used as input to compute the un-modeled double difference residuals. These residuals are stored and inverted into one way residuals using the zero mean assumptions [*Alber et al.*, 2000]. The ZWD values and the zero difference residuals are then combined to create SWD values that can be scaled to SW using the Π factor.

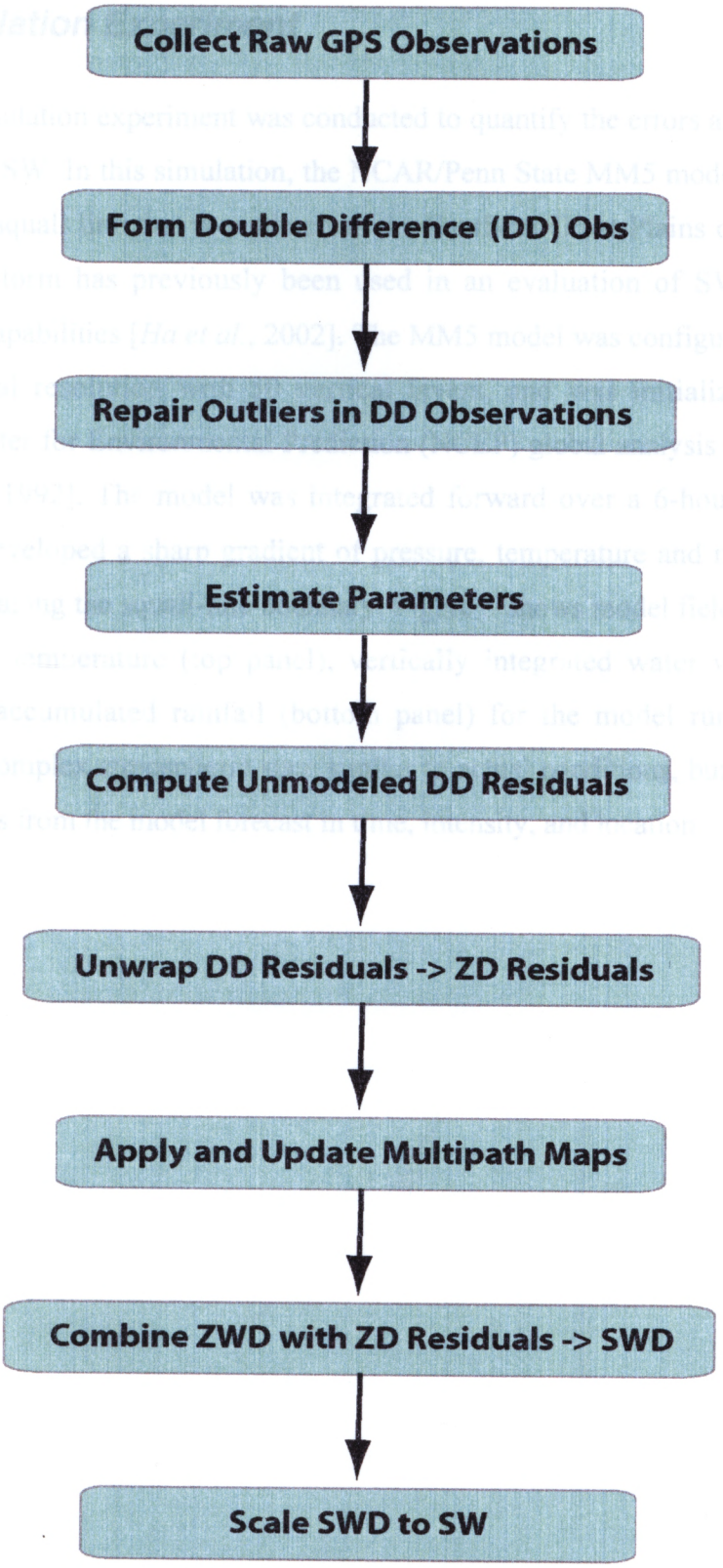

Figure 2: Diagram of processing steps in the computation of GPS SW.

4.5 Simulation Experiment

A simulation experiment was conducted to quantify the errors associated with GPS derived SW. In this simulation, the NCAR/Penn State MM5 model was used to reproduce a squall line that moved across the Southern Great Plains on October 30 1999. This storm has previously been used in an evaluation of SW to improve forecasting capabilities [*Ha et al.*, 2002]. The MM5 model was configured to run at 3 km horizontal resolution with 50 vertical layers, and was initialized using the National Center for Environmental Prediction (NCEP) global analysis field [*Parrish and Derber*, 1992]. The model was integrated forward over a 6-hour period. The squall line developed a sharp gradient of pressure, temperature and moisture, with rain forming along the squall-line boundary. Figure 3 shows model fields of sea level pressure and temperature (top panel), vertically integrated water vapor (middle panel), and accumulated rainfall (bottom panel) for the model run. The model generates a complex atmospheric state similar to actual conditions, but the observed rainfall differs from the model forecast in time, intensity, and location.

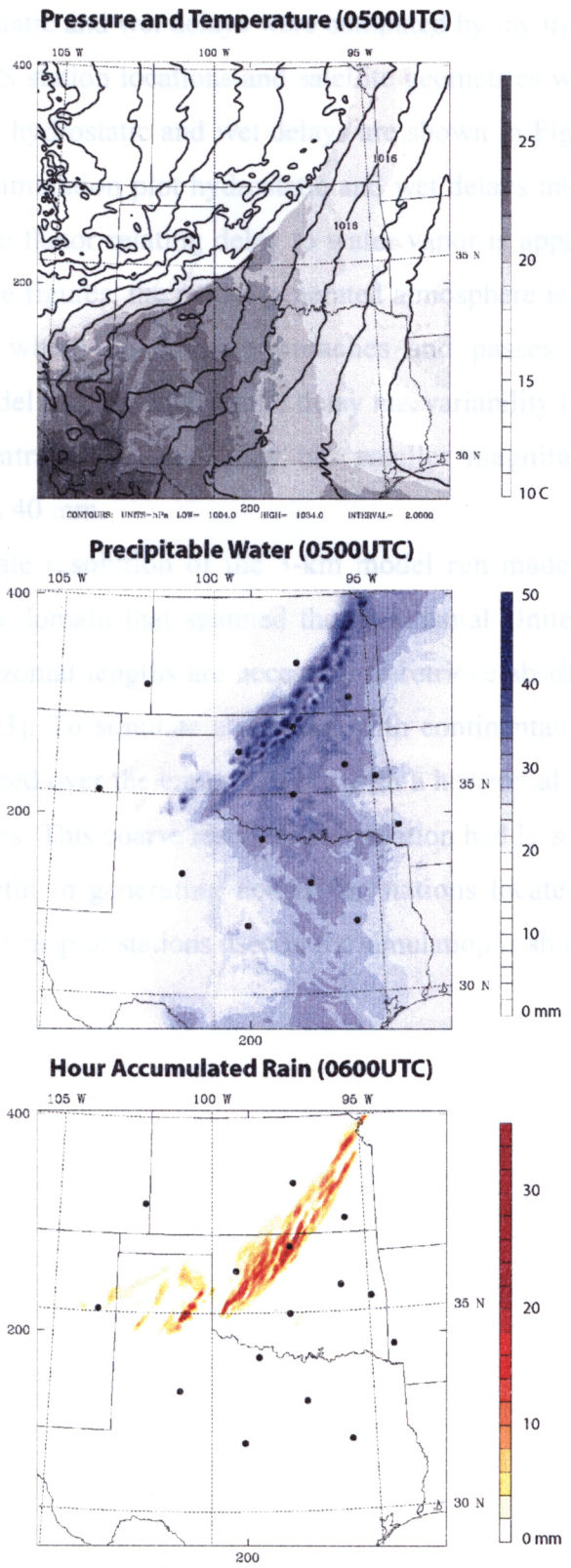

Figure 3: Model output fields used in the SW simulation – pressure and temperature (top), precipitable water (middle), hourly accumulation of rainfall (bottom).

Slant hydrostatic and wet delays were computed by ray tracing through model fields. Realistic GPS station locations and satellite geometries were used. Examples of the zenith scaled hydrostatic and wet delays are shown in Figure 4 and Figure 5. All figures in this simulation plot hydrostatic and wet delays instead of SW or PW. Recall that the scale factor relating delay to water vapor is approximately 0.15. As can be seen from the figures, the model-generated atmosphere is quite variable. This is especially true when the storm approaches and passes over each station. Throughout the model run, the hydrostatic delay has variability of less than 5 mm at any instant. In contrast, the wet delay has smaller magnitude, but displays a variability of almost 40 mm.

The fine scale resolution of the 3-km model run made it computationally difficult to create a domain that spanned the continental United States. Networks spanning large horizontal lengths are necessary to retrieve absolute ZWD estimates [*Rocken et al.*, 1993]. To simulate a network with continental coverage, a second model run was created over the entire US, but with a horizontal resolution of 25 km and 23 vertical layers. This coarse resolution simulation had less variability in model fields, but was useful in generating delays for stations located outside the 3 km resolution domain. A map of stations used in the simulation is shown in Figure 6.

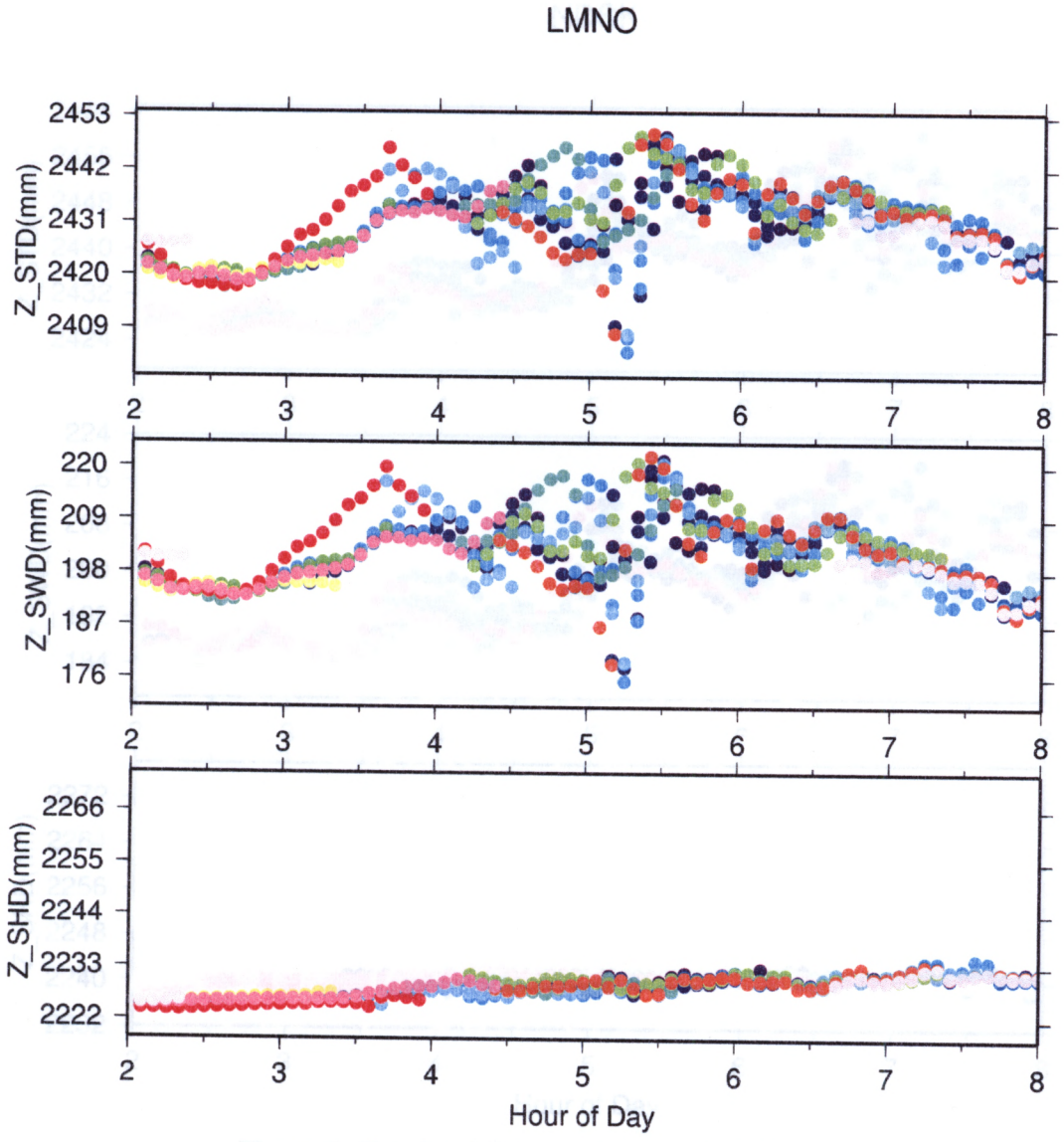

Figure 4: Simulated, zenith scaled, hydrostatic delay (lower), wet delay (middle), and total delay (upper). Each color represents a different satellite.

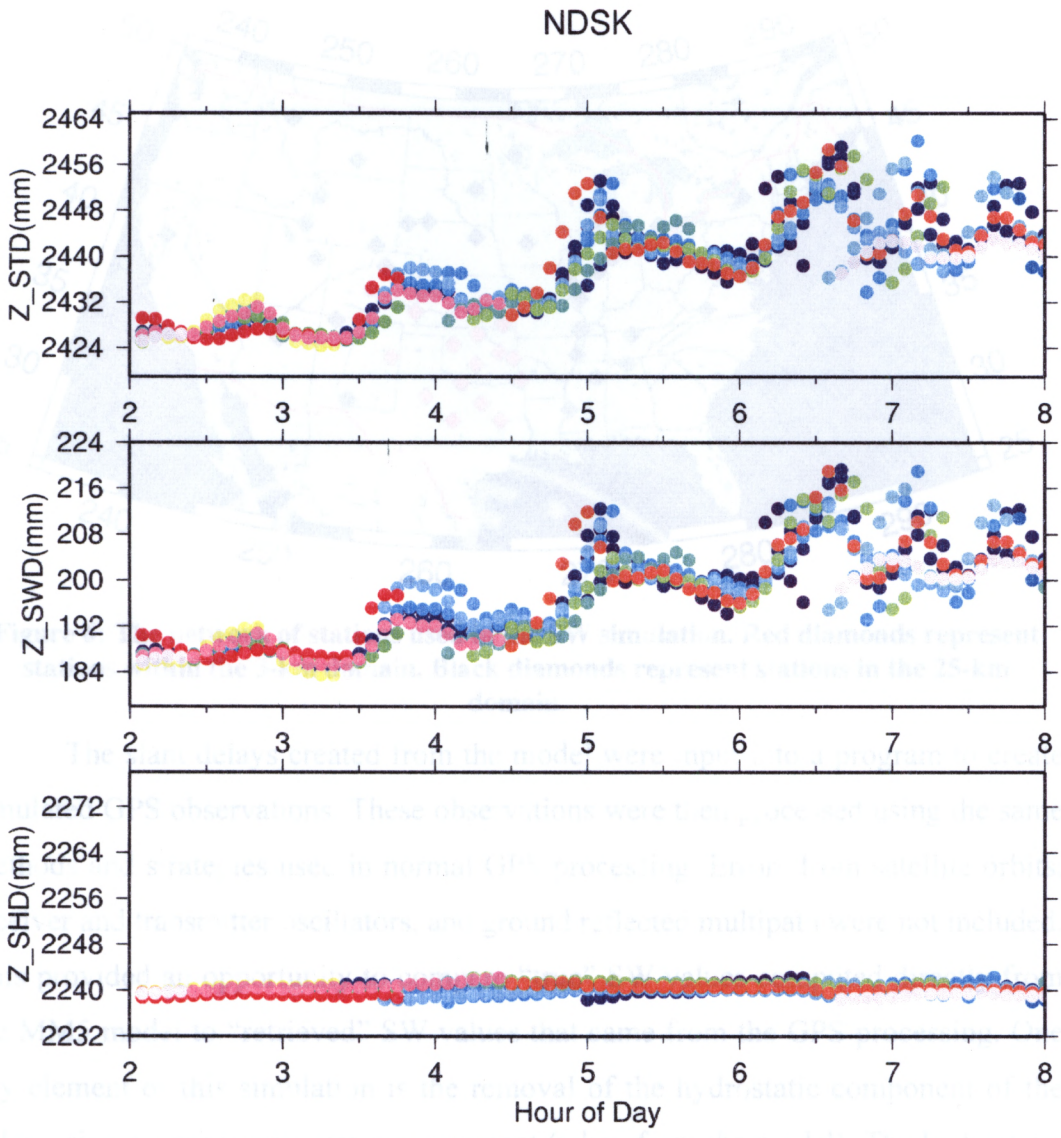

Figure 5: Simulated delays for station NDSK.

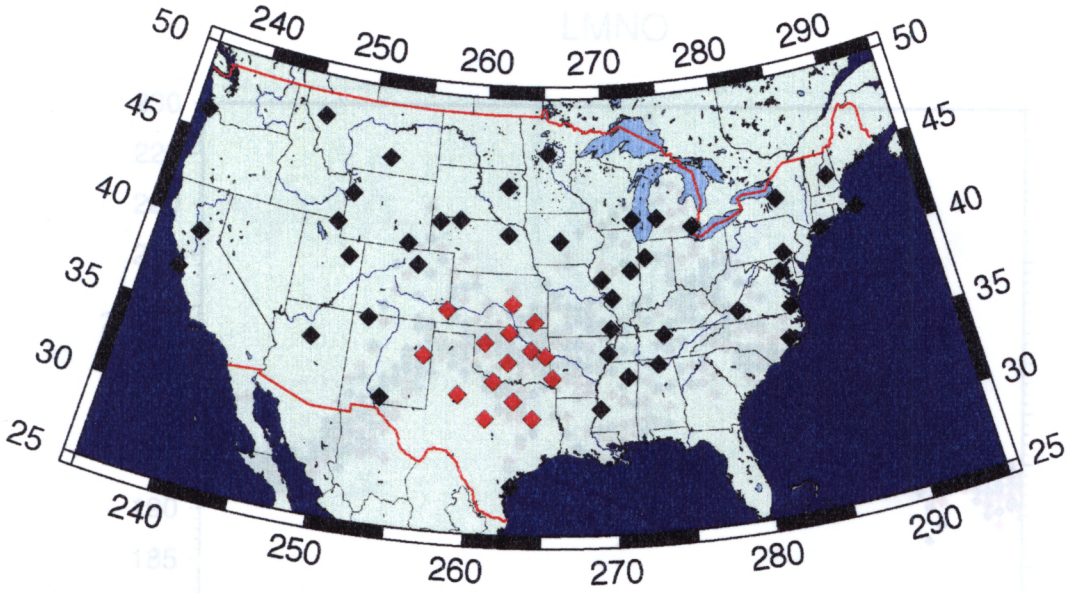

Figure 6: The network of stations used in the SW simulation. Red diamonds represent stations within the 3-km domain. Black diamonds represent stations in the 25-km domain.

The slant delays created from the model were input into a program to create simulated GPS observations. These observations were then processed using the same methods and strategies used in normal GPS processing. Errors from satellite orbits, receiver and transmitter oscillators, and ground reflected multipath were not included. This provided an opportunity to compare "true" SW values computed directly from the MM5 model to "retrieved" SW values that came from the GPS processing. One key element of this simulation is the removal of the hydrostatic component of the delay using a surface pressure measurement (taken from the model). The hydrostatic delay is assumed horizontally homogeneous. Variations in the pressure and temperature fields make this assumption incorrect. The result is that the variability in the hydrostatic delay will be interpreted as variability in the wet delay. Fortunately, as can be seen in Figure 4 and Figure 5, hydrostatic variations are much smaller than the variations in the water vapor field. This is especially true when the squall line is near a station and the water vapor field becomes complex and variable.

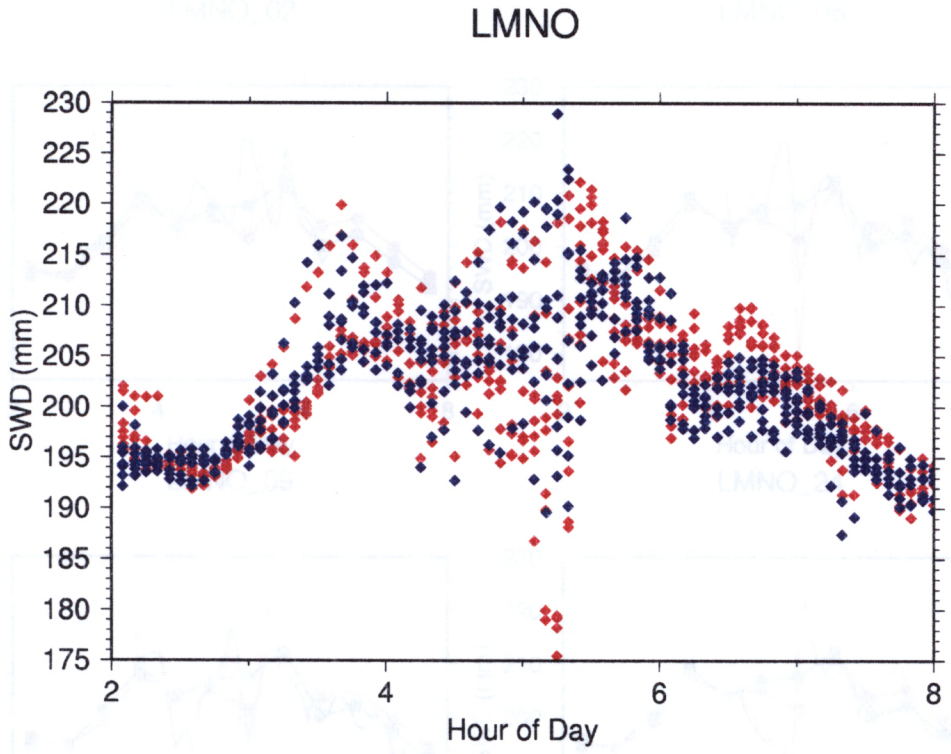

Figure 7: Comparison of Simulated SWD (red) and retrieved SWD (blue) for station LMNO.

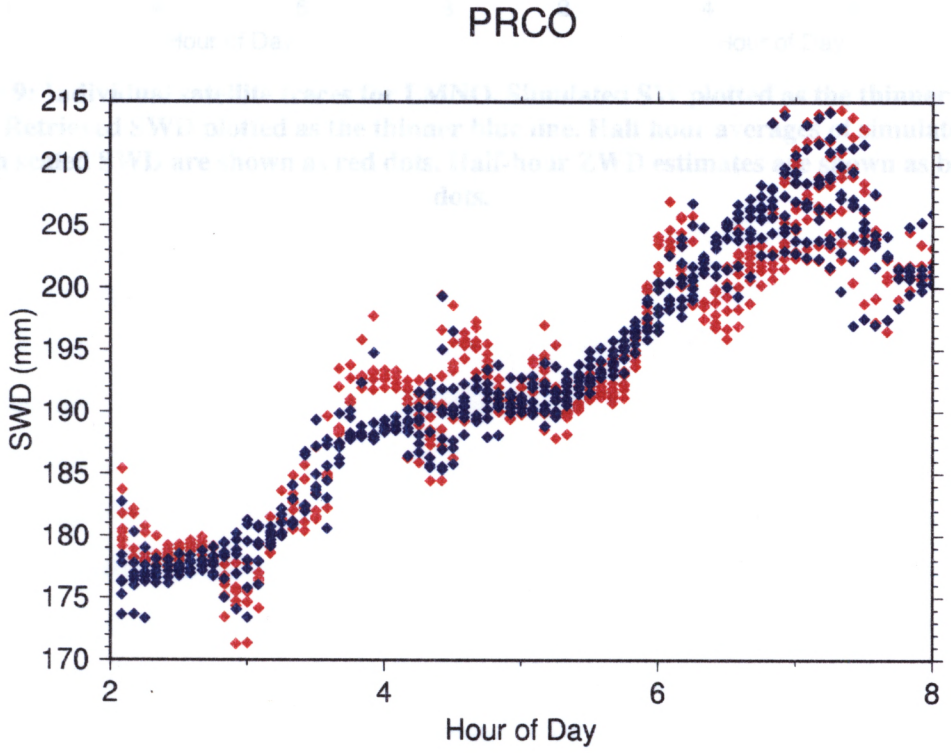

Figure 8: Simulated SWD (red) and retrieved SWD (blue) for station PRCO

error in the ZWD estimate. This error is caused by both the mis-modeling of the atmosphere using a single isotropic zenith term and the associated non-Gaussian errors of the actual atmosphere in relation to the zenith model. This systematic error has been previously identified [*Elosegui and Davis*, 2003]. The least squares estimator is based on the assumption that the modeling of the parameters results in differences between the model and the observations that have a Gaussian distribution. When the model/observations do not obey this assumption, the result is an estimate that is different from the average. This difference between the average and the estimated value is an error that is systematic in nature – it is common to all SWD values at any instant. Field comparisons of GPS PW to other instruments (MWRs) indicate that the RMS error of this type might be as large as 1.5 mm (about 10 mm in ZWD). This implies that SW values probably have a lower bound on absolute accuracy near 1.5 mm in integrated water vapor. However, the precision of SW could be much better than 1.5 mm. This is because the dominant error is common to all SW values for any station and time, and that the relative variations contained within the S_i^k term represent actual variations in the atmospheric field. Inspection of the satellite traces in Figure 9 and Figure 10 illustrate the point. The variations in the "true" SWD (thin red lines) and the retrieved SWD (thin blue lines) are similar, but offset by a component that corresponds to the difference in the ZWD estimate from the half hour average. Figure 11 plots the simulated, zenith scaled, SWD against the retrieved ZWD in black. The retrieved SWD, with the systematic error in ZWD removed, is plotted in red. The dominant error in the SWD is due to the error in the ZWD estimate.

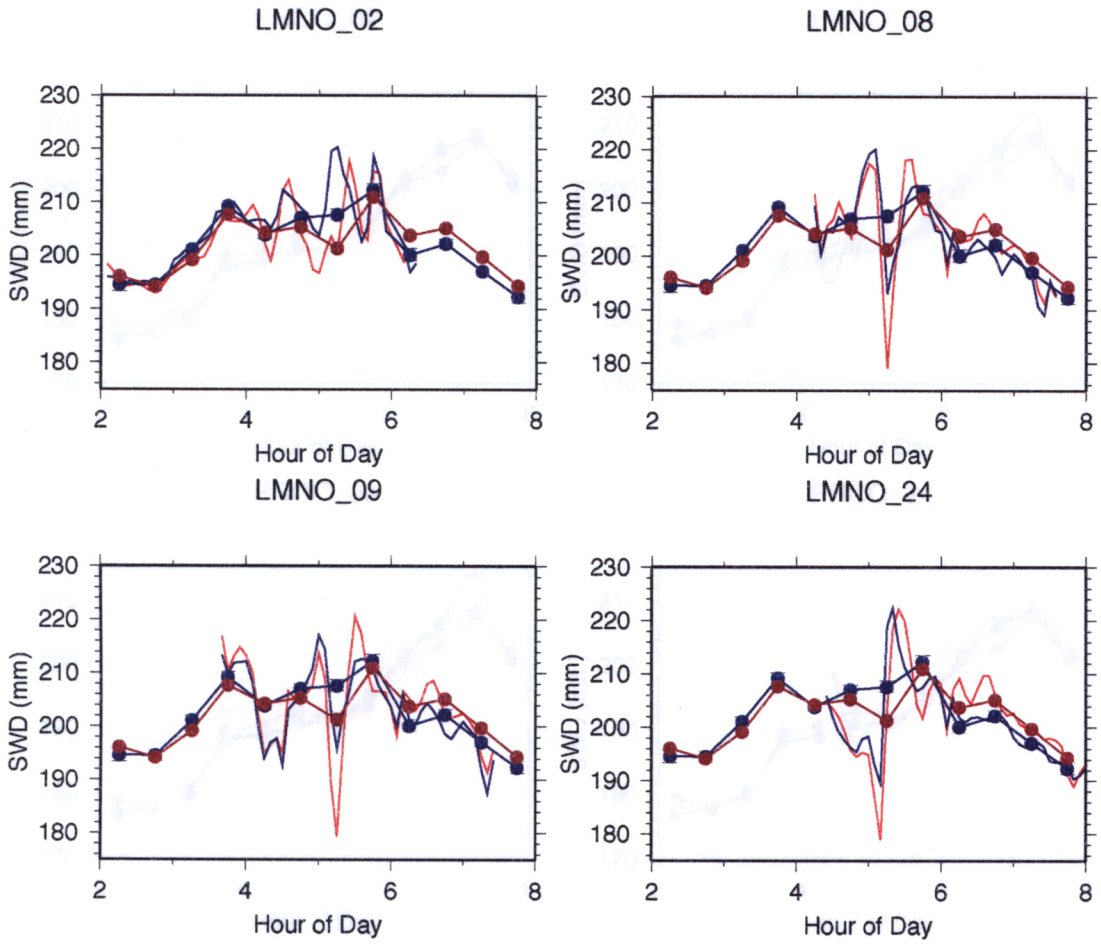

Figure 9: Individual satellite traces for LMNO. Simulated SW plotted as the thinner red line. Retrieved SWD plotted as the thinner blue line. Half hour averages of simulated zenith scaled SWD are shown as red dots. Half-hour ZWD estimates are shown as blue dots.

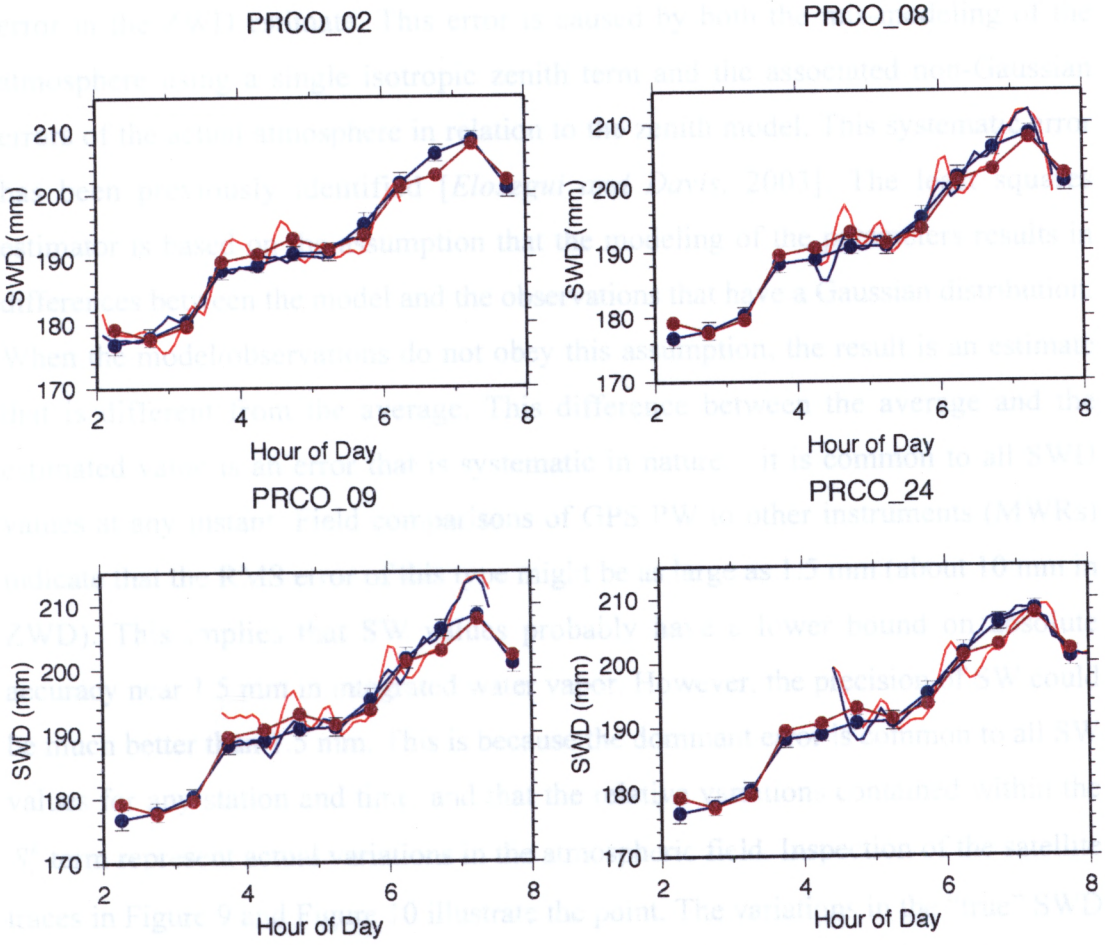

Figure 10: Individual satellite traces for station PRCO. The labeling is the same as Figure 9.

Figure 7 and Figure 8 show the simulated SWD (red diamonds) and the retrieved SWD (blue diamonds) for two stations (LMNO and PRCO). The SWD are scaled to the equivalent zenith amount using the Niell wet mapping function $m_w(\theta)$. From these two figures, it is clear that the retrieved SWD is similar to the model generated SWD. It is also clear that differences exist. The differences are apparent when the SWD values are separated by satellite. Figure 9 and Figure 10 plot four different satellites for stations LMNO and PRCO. The simulated SWD (thinner red lines) are plotted with the retrieved SWD (thinner blue lines). The ZWD estimates are shown as blue dots and are the time varying parameter estimated in the GPS analysis software. ZWD should represent the half hour average of the zenith scaled SWD. The half hour averages of the model generated SWD are plotted as red dots. The difference between each half hour average and the corresponding ZWD estimate is an

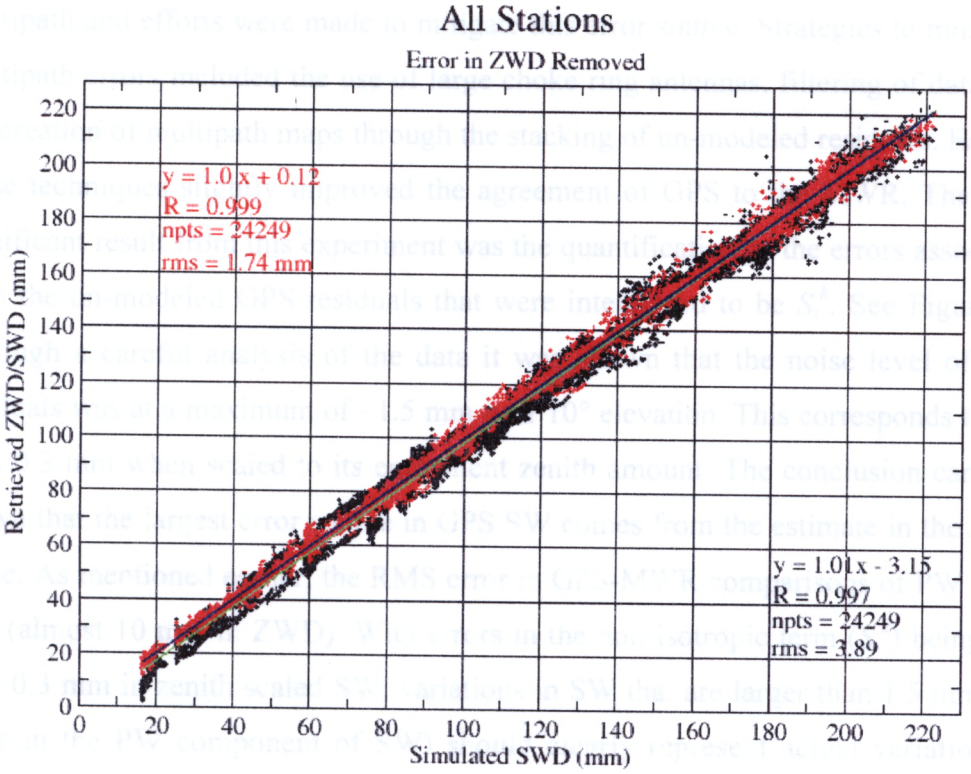

Figure 11: Linear correlation of simulated SWD against retrieved ZWD (black) and retrieved SWD (red). The error in the ZWD estimate has been removed in the retrieved SWD.

4.6 Slant Water Vapor Experiment - Platteville, CO

The first experimental testing of SW was conducted in the high plains of the Colorado Front Range [*Braun et al.*, 2001]. Two GPS stations were positioned north of Boulder and near Platteville, and were deployed adjacent to pointing MWRs from Radiometrics Corporation. The radiometers were configured so that they would measure SW in the direction of all visible GPS satellites. The non-isotropic component of SW (S_i^k in equation (28)) was calculated for the MWR and compared to the non-isotropic SW measured with GPS. In this three-day test, the S_i^k component rarely exceeded +/- 5 mm and generally was below the noise level of both the GPS and the MWR. This small signal can be attributed to the dry conditions of this high plains environment. In an attempt to extract the most information from this test, various strategies were adopted to improve the signal-to-noise of the GPS

measurements. The dominant error in the GPS S_i^k was caused by ground reflected multipath and efforts were made to mitigate this error source. Strategies to minimize multipath errors included the use of large choke ring antennas, filtering of data, and the creation of multipath maps through the stacking of un-modeled residuals. Each of these techniques slightly improved the agreement of GPS to the MWR. The most significant result from this experiment was the quantification of the errors associated with the un-modeled GPS residuals that were interpreted to be S_i^k. See Figure 12. Through a careful analysis of the data it was shown that the noise level of GPS residuals was at a maximum of ~1.5 mm near 10° elevation. This corresponds to less than 0.3 mm when scaled to its equivalent zenith amount. The conclusion can then drawn that the largest error source in GPS SW comes from the estimate in the ZWD value. As mentioned earlier, the RMS error in GPS-MWR comparisons of PW is 1.5 mm (almost 10 mm in ZWD). With errors in the non-isotropic term (S_i^k) being less than 0.3 mm in zenith scaled SW, variations in SW that are larger than 1.5 mm (the error in the PW component of SW) should clearly represent actual variations in atmospheric water vapor. In addition, since the dominant error source is going to be related to the PW component, relative differences in SW at any station and time should be significant to less than 1 mm in zenith scaled SW.

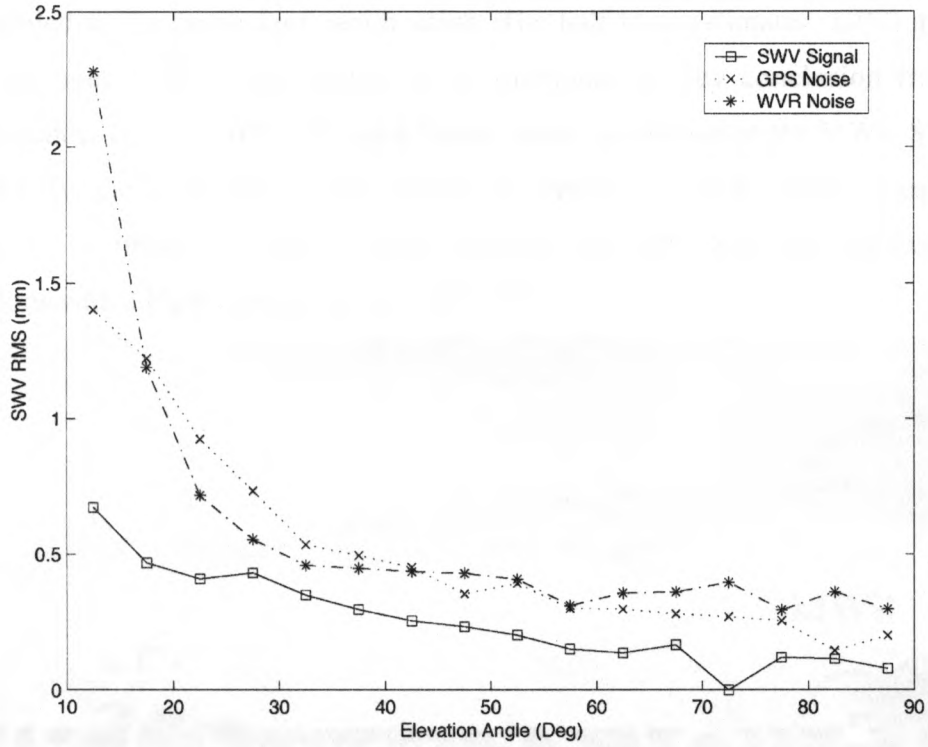

Figure 12: SW signal, GPS measurement noise, and MWR measurement noise plotted as a function of satellite elevation angle. Figure originally from Braun et al. 2001.

4.7 Slant Water Vapor Experiment - Lamont, OK

The high plains location of the initial SW validation experiment resulted in a relatively small data set, and very little water vapor variability. In this second paper [*Braun et al.*, 2003], the location of the experiment was the Atmospheric Radiation Measurements (ARM) Southern Great Plains Central Facility, near Lamont, OK. A GPS station was deployed next to a pointing MWR (Figure 13) during May and June of 2000. During this time, 47 days of data were collected and analyzed, producing a rich data set with large variations in absolute water vapor amounts, and significant variability at any instant. In this paper, both the non-isotropic component of SW (S_i^k) and the zenith scaled SW from both the MWR and GPS were compared. The data set in this analysis contained more than 100,000 measurements, which varied in zenith scaled SW from less than 10 mm to more than 60 mm. Examples of SW from four different satellite tracks are shown in Figure 14. The non-isotropic component of SW

is plotted in the top panels (GPS red and MWR blue). The bottom panels plot the total SW, scaled to the equivalent zenith value. The half hour estimates (GPS) and half hour averages (MWR) are plotted as the diamonds. A key conclusion from this experiment is that the GPS SW had a higher linear correlation to the MWR SW than the GPS PW did to the MWR. This implies two things. First, SW contains measurable variations in integrated water vapor. Second, that GPS SW can retrieve these variations with a higher precision than GPS PW.

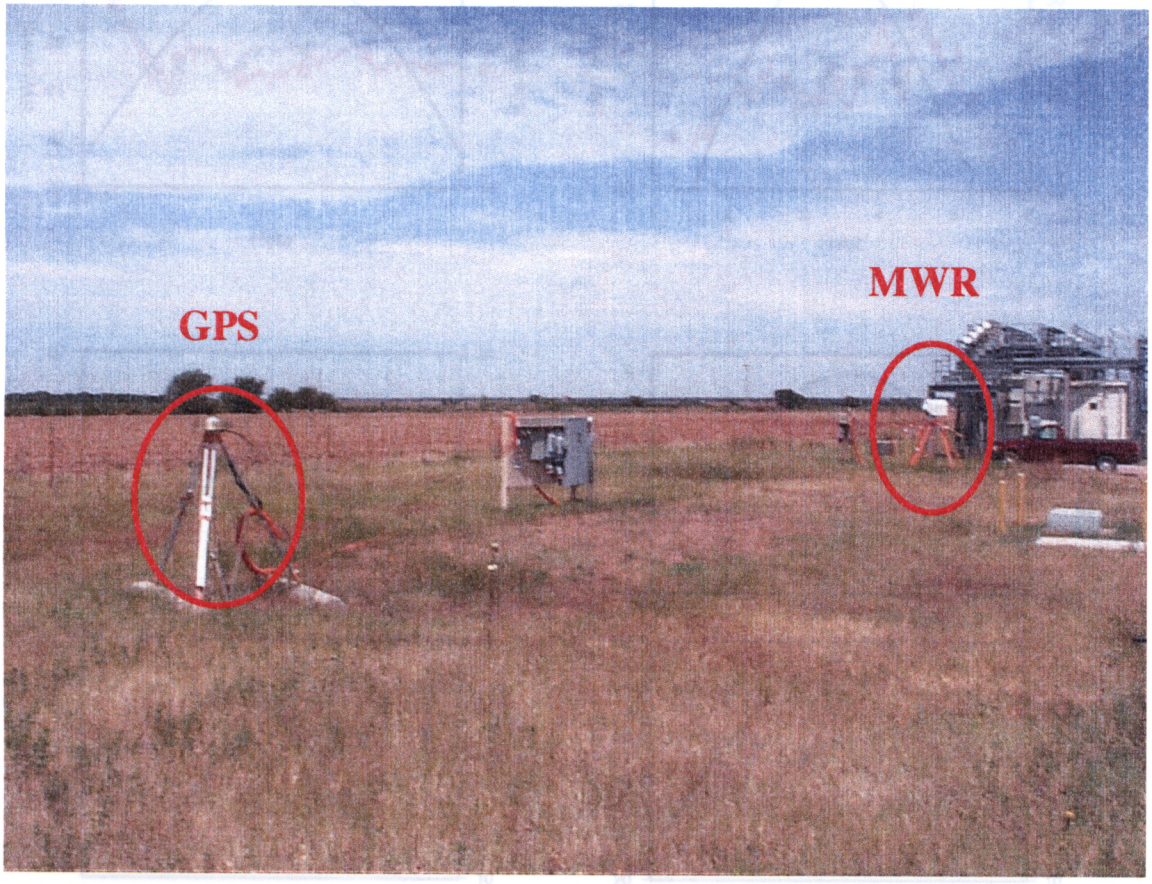

Figure 13: GPS antenna (left) and MWR (right) collocated at ARM Central Facility

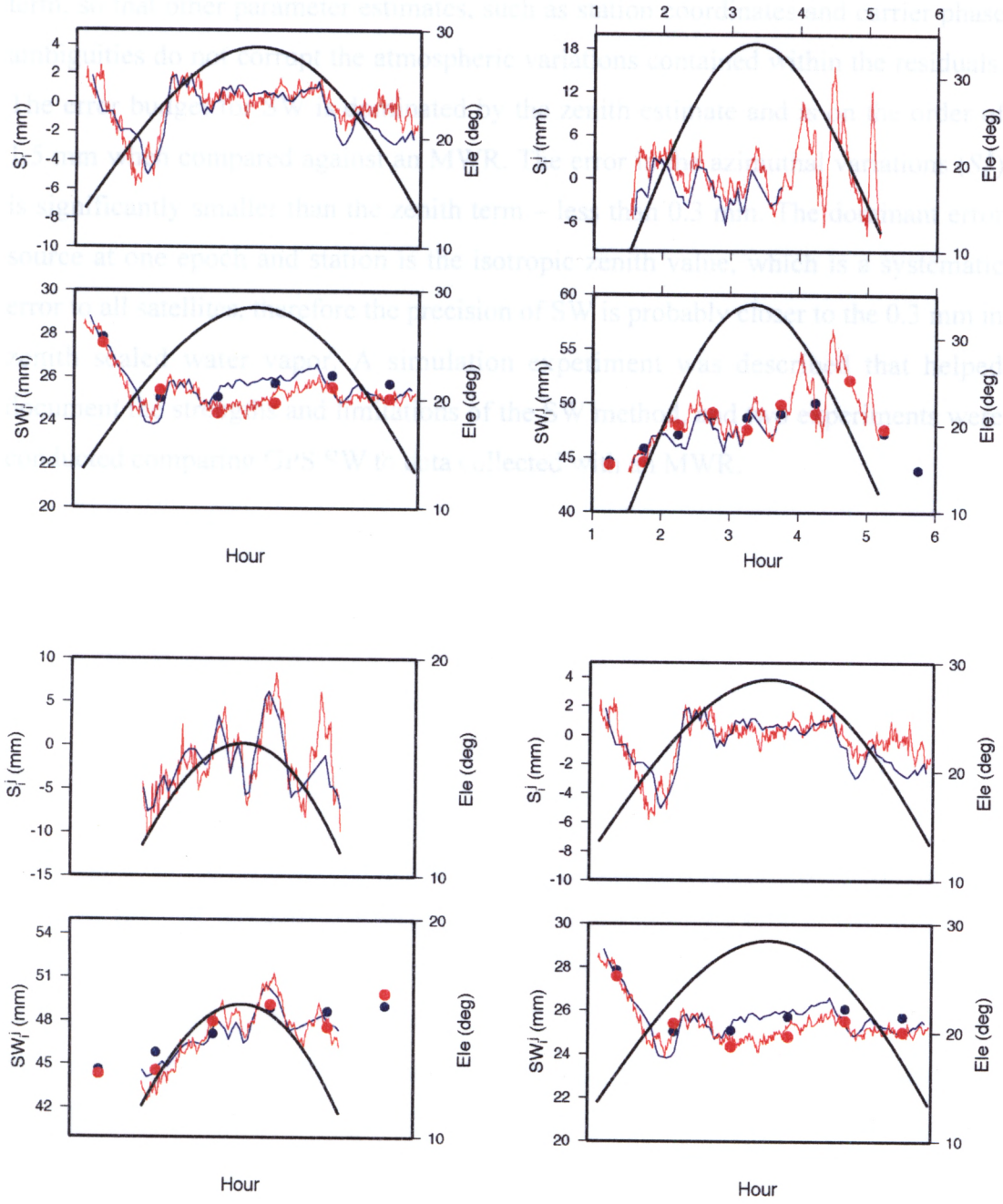

Figure 14: Examples of retrieved SW from Braun 2003 et al.

4.8 Chapter Summary

This chapter describes the methods and strategy used when inferring SW from GPS observations. This strategy can be summarized as the combination of the isotropic ZWD estimate (or PW when scaled by the PI factor) with the un-modeled residuals from the estimation program. Care must be taken when estimating the ZWD

term, so that other parameter estimates, such as station coordinates and carrier phase ambiguities do not corrupt the atmospheric variations contained within the residuals. The error budget for SW is dominated by the zenith estimate and is on the order of 1.5 mm when compared against an MWR. The error in the azimuthal variations (S_i^k) is significantly smaller than the zenith term – less than 0.3 mm. The dominant error source at one epoch and station is the isotropic zenith value, which is a systematic error to all satellites, therefore the precision of SW is probably closer to the 0.3 mm in zenith scaled water vapor. A simulation experiment was described that helped document the strengths and limitations of the SW method, and two experiments were conducted comparing GPS SW to data collected with an MWR.

Chapter 5: Single Frequency GPS Stations

5.1 Overview

The deployment of densely spaced, permanent, and high quality GPS stations requires substantial financial and infrastructure resources. To detect kilometer scale horizontal and sub-kilometer scale vertical moisture fields, new methods of collecting data needed to be developed. A single frequency GPS station was constructed for this purpose. These systems have proven to be accurate and reliable. The components of the system are described in this chapter, highlighting some interesting features. A problem with the synchronization of the observations is identified, as well as a remedy. The processing strategy used when analyzing this data is presented and results indicate that these instruments are of nearly equal quality as more expensive dual frequency stations.

5.2 System Components

A GPS station has been assembled using a low cost single frequency receiver made by original equipment manufacturer Canadian Marconi (which has now been acquired by Novatel). This OEM board level receiver was matched with a patch GPS antenna with rolled edge ground plane and a Freewave radio transceiver. A list of all the components in the station is shown in the Table 4. Two unique characteristics of the GPS stations are their single frequency receiver and the continuous streaming of data back to a central collection computer. Two of these stations are shown in Figure 15. As a testament to the reliability of the stations, the one on the right continued to operate after being vandalized with a shotgun blast.

Table 4: Significant Components of Single Frequency GPS Stations

System Component	Manufacturer
GPS Receiver	Canadian Marconi ALLSTAR OEM Receiver
GPS Antenna	Micro Pulse L1 Patch Antenna (model 1272W)
Radio modem	Freewave

Radio modem antenna (10 dB – Yagi)	Freewave

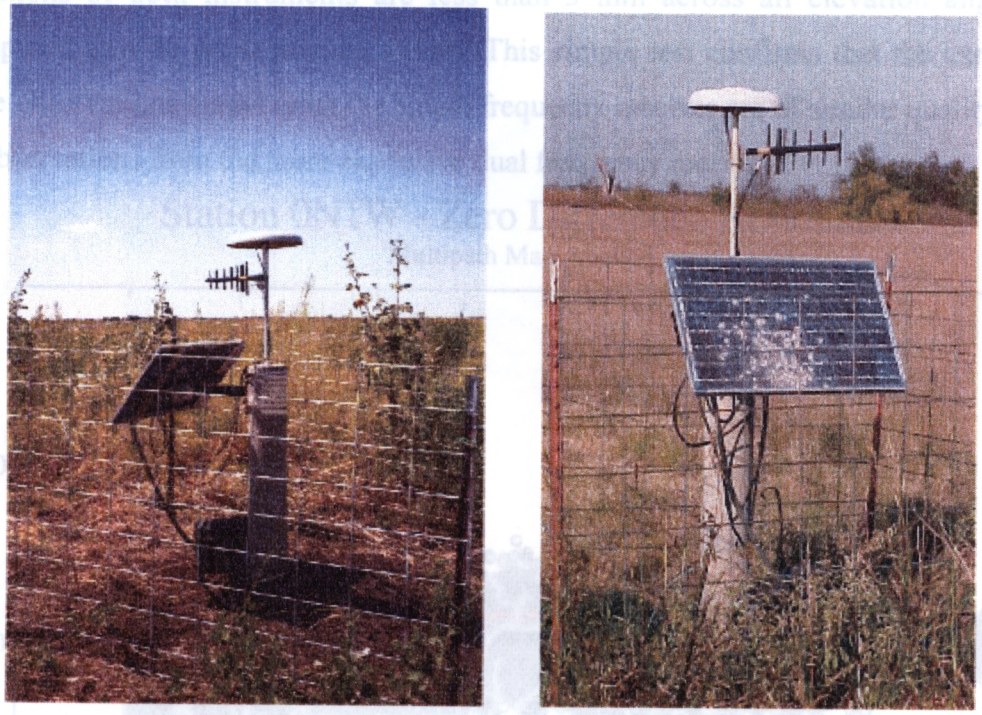

Figure 15: Single frequency GPS stations operating in north-central Oklahoma. The station on the right continued operation after being vandalized with a shotgun.

5.2.1 GPS Receiver

The CMC ALLSTAR receiver was principally designed for navigation, timing, and differential GPS positioning applications. With a single unit price of approximately $225, it is also one of the cheapest GPS receivers capable of outputting carrier phase observations. This combination makes it an attractive choice for deployment in dense arrays for atmospheric monitoring. While price is a significant factor in the selection of a GPS receiver, the most important characteristic is that it produce carrier phase observations with noise levels that are comparable to the high quality dual frequency receivers typically used for geodetic and atmospheric sensing. Figure 16 and Figure 17 show zero difference residuals for two stations spaced approximately 1 mile apart. The CMC ALLSTAR receiver was used to collect the data in Figure 16. A dual frequency, geodetic quality, Trimble 4700 was used to

collect the data in Figure 17. These data were collected on the same day (11-Feb-2004) and span the entire day of observations. The residuals in these two figures indicate that the two receivers have similar noise characteristics. The standard deviations of both instruments are less than 5 mm across all elevation angles (computed as a 50 point running value). This simple test confirms that the carrier phase observations output from the single frequency receiver are of similar quality to the observations from the more expensive dual frequency receiver.

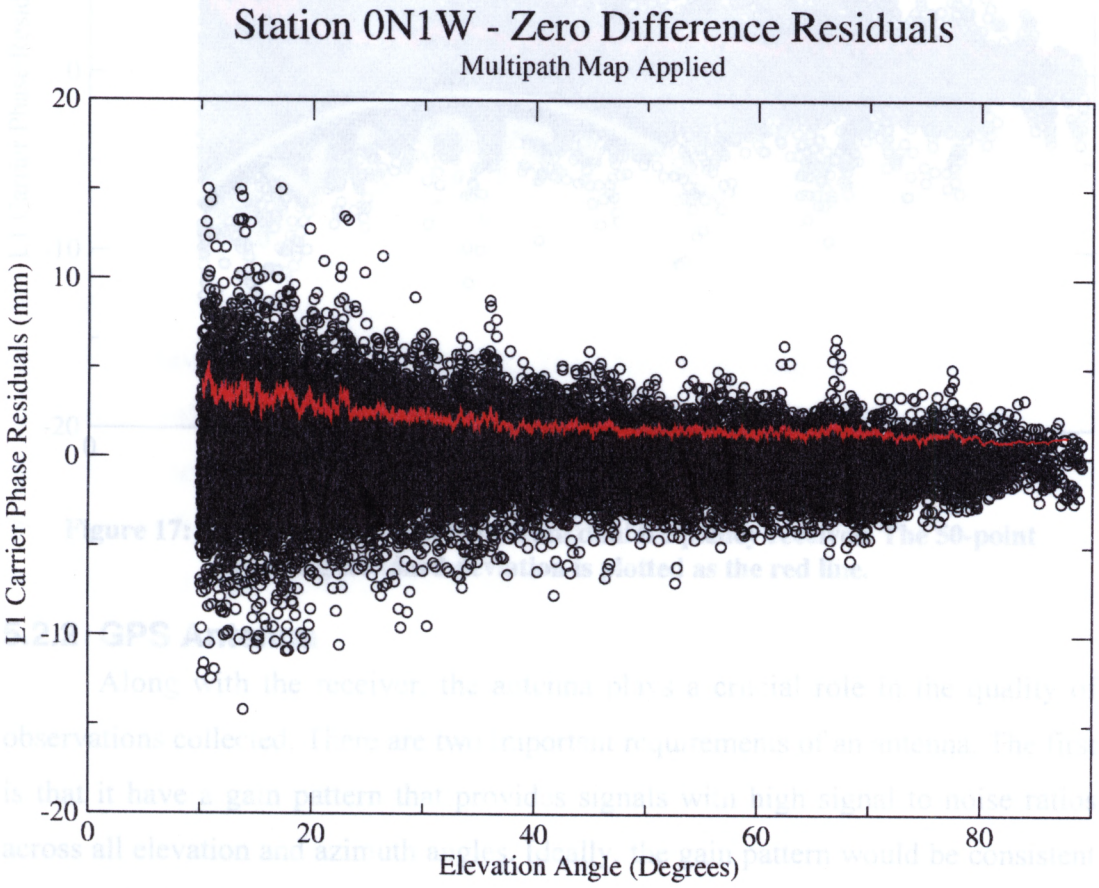

Figure 16: Zero difference residuals from single frequency receiver. The 50-point running standard deviation is plotted as the red line.

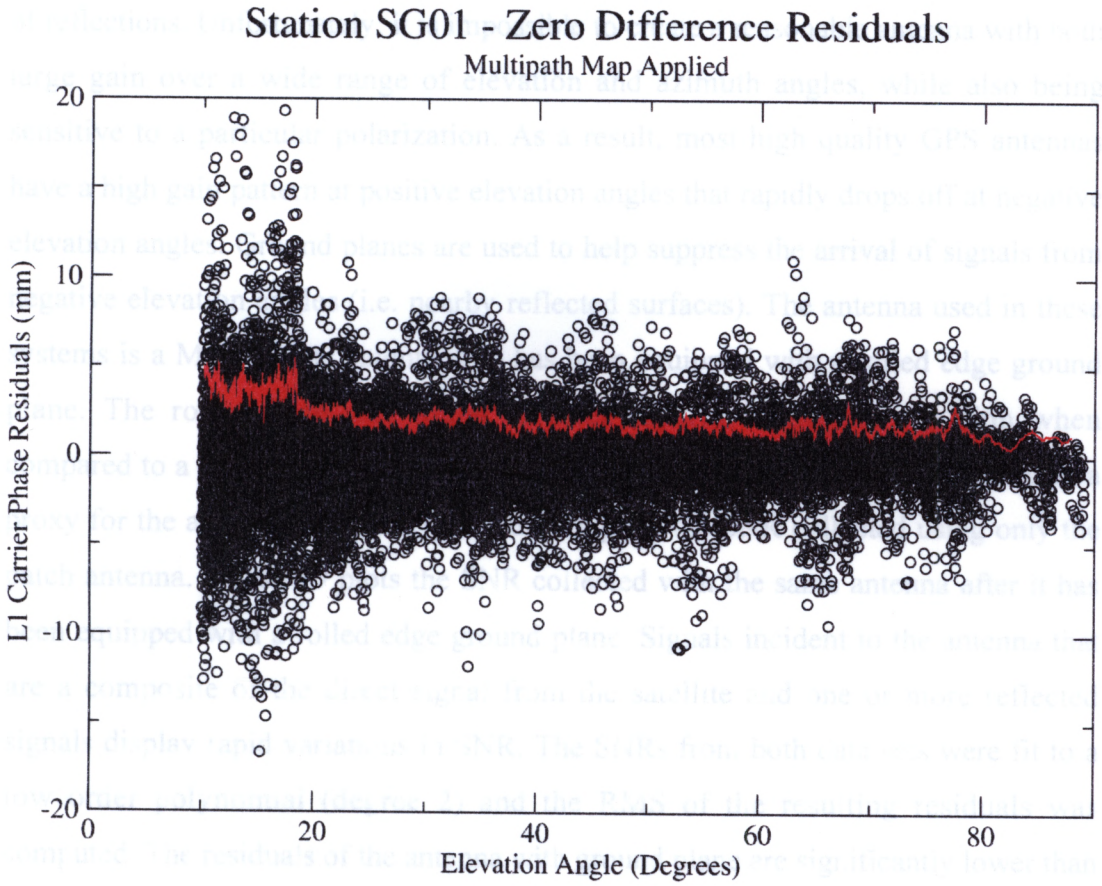

Figure 17: Zero difference residuals from dual frequency receiver. The 50-point running standard deviation is plotted as the red line.

5.2.2 GPS Antenna

Along with the receiver, the antenna plays a crucial role in the quality of observations collected. There are two important requirements of an antenna. The first is that it have a gain pattern that provides signals with high signal to noise ratios across all elevation and azimuth angles. Ideally, the gain pattern would be consistent across all elevation angles greater than zero. The second requirement is that it provides some level of multipath suppression. One possible method of multipath suppression is to design an antenna that is sensitive to only right hand circularly polarized (RCHP) signals. GPS signals are transmitted with RHCP. If the transmitted signal reflects off a surface before arriving at the antenna, the polarization reverses and becomes left hand circularly polarized (LHCP). An antenna that would be sensitive to only RHCP would suppress the largest component of antenna multipath, even though it would still be sensitive to multipath originating from an even number

of reflections. Unfortunately, it is impossible to create a reasonable antenna with both large gain over a wide range of elevation and azimuth angles, while also being sensitive to a particular polarization. As a result, most high quality GPS antennas have a high gain pattern at positive elevation angles that rapidly drops off at negative elevation angles. Ground planes are used to help suppress the arrival of signals from negative elevation angles (i.e. nearby reflected surfaces). The antenna used in these systems is a Micro Pulse antenna that has been equipped with a rolled edge ground plane. The rolled edge was found to offer superior multipath rejection when compared to a flat surface. Observation signal to noise ratios (SNR) can be used as a proxy for the antenna gain pattern. Figure 18 plots the SNR collected using only the patch antenna. Figure 19 plots the SNR collected with the same antenna after it has been equipped with a rolled edge ground plane. Signals incident to the antenna that are a composite of the direct signal from the satellite and one or more reflected signals display rapid variations in SNR. The SNRs from both data sets were fit to a low order polynomial (degree 2) and the RMS of the resulting residuals was computed. The residuals of the antenna with ground plane are significantly lower than the residuals from just the antenna itself (1.23 mm RMS compared to 1.65 mm RMS). This is a good indication that the ground plane plays a significant roll in improving the overall characteristics of the antenna.

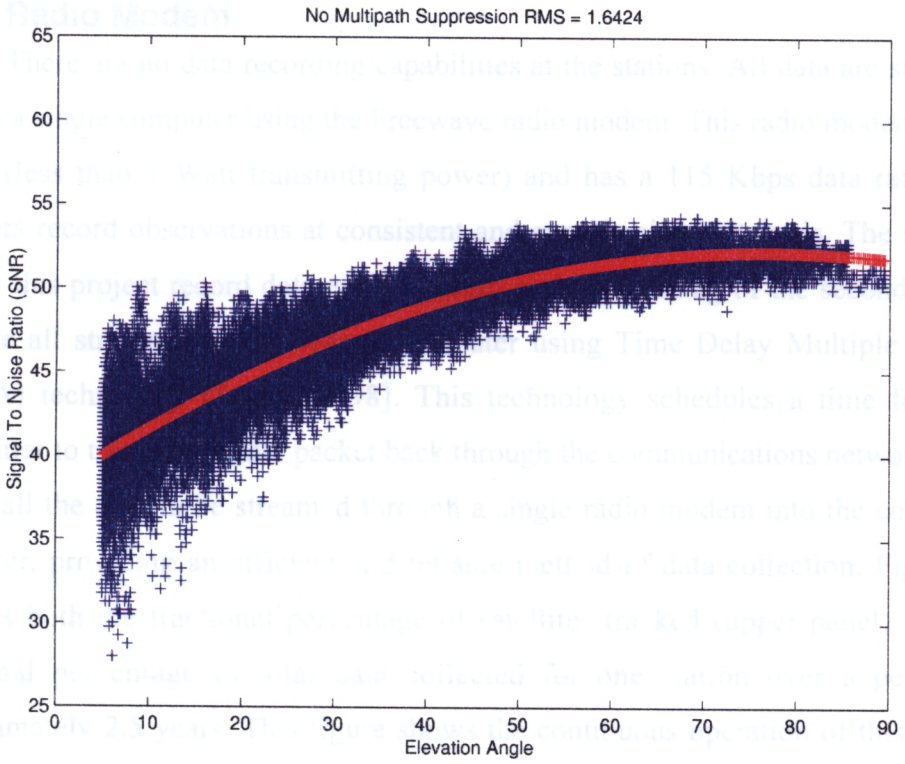

Figure 18: Signal-to-Noise (SNR) values in dBm for Micropulse patch antenna without multipath suppression.

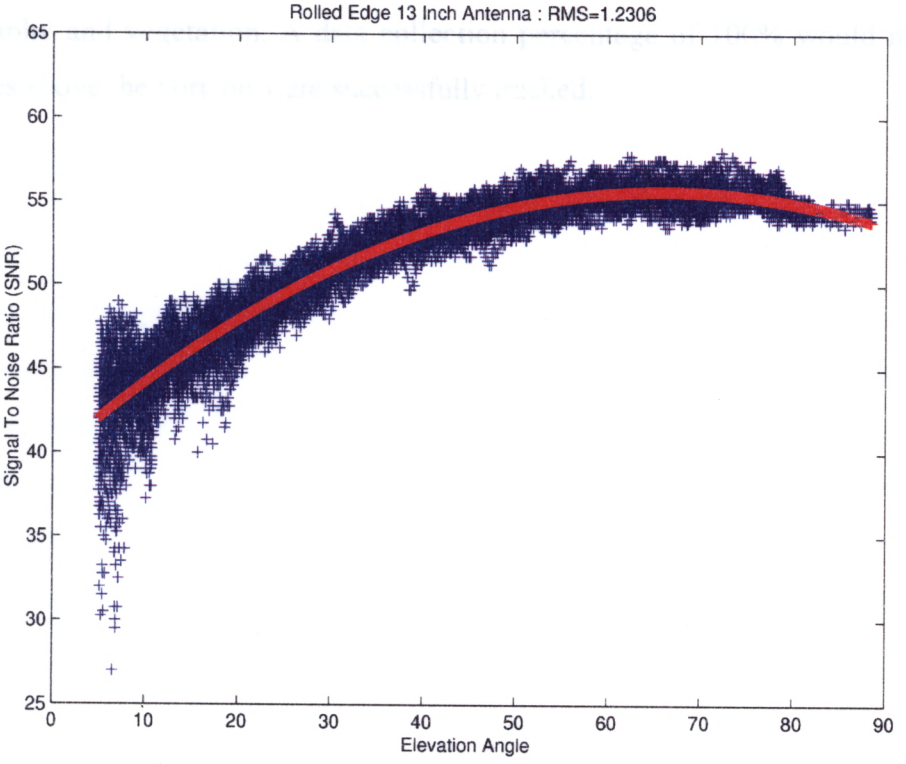

Figure 19: SNR values in dBm of Micropulse antenna with rolled edge ground plane.

5.2.3 Radio Modem

There are no data recording capabilities at the stations. All data are streamed back to a single computer using the Freewave radio modem. This radio modem is low power (less than 1 Watt transmitting power) and has a 115 Kbps data rate. GPS receivers record observations at consistent and synchronized intervals. The systems used in this project record data every second, at the beginning of the second. These data are all streamed to the central computer using Time Delay Multiple Access (TDMA) technology [*Lamb*, 1998]. This technology schedules a time for each transmitter to transfer its data packet back through the communications network. This allows all the data to be streamed through a single radio modem into the collection computer, providing an efficient and reliable method of data collection. Figure 20 displays both the fractional percentage of satellites tracked (upper panel) and the fractional percentage of total data collected for one station over a period of approximately 2.5 years. This figure shows the continuous operation of this station and its consistent collection of approximately 75% of all observations. The remaining 25% of data that is not collected are from satellites that are obstructed by local topography and vegetation. A data collection percentage of 100% would mean all satellites above the horizon were successfully tracked.

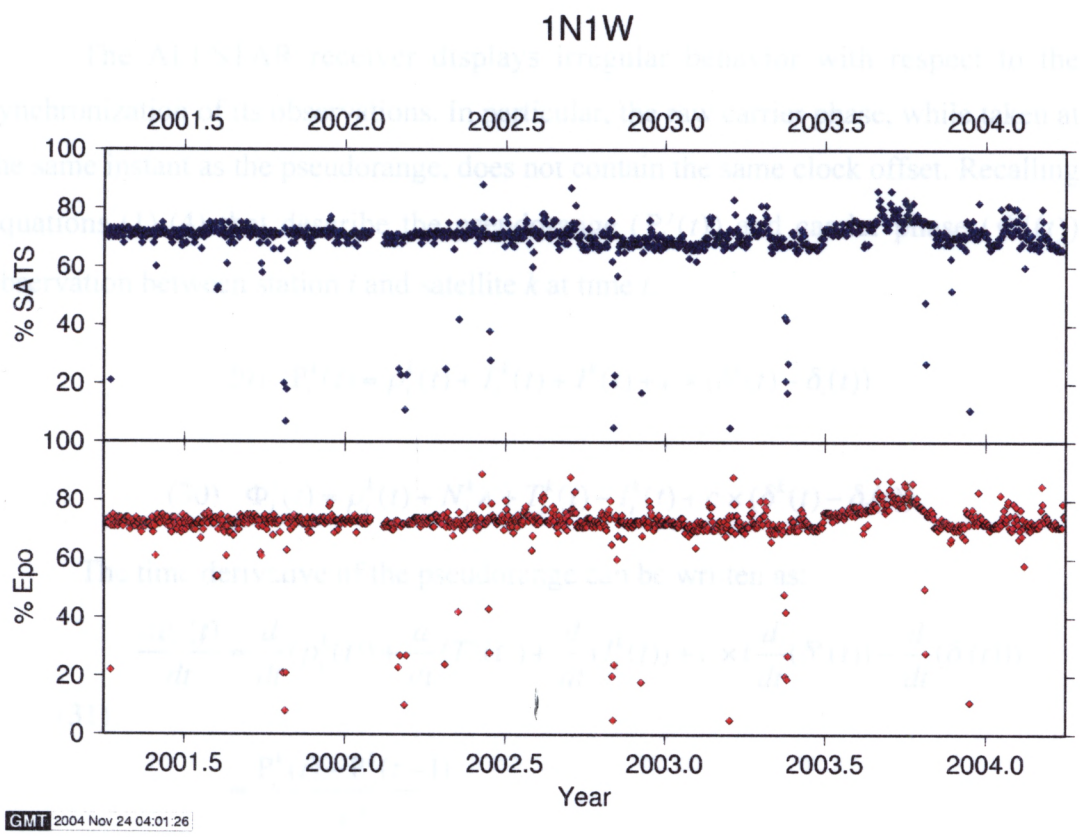

Figure 20: Data collection statistics for station 1N1W.

5.2.4 Power/Battery Backup

Each station has a solar panel with charge controller with a deep cycle battery for night operation and backup. The batteries are rated for 60 amp-hours. The power consumption of the GPS receiver and radio transceiver is 272 mA using a 12 Volt input power supply. These characteristics are determined from the manufacturers specifications. This combination of battery backup and maximum power consumption allows for approximately 4.5 days of operation with 50% battery consumption. This robust power system was selected to minimize any loss of data due to poor weather conditions. Currently, these systems have displayed excellent behavior and consistent operation.

5.3 CMC Receiver Performance

The ALLSTAR receiver displays irregular behavior with respect to the synchronization of its observations. In particular, the raw carrier phase, while taken at the same instant as the pseudorange, does not contain the same clock offset. Recalling equations (1)-(4) that describe the pseudorange ($P_i^j(t)$) and carrier phase ($\Phi_i^j(t)$) observation between station *i* and satellite *k* at time *t*.

$$(29)\quad P_i^k(t) = \rho_i^k(t) + T_i^k(t) + I_i^k(t) + c \times (\delta^k(t) - \delta_i(t))$$

$$(30)\quad \Phi_i^k(t) = \rho_i^k(t) + N_i^k\lambda + T_i^k(t) - I_i^k(t) + c \times (\delta^k(t) - \delta_i(t))$$

The time derivative of the pseudorange can be written as:

$$(31)\quad \frac{dP_i^k(t)}{dt} = \frac{d}{dt}(\rho_i^k(t)) + \frac{d}{dt}(T_i^k(t)) + \frac{d}{dt}(I_i^k(t)) + c \times (\frac{d}{dt}(\delta^k(t)) - \frac{d}{dt}(\delta_i(t))) \approx \frac{P_i^k(t) - P_i^k(t-1)}{\Delta t}$$

The time derivative of the carrier phase is similarly written:

$$(32)\quad \frac{d\Phi_i^k(t)}{dt} = \frac{d}{dt}(\rho_i^k(t)) + \frac{d}{dt}(N_i^k\lambda) + \frac{d}{dt}(T_i^k(t)) - \frac{d}{dt}(I_i^k(t)) + c \times (\frac{d}{dt}(\delta^k(t)) - \frac{d}{dt}(\delta_i(t))) \approx \frac{\Phi_i^k(t) - \Phi_i^k(t-1)}{\Delta t}$$

The ambiguity in the carrier phase observation is a constant, therefore it's time derivative is zero. Differencing these two equations and collecting terms yields the following equation.

$$(33)\quad \frac{dP_i^k(t)}{dt} - \frac{d\Phi_i^k(t)}{dt} = 2\frac{d}{dt}(I_i^k(t)) + c \times (\frac{d}{dt}(\delta^k(t)) - \frac{d}{dt}(\delta_i(t)) - c \times (\frac{d}{dt}(\delta^k(t)) - \frac{d}{dt}(\delta_i(t))$$

The range and troposphere components difference out when combing the two observation types. The non-zero terms remaining are twice the ionospheric derivative,

and the difference in clock errors between the pseudorange and carrier phase. Recall that the ionosphere appears as an increase in length for a pseudorange measurement, and a decrease in length for a carrier phase measurement. This difference arises from the fact that a pseudorange travels at the speed defined by the group delay and the carrier phase travels at a speed defined by the phase velocity. The satellite clock error is assumed to difference out because it originates from the satellite, which common to both the pseudorange and carrier phase. The remaining terms represent twice the change in ionosphere, and the difference between the pseudorange and carrier phase receiver clock error.

$$(34)\quad \frac{d\mathrm{P}_i^k(t)}{dt} - \frac{d\Phi_i^k(t)}{dt} = 2\frac{d}{dt}\left[I_i^k(t)\right] + c \times \left[\frac{d}{dt}(\delta_i(t)_\Phi - \delta_i(t)_P)\right]$$

If the median of this offset is determined, it represents the drift in receiver clock error between the carrier phase and pseudorange. The median calculation prevents data gaps or cycle slips from corrupting the computation. The time offset is actually computed by first determining the median value of the offset, then finding all the observations that fall within 3 times the stated precision of the receiver and computing the mean value for this subset of observations. The modification of either the carrier phase, or the pseudorange and time tag, by this integration offset will synchronize all the observations from the receiver.

The change in ionosphere in equation (34) is different to each satellite. In the computation of the median value, the ionosphere to each satellite is assumed to combine to be a value nearly equal to zero. Over a few minutes, this is essentially true. Throughout the course of a day, as the TEC increases and decreases with the rise and set of the sun, the time integral of the ionosphere term will degrade the computed clock correction. This error will remain in the corrected observations, but will be much smaller in magnitude than the clock error. For precise point positioning applications, the integral of the clock correction must be reset every few hours to minimize the error originating from the integration of the ionosphere (Jim Johnson, personal communication).

The Novatel SUPERSTAR is a similar, but slightly newer, receiver than the ALLSTAR. In its user manual, a method is described where the clock slew rate is

used to modify the carrier phase observations. This adjustment synchronizes the phase and pseudorange, which then eliminates the need for the steps described above. The method described in the SUPERSTAR manual will also work for the ALLSTAR (Jim Johnson, personal communication). The caveat is that the data stream coming from the receiver must be continuous. The systems deployed in Oklahoma stream their data to a central collection computer without error correction or redundancy. This results in some of the observations being lost in transmission, making the slew rate correction unreliable.

For double difference processing, the synchronization step is not necessarily needed. The clock error differences out when carrier phase measurements from one station and two satellites are differenced. However, the synchronization of the observations helps in cycle slip detection (especially when checking for slips on the single difference level). In precise point positioning processing [*Zumberge et al.*, 1997], where the pseudoranges are used to model the receiver clock error, this synchronization step is important (K. Larson, personal communication).

5.4 Processing Strategy

It is difficult to use single frequency GPS data to retrieve PW and SW. With only one frequency, the ionosphere cannot be removed with the standard linear combination of L_1 and L_2 carrier phase observations (see equation (5)). The ionosphere will induce a scale contraction on the carrier phase that will be larger than the delay caused by the neutral atmosphere (PW/SW). This problem is solved with the use of Global Ionosphere Models (GIMs) produced by the Center for Orbit Determination in Europe (CODE) [*Schaer*, 1999]. These models are generated daily, and describe the ionosphere with a set of spherical harmonics of degree and order 15. The time resolution is two hours. While GIMs remove large-scale ionospheric errors, small-scale variations in the ionosphere will not be resolved using this global model. These small-scale ionospheric errors are minimized with double difference processing using stations that are less than 10 km apart. In effect, the small-scale error in the GIM model is eliminated with double difference processing if the baseline lengths are kept short. This theory assumes that the ionosphere does not contain measurable

differences over distances of less than 10 km. The validity of this assumption is addressed in the results presented in Section 5.8.

Short baselines eliminate ionospheric errors that remain in GIMs. However, the analysis of GPS data using a small network of stations will result in troposphere values (PW and SW) that are accurate only in a relative sense. Absolute PW and SW estimates require the use of GPS stations spaced over a distance of at least 500 km [*Rocken et al.*, 1993]. This problem is solved by nesting the single frequency network within a continental scale network of dual frequency stations. This strategy is represented in Figure 21. A dual frequency GPS station is located approximately 30 meters away from one of the single frequency stations at the ARM CF. This station is included in the analysis of both the single frequency data, and the dual frequency data. The short distances between single frequency stations (and the one dual frequency station at the ARM CF) and the GIM model accurately removes the ionosphere. The continental network of dual frequency stations allows for the absolute determination of PW and SW.

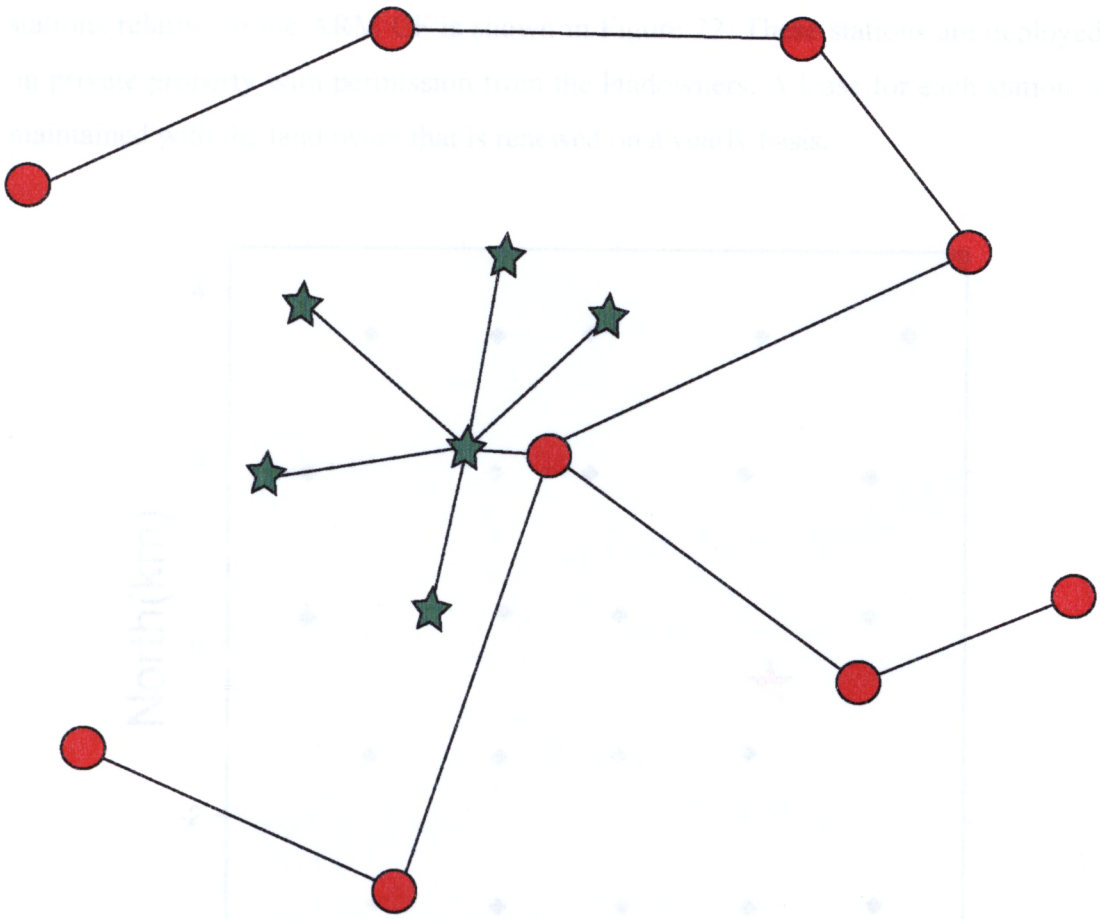

Figure 21: Diagram of baseline formation using single frequency stations (green) and dual frequency stations (red).

5.5 Network Deployment

Twenty-four GPS stations were deployed around the ARM CF near Lamont, OK. This region of the country is primarily agricultural, sparsely populated, and most of the land is used for either crops or livestock grazing. The road system around the CF consists primarily of farm access roads, organized along section lines within the county. Almost all roads run either north-south or east-west with a spacing of exactly one mile. Most sections are divided into quarters. The stations were deployed around the CF along these farm roads. They are placed on east-west running county roads, at the boundary between quarter sections. This allows station placement near the roads for easy access while also being positioned in the corner of one of the quarter sections. This corner location ensured that large farming machinery would not disturb the systems. The stations were fenced to systems from livestock. A map of the

stations relative to the ARM CF is shown in Figure 22. These stations are deployed on private property with permission from the landowners. A lease for each station is maintained with the landowner that is renewed on a yearly basis.

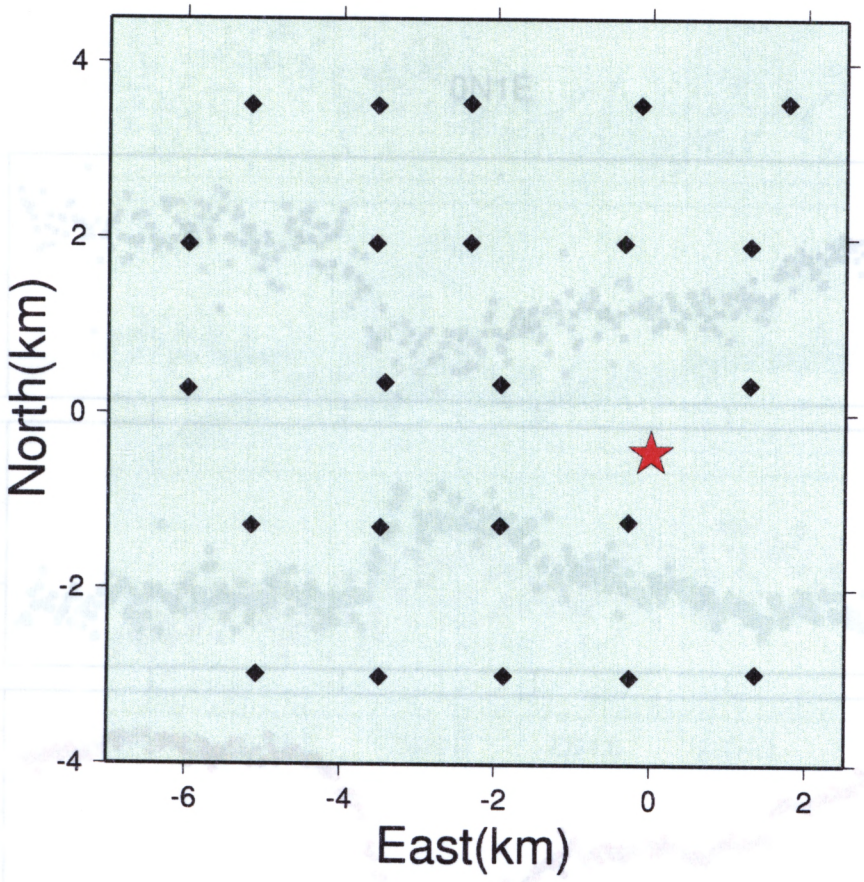

Figure 22: Map of single frequency GPS stations (black diamonds) relative to ARM SGP central facility (red star).

5.6 Geodetic Results

One way to assess the capabilities of a GPS receiver is compute the scatter in the position estimates from one day to the next. Figure 23 and Figure 24 show the time series of station positions for two different sites. These time series indicate that the weekly repeatability of the stations is less than 2 mm RMS in their horizontal components, and less than 5 mm in the vertical component. These results are encouraging and show that the stations are of high quality. The long-term drift of the coordinates in Figure 23 is caused by monument motion. This wandering of the

station over seasons is due to the shallow depth of the monuments (approximately 1 meter). Variations in soil moisture are most likely the source of this station variation. Updating the a priori coordinates used in the analysis prevents this monument instability from affecting the accuracy of the atmospheric solutions.

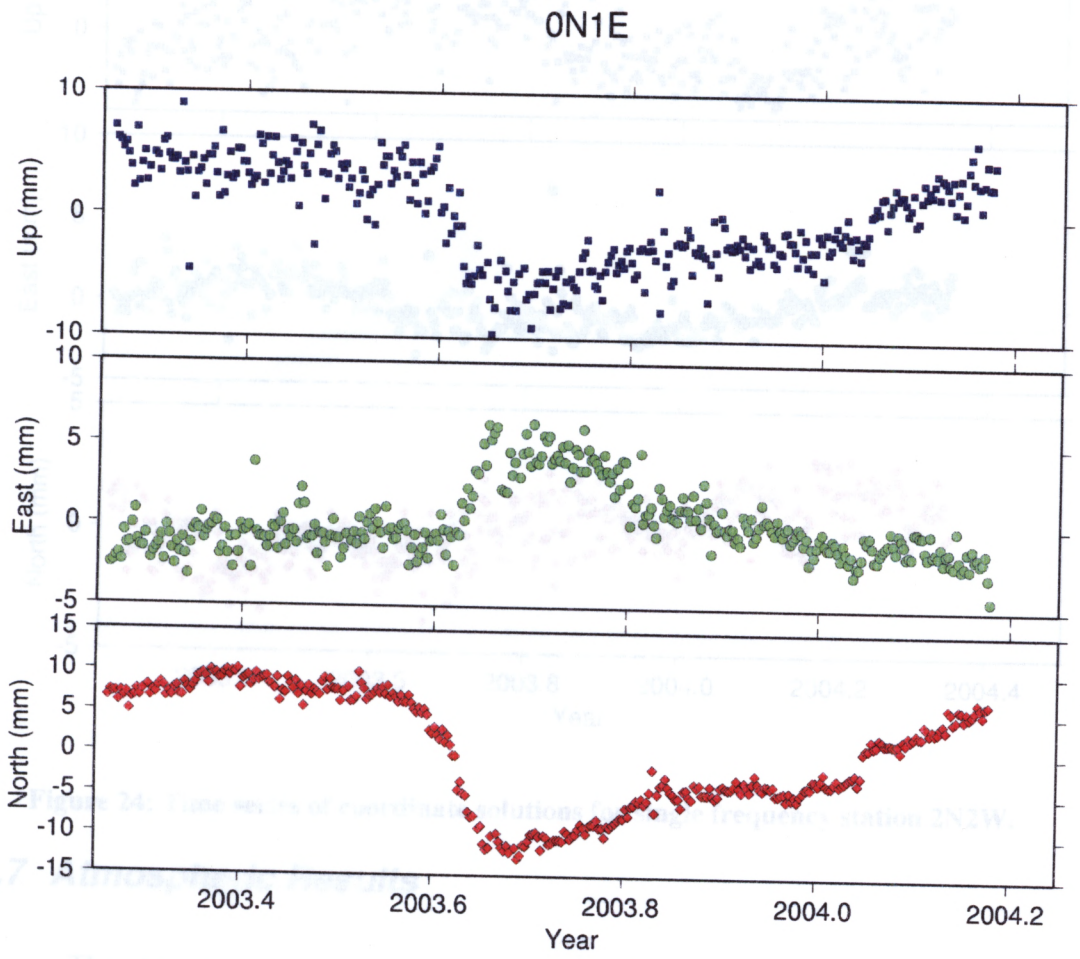

Figure 23: Time series of coordinate solutions for single frequency station 0N1E.

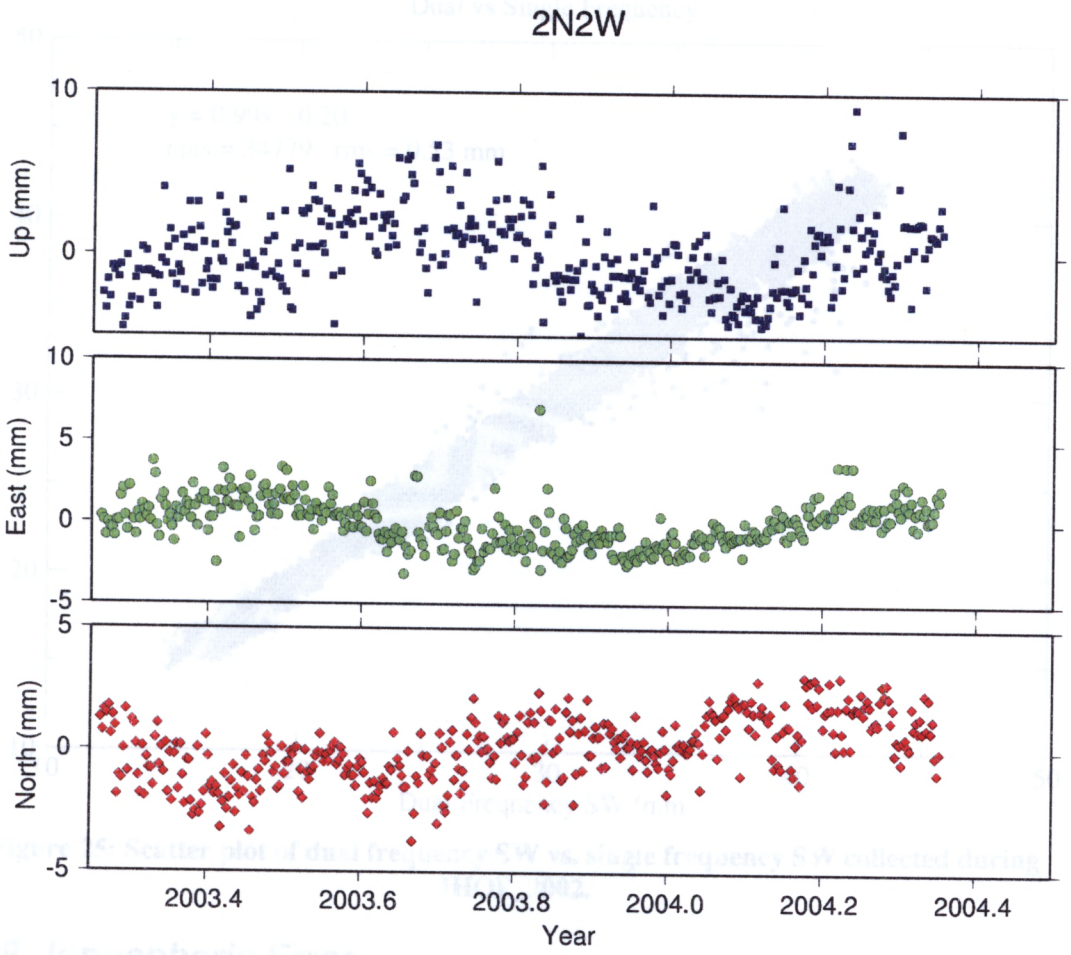

Figure 24: Time series of coordinate solutions for single frequency station 2N2W.

5.7 Atmospheric Results

The objective of developing and operating these GPS stations was to measure atmospheric water vapor with accuracy and precision that is comparable to the traditional dual frequency systems. To assess the capability of these systems, SW from a single frequency station was compared to SW measured with a dual frequency GPS system stationed approximately 30 meters away. A scatter plot comparison for data collected during IHOP_2002 is shown in Figure 25. The agreement between the two stations is quite good, with an RMS difference of 0.53 mm in zenith scaled SW. This comparison implies that the single frequency results are of similar quality as the dual frequency results.

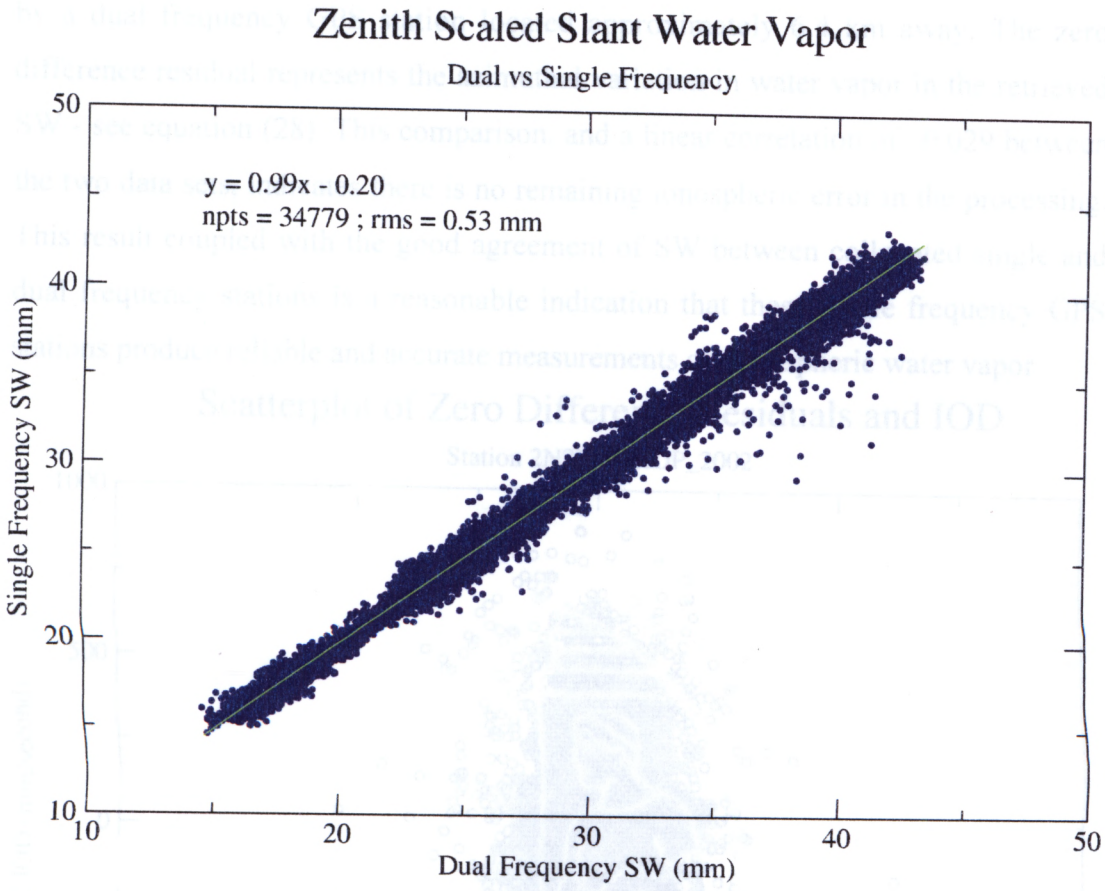

Figure 25: Scatter plot of dual frequency SW vs. single frequency SW collected during IHOP_2002.

5.8 Ionospheric Error

As mentioned earlier, errors in the retrieved geodetic and atmospheric parameters that might be caused by the ionosphere are eliminated with the use of GIM models and short baseline lengths. The GIM removes large-scale errors and the short baselines ensure that small-scale ionospheric structures are differenced away. The data translation software TEQC [*Estey and Meertens*, 1999] contains a set of quality check routines that can be used to test this strategy. Using dual frequency GPS observations, TEQC can compute the time rate of change of the ionosphere. A rapidly changing ionosphere, measured by a receiver tracking a satellite as it moves across the sky, implies the existence of small-scale variations. This ionospheric derivative (IOD) can be used as a proxy for the spatial variability. Figure 26 plots the zero difference residuals from a single frequency GPS station against the IOD as measured

by a dual frequency GPS station located approximately 6.4 km away. The zero difference residual represents the azimuthal variation in water vapor in the retrieved SW - see equation (28). This comparison, and a linear correlation of –0.029 between the two data sets, indicates there is no remaining ionospheric error in the processing. This result coupled with the good agreement of SW between collocated single and dual frequency stations is a reasonable indication that these single frequency GPS stations produce reliable and accurate measurements of atmospheric water vapor.

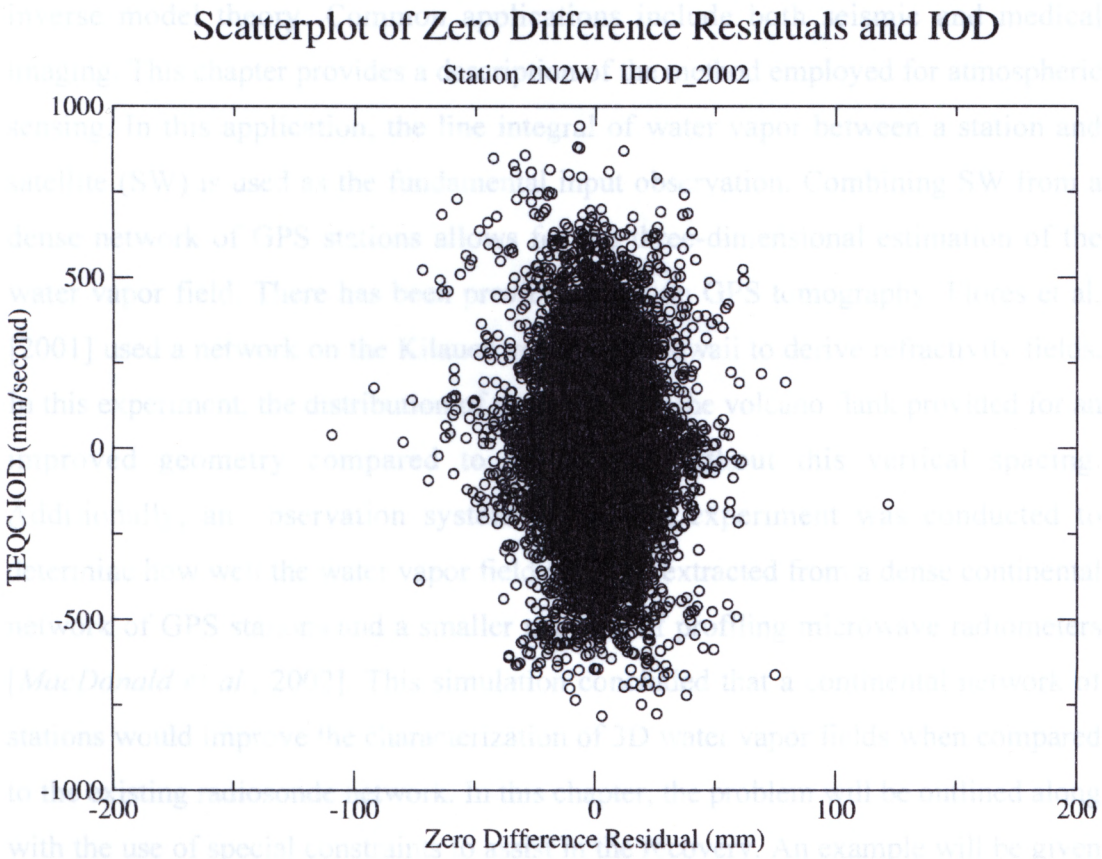

Figure 26: Scatter plot of zero difference residuals from a single frequency station and the rate of change of the ionosphere.

Chapter 6: Tomography of the Atmosphere

6.1 Overview

This chapter describes the tomographic method used to generate three-dimensional estimates of the water vapor field. Tomography is an application of inverse model theory. Common applications include both seismic and medical imaging. This chapter provides a description of the method employed for atmospheric sensing. In this application, the line integral of water vapor between a station and satellite (SW) is used as the fundamental input observation. Combining SW from a dense network of GPS stations allows for the three-dimensional estimation of the water vapor field. There has been previous work on GPS tomography. Flores et al. [2001] used a network on the Kilauea volcano in Hawaii to derive refractivity fields. In this experiment, the distribution of stations along the volcano flank provided for an improved geometry compared to a network without this vertical spacing. Additionally, an observation system simulation experiment was conducted to determine how well the water vapor field could be extracted from a dense continental network of GPS stations and a smaller network of profiling microwave radiometers [*MacDonald et al.*, 2002]. This simulation concluded that a continental network of stations would improve the characterization of 3D water vapor fields when compared to the existing radiosonde network. In this chapter, the problem will be outlined along with the use of special constraints to assist in the recovery. An example will be given that illustrates the technique and defines its capabilities and limitations.

6.2 The Inverse Problem

SW represents the integrated amount of water vapor between a GPS satellite (k) and a receiving antenna (i), scaled to its equivalent amount of liquid water.

$$(35) \quad SW_i^k = \frac{1}{\rho}\int_L \rho_v(s) \bullet ds$$

Partitioning the atmosphere into relatively small three-dimensional volumes of atmosphere, or voxels, and assuming the water vapor is constant within the voxel allows for the approximation of SW with a Riemann sum.

$$(36)\quad SW_i^k = \int_L \rho \bullet ds \approx \sum_{l=1}^{n} \rho_l \bullet \Delta s_l$$

A schematic representation of this approximation is illustrated in Figure 27. The use of voxels implies that integrated water vapor can be accurately described by the average vapor density within the voxels. It is assumed that there is no water vapor above the top layer of voxels. The line integral is considered a straight line between the station and the satellite. In reality the path of the GPS signal, and therefore the SW integral, is somewhat curved. This error in the representation of SW as a straight-line integral is very small for ground based GPS measurements above 5° elevation angle and is neglected in this research. The effects of bending will need to be accounted for when low elevation data are eventually used in atmospheric studies.

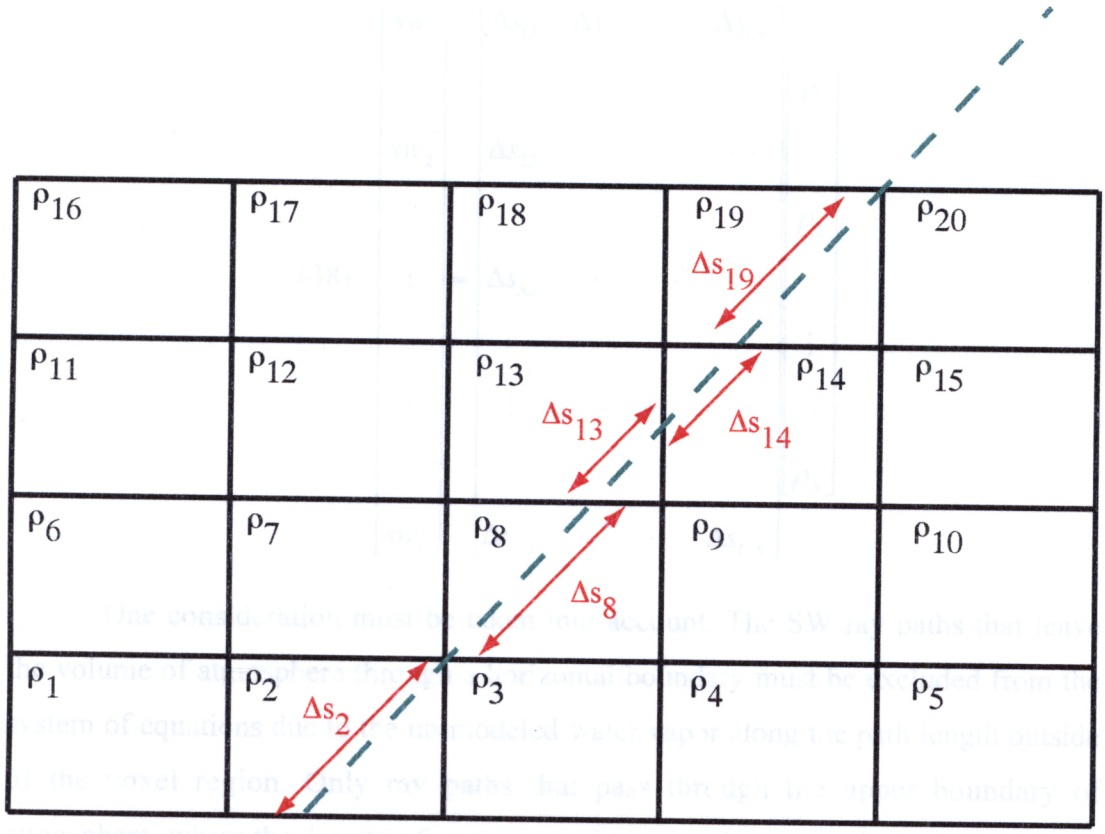

$$SW = \sum (\rho_l * \Delta s_l) = \rho_2 \Delta s_2 + \rho_8 \Delta s_8 + \rho_{13} \Delta s_{13} + \rho_{14} \Delta s_{14} + \rho_{19} \Delta s_{19}$$

Figure 27: Cartoon representation approximating SW measurement within voxels.

Deploying a network of stations in a region and deriving SW from each station to all visible satellites generates a collection of observations that can be combined into a system of linear equations.

$$(37) \quad \mathbf{SW} = \mathbf{H}\boldsymbol{\rho}$$

The matrix representation would consist of a single column matrix representing SW (**SW**), the design matrix representing the path length of each SW value through the individual voxels (**H**), and a single column matrix with the density of water vapor within the individual voxels (ρ).

$$(38)\quad \begin{bmatrix} sw_1 \\ sw_2 \\ \vdots \\ \vdots \\ sw_L \end{bmatrix} = \begin{bmatrix} \Delta s_{1,1} & \Delta s_{1,2} & \cdots & \Delta s_{1,N} \\ \Delta s_{2,1} & \cdots & \cdots & \cdots \\ \Delta s_{3,1} & \cdots & \cdots & \cdots \\ \vdots & \cdots & \cdots & \cdots \\ \Delta s_{L,1} & \cdots & \cdots & \Delta s_{L,N} \end{bmatrix} \begin{bmatrix} \rho_1 \\ \rho_2 \\ \vdots \\ \rho_N \end{bmatrix}$$

One consideration must be taken into account. The SW ray paths that leave the volume of atmosphere through a horizontal boundary must be excluded from the system of equations due to the un-modeled water vapor along the path length outside of the voxel region. Only ray paths that pass through the upper boundary of atmosphere, where the density of water vapor is assumed zero, can be included.

If the geometry of the of SW ray paths is sufficient, the water vapor density of the voxels can be determined through a least squares estimation of the system of equations in (38). There are two reasons why GPS produces a system of linear equations that are almost never full rank. First, it is nearly impossible to have ray paths that intersect all voxels. This leaves a subset of voxels not described by the linear system of equations. Second, an ambiguity exists in the vertical partitioning of the water vapor profile that makes the retrieval of the absolute profile difficult when only using ground based GPS. The next two sections describe how these two problems are overcome.

6.3 Horizontal Constraints

The condition where the rank of the design matrix **H** becomes full is almost never realized using only GPS observations. One significant problem is the representation of the water vapor density in voxels that are not pierced by an SW ray path. Un-sampled voxels generally occur when the spacing of the GPS stations is

much larger than the horizontal voxel size and along the boundary of the tomography region. With a sufficiently dense network of stations, like the single frequency one installed around the ARM CF in Oklahoma, the voxels that do not have ray paths passing through them are typically located along the outside boundary. Figure 28 counts the number of SW ray paths that pass through each voxel and originate from different stations. There are 36 voxels in each layer (6x6) with a voxel size of approximately 1 km^2. In the figure, the voxels are organized by horizontal layer, with 36 voxels in each layer and 18 vertical layers. Voxel 1 is in the northwest most voxel; voxel 36 is the southeast most voxel. The plot is made using 10 minutes of observations, with a 120 second sample period (5 epochs). Most of the voxels are pierced by ray paths from only one or two stations. The voxels that are not pierced are typically the ones along the outer boundary of the tomography region.

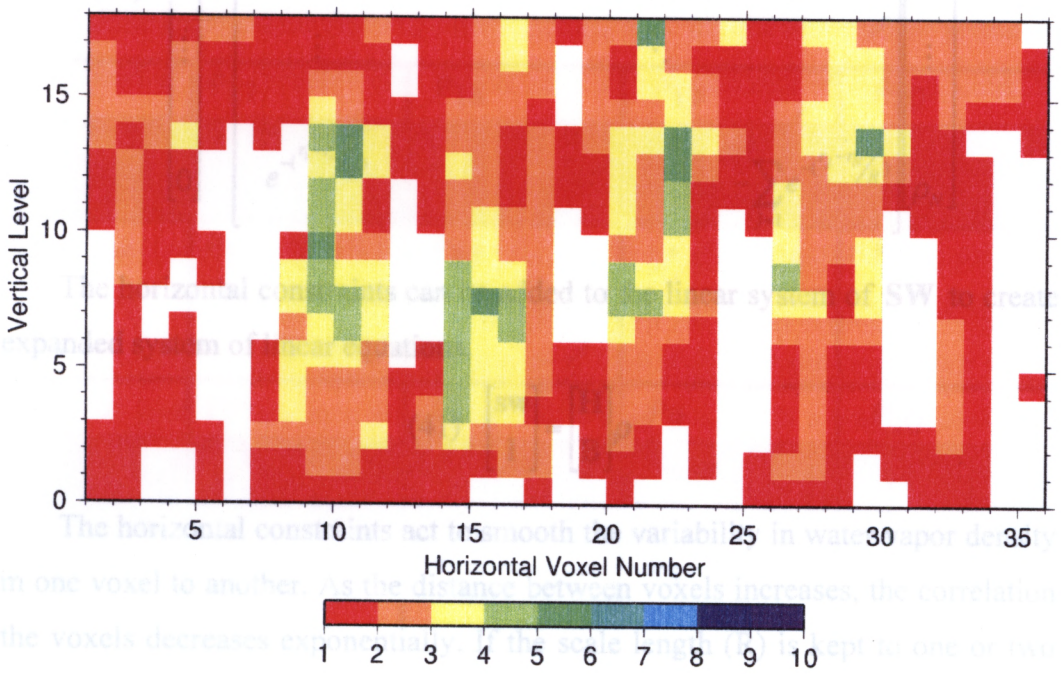

Figure 28: Graphical representation of the number of different stations containing a ray path passing through each voxel.

The addition of constraints defines the water vapor density in voxels that are not pierced by SW ray paths by relating the water vapor in a voxel to nearby voxels in the same horizontal layer. This horizontal constraint (l_i) for any voxel (i) that is applied in this problem is a Gaussian smoothing constraint.

$$(39)\quad l_i = \sum_{j=1}^{N} e^{-(r_j - r_i)/R}, i \neq j$$

Where r_i is the vector location of the spatial center of voxel i and r_j is the spatial center of voxel j. The scale distance (R) is selected based on the station spacing and voxel size. A typical value is 1.5 times the horizontal length of a voxel. A constraint is included into the linear system of equations for each voxel. In matrix form, the system of constraints resembles (40).

$$(40)\quad \begin{bmatrix} 0 \\ 0 \\ \vdots \\ 0 \end{bmatrix} = \begin{bmatrix} -\sum_{j=1} e^{-(r_j - r_1)/R} & e^{-(r_2 - r_1)/R} & \cdots & e^{-(r_N - r_1)/R} \\ e^{-(r_1 - r_2)/R} & -\sum_{j=1} e^{-(r_j - r_2)/R} & e^{-(r_3 - r_2)/R} & e^{-(r_N - r_1)/R} \\ \vdots & & \ddots & \\ e^{-(r_1 - r_N)/R} & & & -\sum_{j=1} e^{-(r_j - r_N)/R} \end{bmatrix} \begin{bmatrix} \rho_1 \\ \rho_2 \\ \vdots \\ \rho_N \end{bmatrix}$$

The horizontal constraints can be added to the linear system of **SW** to create an expanded system of linear equations.

$$(41)\quad \begin{bmatrix} \mathbf{sw} \\ \mathbf{l} \end{bmatrix} = \begin{bmatrix} \mathbf{H} \\ \mathbf{B} \end{bmatrix} \boldsymbol{\rho}$$

The horizontal constraints act to smooth the variability in water vapor density from one voxel to another. As the distance between voxels increases, the correlation of the voxels decreases exponentially. If the scale length (R) is kept to one or two voxel lengths, there will be almost no correlation in voxels on opposite sides of a horizontal layer. The choice of horizontal constraints is preferred to vertical constraints because of the exponential decay of vapor density in the vertical direction. The improvement in resolving the vertical water vapor profile is described next.

6.4 Improvement of the Vertical Profile

Using a network of ground based GPS stations and simple straight-line geometry; it is impossible to determine the absolute profile of water vapor within a tomography region. The geometry of the GPS stations does not provide enough information on the vertical distribution of the water vapor field. This can be illustrated using Figure 29. If the tomography region contains a horizontally homogeneous layer of water vapor with constant thickness, it can be placed at any vertical level and produce the same integrated SW. This makes the tomography problem ill-conditioned and not uniquely solvable.

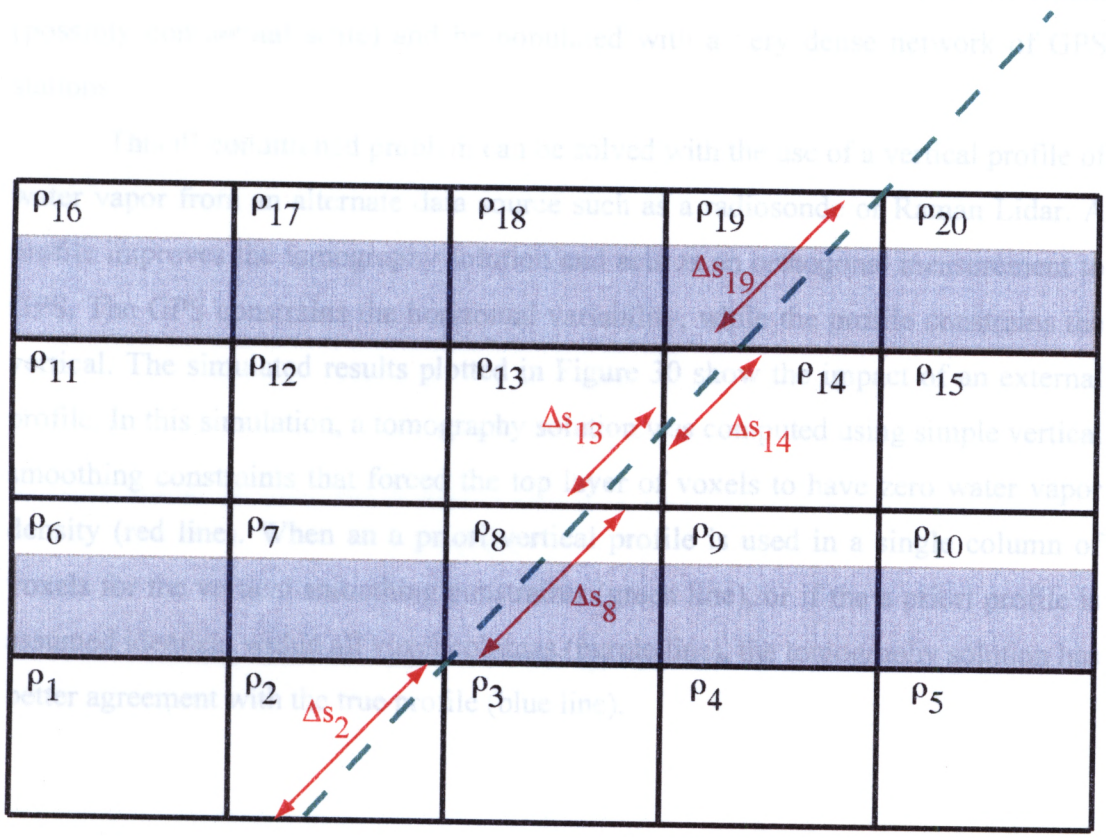

$$SW = \sum (\rho_l * \Delta s_l) = \rho_2 \Delta s_2 + \rho_8 \Delta s_8 + \rho_{13} \Delta s_{13} + \rho_{14} \Delta s_{14} + \rho_{19} \Delta s_{19}$$

Figure 29: A ground based GPS station would measure the same integrated SW for a homogeneous layer of water vapor located at any height.

There are two possible exceptions where vertical information may be determined exclusively with the use of GPS. The first situation is if the station

topography is variable in altitude so that a GPS receiver can be placed within each horizontal level of the tomography region. An example of this type of geometry is the research by Flores et al. [2001] where a line of stations runs along the edge of the volcano and into the dry upper troposphere. This situation is rare, and is not possible with in the majority of locations around the Earth. A second possible method to derive an absolute water vapor profile using only GPS would be when the horizontal extent of the tomography region was large enough so that the profile in one portion of the tomography area would be significantly different than another area, eliminating the possibility of a single homogenous layer extending across the entire tomography domain. This network would have to be many hundreds of kilometers in extent (possibly continental scale) and be populated with a very dense network of GPS stations.

This ill-conditioned problem can be solved with the use of a vertical profile of water vapor from an alternate data source such as a radiosonde or Raman Lidar. A profile improves the tomography solution and acts as an orthogonal measurement to GPS. The GPS constrains the horizontal variability, while the profile constrains the vertical. The simulated results plotted in Figure 30 show the impact of an external profile. In this simulation, a tomography solution was computed using simple vertical smoothing constraints that forced the top layer of voxels to have zero water vapor density (red line). When an a priori vertical profile is used in a single column of voxels for the vertical smoothing constraints (green line), or if the a priori profile is assumed identical within all voxel columns (purple line), the tomography solution has better agreement with the true profile (blue line).

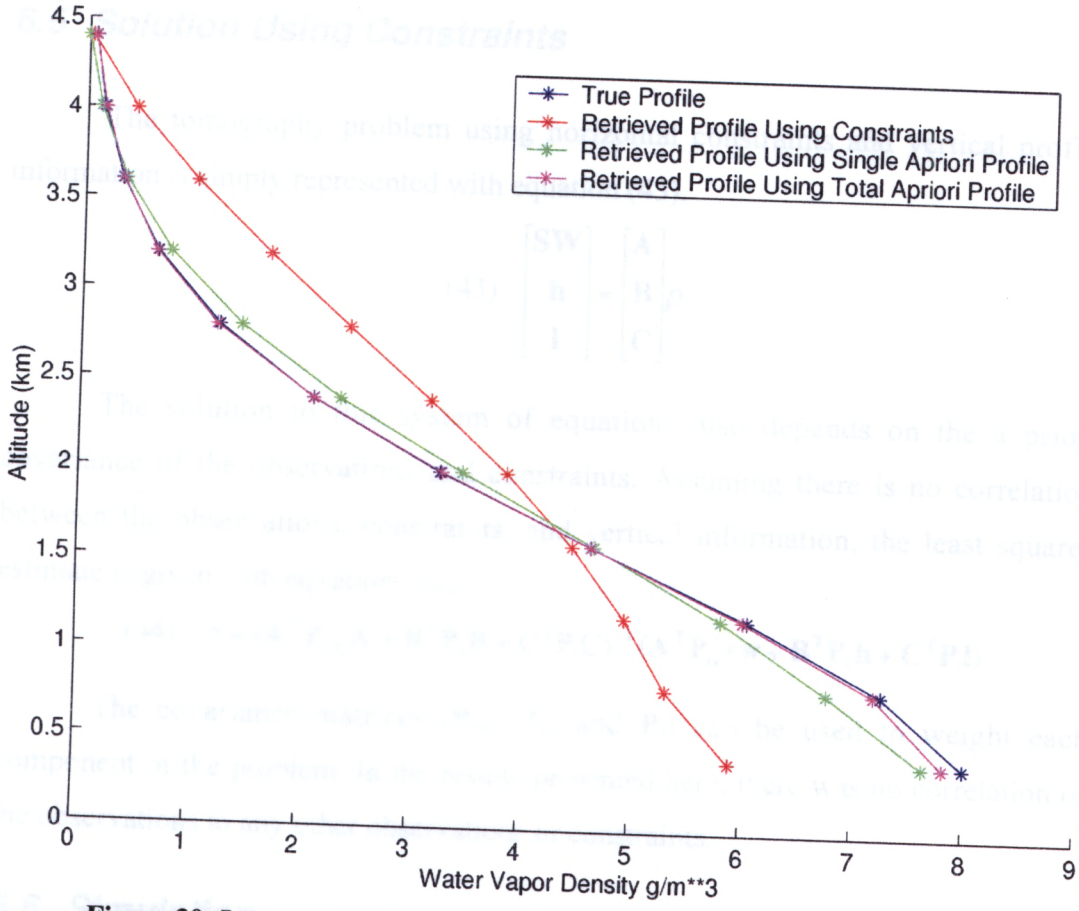

Figure 30: Improvement in Vertical Profile Using Additional Information

Profile information can be included into the linear system of equations simply by representing the observed density profile as a collection of pseudo-observations.

$$(42)\quad \begin{bmatrix} l_1 = \rho_0(\rho_1) \\ l_2 = \rho_0(\rho_2) \\ \vdots \\ l_N = \rho_0(\rho_N) \end{bmatrix} = \begin{bmatrix} 1 & 0 & \cdots & 0 \\ 0 & 1 & & \\ \vdots & & \ddots & \\ 0 & & & 1 \end{bmatrix} \begin{bmatrix} \rho_1 \\ \rho_2 \\ \vdots \\ \rho_N \end{bmatrix}$$

6.5 Solution Using Constraints

The tomography problem using horizontal constraints and vertical profile information is simply represented with equation (43).

$$(43)\quad \begin{bmatrix} \mathbf{SW} \\ \mathbf{h} \\ \mathbf{l} \end{bmatrix} = \begin{bmatrix} \mathbf{A} \\ \mathbf{B} \\ \mathbf{C} \end{bmatrix} \boldsymbol{\rho}$$

The solution to this system of equations also depends on the a priori covariance of the observations and constraints. Assuming there is no correlation between the observations, constraints, and vertical information, the least squares estimate is given with equation (44).

$$(44)\quad \boldsymbol{\rho} = (\mathbf{A}^{\mathrm{T}}\mathbf{P}_{SW}\mathbf{A} + \mathbf{B}^{\mathrm{T}}\mathbf{P}_{h}\mathbf{B} + \mathbf{C}^{\mathrm{T}}\mathbf{P}_{l}\mathbf{C})^{-1}(\mathbf{A}^{\mathrm{T}}\mathbf{P}_{sw}\mathbf{sw} + \mathbf{B}^{\mathrm{T}}\mathbf{P}_{h}\mathbf{h} + \mathbf{C}^{\mathrm{T}}\mathbf{P}_{l}\mathbf{l})$$

The covariance matrices ($\mathbf{P}_{sw}$, $\mathbf{P}_{h}$, and $\mathbf{P}_{l}$) can be used to weight each component of the problem. In the results presented here, there was no correlation of the observations to any other observations or constraints.

6.6 Simulation

A simulation was conducted to evaluate how well the single frequency network of stations could resolve the horizontal and vertical water vapor field. The simulation used a model atmosphere with peak density of 16 g/m^3 over the center of the network that radially decreased by 4 g/m^3 to the network edge. Vertically, this local maximum of water vapor decreased exponentially with a scale height of 4 km. There are two important similarities of this simulation to actual atmospheric conditions. First, the water vapor was concentrated within the lowest levels with an exponential decay with height. Second, the horizontal variations in vapor density were smaller than the vertical. The station and satellite geometry that was used to create Figure 28, which plots the number SW ray paths from different stations intersecting each voxel.

The scatter plot of simulated and retrieved vapor densities is plotted on the left in Figure 31. The right plot contains the vapor density of the simulated field (black)

and retrieved field (red) plotted as a function of voxel altitude. The profile from the column of voxels in the center of the region was used as the vertical constraint in the tomography solution. In the lowest tomography layer, the horizontal resolution of the solution is relatively poor. The simulated (left) and retrieved (right) fields for the lowest level are plotted in Figure 32. The simulated field changes by 4 g/m^3 in this layer. The retrieved field changes by less than 2 g/m^3. This poor resolution is caused by the lack of voxels containing SW ray paths from more than one station. The horizontal smoothing constraints and the vertical profile used in the solution dictate that this lowest level has relatively little variability. The simulated (left) and retrieved (right) fields within the vertical layer from 1.5 km to 2.0 km are plotted in Figure 33. As can be seen from this figure, the tomography works much better in this elevated layer. The retrieved maximum density is slightly south of the simulated maximum, but the tomography solution contains a horizontal pattern similar to the input field. In the simulation, the horizontal variability is approximately 2.5 g/m^3. In the retrieved field, it is 1.5 g/m^3. The outside edges of the solution, where there are voxel that are not pierced by SW ray paths, suffers from some smoothing.

Some obvious strengths and limitations of the tomography method can be inferred from this simulation. The lowest level of the solution is essentially driven by the smoothing constraints. The SW improves the solution at vertical layers where there is some overlap of ray paths from different stations. Within these layers, the tomography solution recreates the simulated field with reasonable quality.

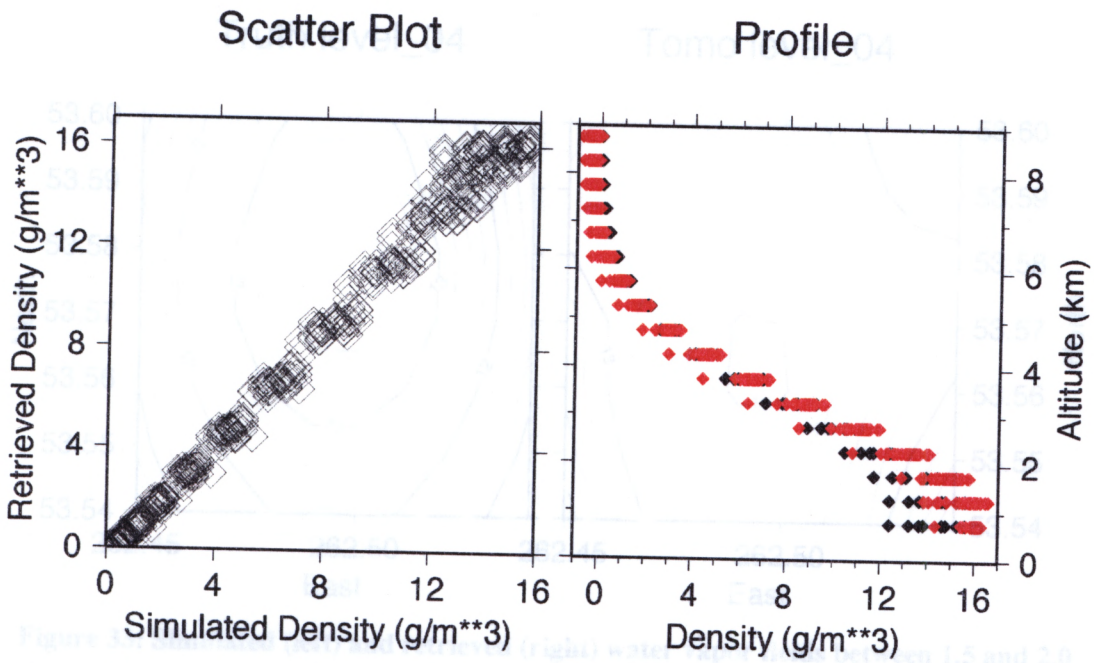

Figure 31: Scatter plot (left) of simulated vs. retrieved densities for each voxel. Density plotted as function of altitude (right) for simulated (black) and retrieved (red) values.

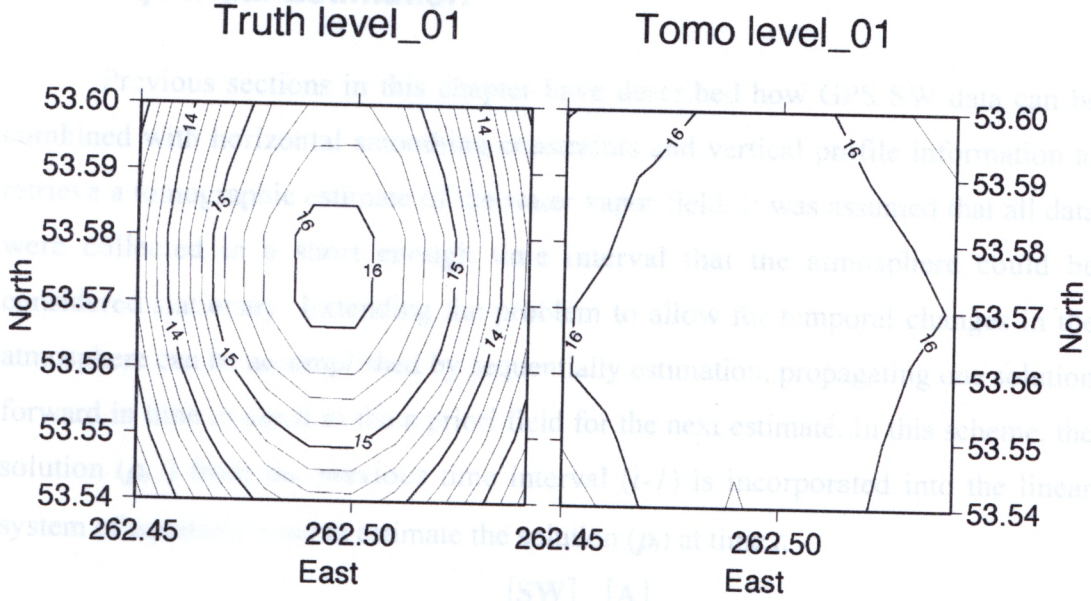

Figure 32: Simulated (left) and retrieved (right) water vapor fields for layer from ground level to 0.5 km.

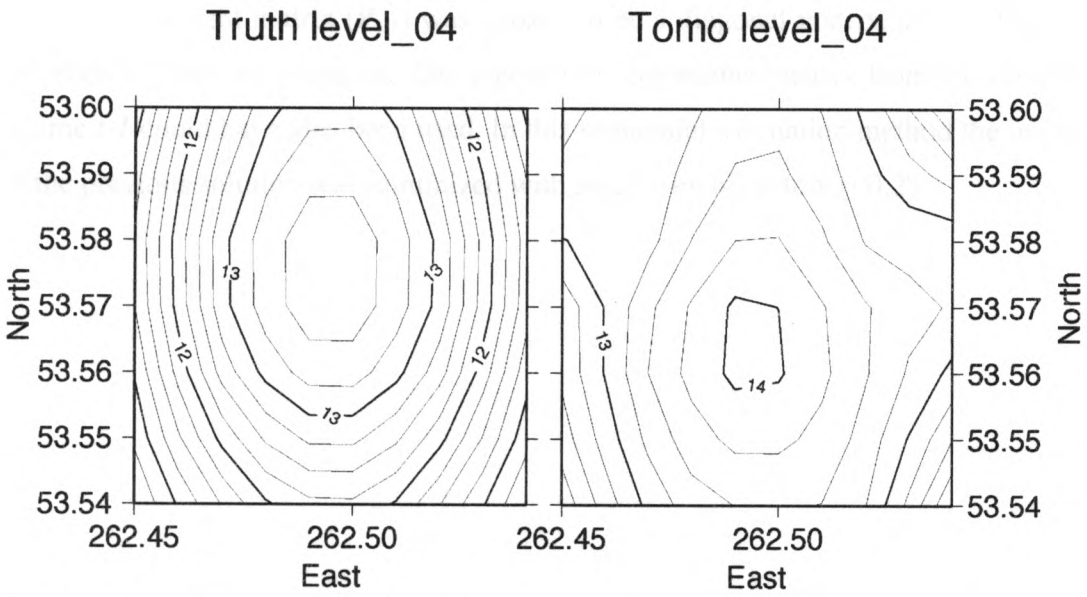

Figure 33: Simulated (left) and retrieved (right) water vapor fields between 1.5 and 2.0 km altitude.

6.7 Sequential Estimation

Previous sections in this chapter have described how GPS SW data can be combined with horizontal smoothing constraints and vertical profile information to retrieve a tomographic estimate of the water vapor field. It was assumed that all data were collected in a short enough time interval that the atmosphere could be considered stationary. Extending the problem to allow for temporal changes in the atmosphere can be accomplished by sequentially estimation, propagating one solution forward in time to use it as the a priori field for the next estimate. In this scheme, the solution ($\boldsymbol{\rho}_{t-1}$) from the previous time interval (t-1) is incorporated into the linear system of equations used to estimate the solution ($\boldsymbol{\rho}_t$) at time t.

$$(45) \quad \begin{bmatrix} \mathbf{SW} \\ \mathbf{h} \\ \mathbf{l} \\ \boldsymbol{\rho}_{t-1} \end{bmatrix} = \begin{bmatrix} \mathbf{A} \\ \mathbf{B} \\ \mathbf{C} \\ \mathbf{I} \end{bmatrix} \boldsymbol{\rho}_t$$

The estimate at time t-1 is updated to time t using the identity matrix ($\mathbf{I}$). The solution at time t is then computed with equation (46).

$$(46) \quad \boldsymbol{\rho}_t = (\mathbf{A}^T\mathbf{P}_{SW}\mathbf{A} + \mathbf{B}^T\mathbf{P}_h\mathbf{B} + \mathbf{C}^T\mathbf{P}_l\mathbf{C} + \mathbf{I}^T\mathbf{P}_{t-1}\mathbf{I})^{-1}(\mathbf{A}^T\mathbf{P}_{sw}\mathbf{sw} + \mathbf{B}^T\mathbf{P}_h\mathbf{h} + \mathbf{C}^T\mathbf{P}_l\mathbf{l} + \mathbf{I}^T\mathbf{P}_{t-1}\boldsymbol{\rho}_{t-1})$$

The weight matrix ($\mathbf{P}_{t-1}$) was chosen to be a diagonal matrix, eliminating the correlations between elements. The a posteriori covariance matrix from the estimate at time *t-1* could have also been used. In this sequential estimation method the impact of the previous solution was minimized with small weight factors (<0.2).

Chapter 7: The International H_20 Project (IHOP_2002)

7.1 Overview

The International H_20 Project (IHOP_2002) was a field experiment conducted in the Southern Great Plains region of the United States during May and June of 2002 [*Weckwerth et al.*, 2004]. The principal goals were to test and compare water vapor measurements from current research quality instruments and to improve warm season rainfall prediction through the careful study and application of data collected during case studies. The forecasting of warm season rainfall associated with convection initiation is the area of least skill for current numerical weather prediction [*Fritsch and Carbone*, 2004]. It is believed that a significant reason for this poor forecasting skill is the lack of detailed and precise observations of the water vapor field. There were more than 60 GPS stations operating during IHOP_2002. The results presented in this chapter illustrate the potential uses of GPS to improve the characterization of atmospheric water vapor. The examples shown illustrate the ability of GPS SW to observe small-scale boundary layer features, and tomography solutions imaged larger scale storm systems. The data collected during IHOP_2002 are also used to infer some statistical conclusions about the nature of atmospheric water vapor.

7.2 GPS Network

Several different groups were operating GPS networks in the SGP region during IHOP_2002. These include the continuously operating NOAA/FSL, UCAR's SuomiNet, and single frequency networks. Additionally, 7 GPS stations were deployed and operated for the majority of the experiment by Joel Van Baelen and his colleagues from CNRS France. Dave Whiteman from the Goddard Space Flight Center (GSFC) deployed a GPS station next to the GSFC scanning Raman Lidar in the Oklahoma panhandle region. A map of the stations operating during the project is shown in Figure 34. The black diamonds are the NOAA/FSL stations, the blue diamonds are the SuomiNet stations, and the red diamonds are the additional stations

deployed specifically for IHOP_2002. The single frequency network of stations are deployed around the ARM CF, circled in yellow but on a smaller horizontal scale. Data from all these stations were collected and analyzed to retrieve PW and SW during IHOP_2002. A subset of stations around the ARM central facility was used to compute tomography solutions.

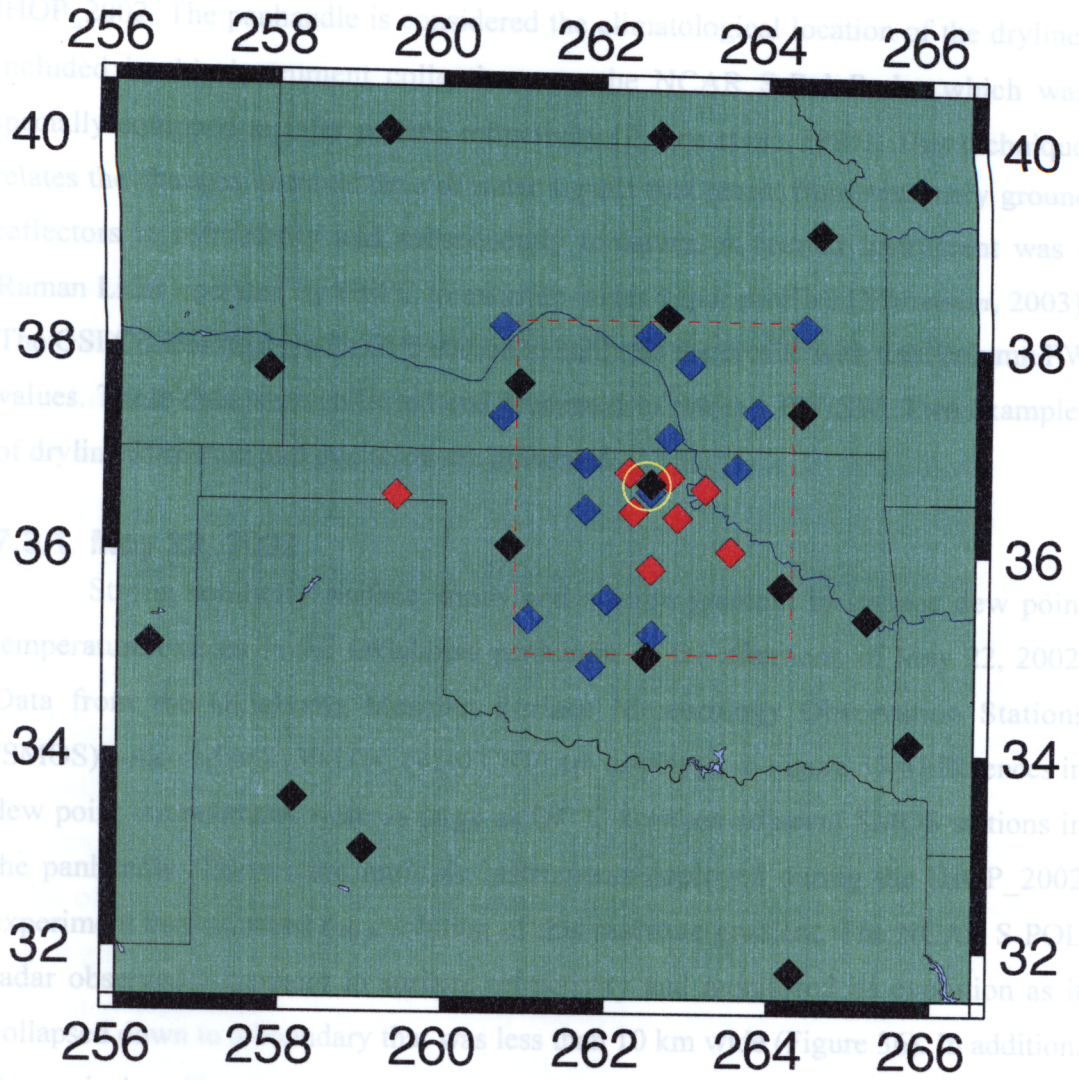

Figure 34: GPS stations in the Southern Great Plains region during the IHOP_2002 experiment.

7.3 Boundary Layer Structures – the Dryline

The dryline is a boundary between dry and moist air masses that usually extends vertically through a portion of the atmosphere [*McCarthy and Koch*, 1982;

Parsons et al., 1991]. The dryline that commonly occurs in the Southern Great Plains develops due to dry air that undergoes adiabatic heating as it subsides from the Rocky Mountains meeting moist air that is advected north and west from the Gulf of Mexico. It is frequently involved in the generation of large convective systems [*Hane et al.*, 1997; *Ziegler et al.*, 1997].

A suite of instruments was operating in the panhandle of Oklahoma during IHOP_2002. The panhandle is considered the climatological location of the dryline. Included in this instrument collection was the NCAR S-Pol Radar which was specially equipped to infer surface refractivity [*Fabry et al.*, 1997]. This technique relates the changes in travel time of radar signals that return from stationary ground reflectors to refractivity and subsequently moisture. A second instrument was a Raman Lidar operated by GSFC to measure water vapor profiles [*Whiteman*, 2003]. The GSFC Lidar deployed a GPS station to calibrate the profile with total column PW values. These data were collected and processed to retrieve PW/SW. Two examples of dryline formation and evolution are presented.

7.3.1 May 22, 2002

Strong southerly surface winds and a large gradient in surface dew point temperature existed in the Oklahoma panhandle in the afternoon of May 22, 2002. Data from the Oklahoma Mesonet Surface Meteorology Observation Stations (SMOS) collected at 2130 UTC (4:30 CST) are displayed in Figure 35. Differences in dew point temperatures were as large as 29° C between adjacent SMOS stations in the panhandle. There were multiple instruments deployed during the IHOP_2002 experiment that captured the evolution of this moisture gradient. The NCAR S-POL radar observed a gradient in surface refractivity and monitored its evolution as it collapsed down to a boundary that was less than 10 km wide (Figure 36). In addition, the vertical profile of water vapor mixing ratio measured with the GSFC Raman Lidar recorded large moisture fluctuations in the boundary layer between 2100 and 2400 UTC (Figure 37). These fluctuations coincided with the dryline moving above and across the field of view of the Lidar.

The data collected with GPS also showed the evolution of the dryline. The vertically scaled GPS SW from the panhandle station to all satellites are plotted as

blue diamonds in Figure 38. The half hour estimates of GPS PW are plotted as red diamonds. Between 1600 and 2100 UTC there was a general increase in total integrated moisture from 15 mm to 24 mm. The increase leveled off and varied between 20 and 25 mm for the rest of the day. The azimuthal variability in SW is seen to increase beginning around 1900 UTC. The variability is represented as the width of the blue diamonds at any instant in time. This increase coincided with the sharpening of the moisture gradient. GPS satellite PRN 03 passed low and to the west of the station from 2030 UTC to 2400 UTC. A plot of SW to PRN 03 is shown in red in Figure 39. The average of all vertically scaled SW is plotted as the black line for reference. It can be seen that between 2115 UTC and 2200 UTC the satellite passed through a region that was at times 3 mm dryer in vertically scaled integrated water vapor when compared to the average SW value. The satellite had a 30° elevation angle at 2130 UTC. The majority of water vapor existed in a boundary layer with a height of 1.5 km (derived from the GSFC Raman Lidar). This implies the gradient existed over a horizontal extent of approximately 2.6 km. Satellite PRN 09 rose above the south-east horizon around 2030 UTC and moved to the east of the station over the next four hours (Figure 40). During this time, the moisture field to the east of the station was generally larger than the average SW values, but there was significant variability observed in this direction too. Weckwerth et al [2004] attributed these rapid variations to mixing of dry and moist air to the east of the dryline. Variations in vertically scaled SW as large as 2.5 mm were observed over periods of less than 20 minutes. Satellite PRN 29 set below the northeast horizon at 2245 UTC. The time series of SW in the direction of this satellite is plotted in Figure 41. As the satellite sets, it goes through a portion of the atmosphere that contains 2 mm more in vertically integrated water vapor. The S-Pol radar showed a small cell of water vapor in the direction of the setting satellite (Figure 42), approximately 15-20 km away from the receiver. This cell is marked with the red arrow in the figure.

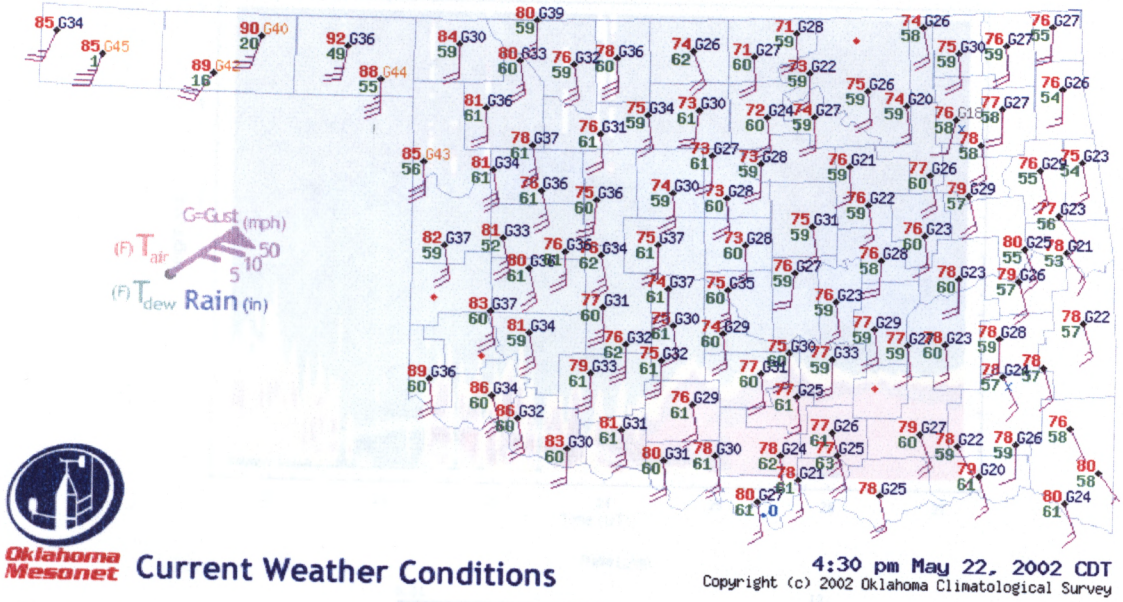

Figure 35: Surface conditions from the Oklahoma Mesonet at 21:30 UTC (4:30 CST) on May 22, 2002.

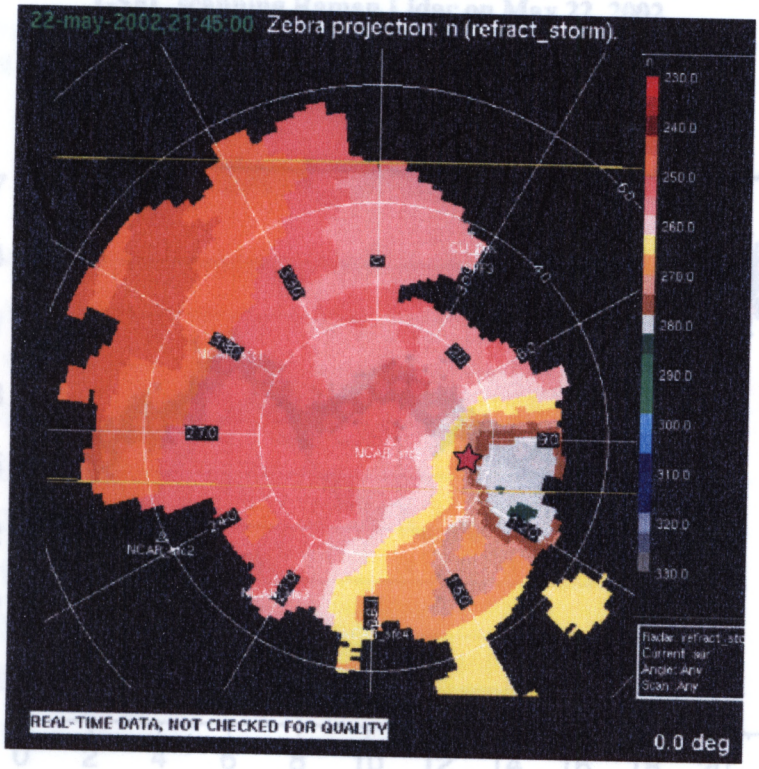

Figure 36: S-Pol surface refractivity field at 2145 UTC (4:45 CST) on May 22, 2002. The location of the GPS station is shown as the red star.

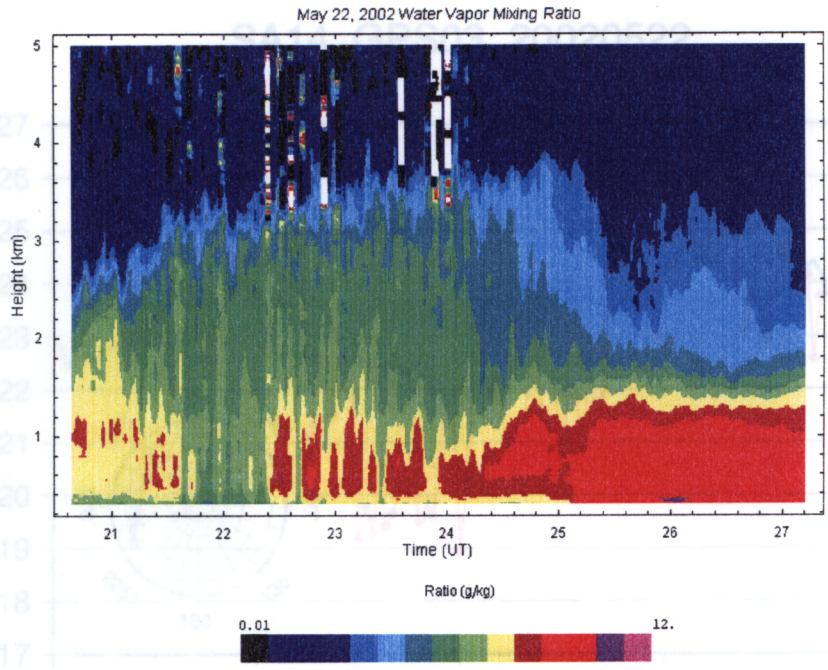

Figure 37: Time-height cross section of water vapor mixing ratio as measured by the GSFC scanning Raman Lidar on May 22, 2002.

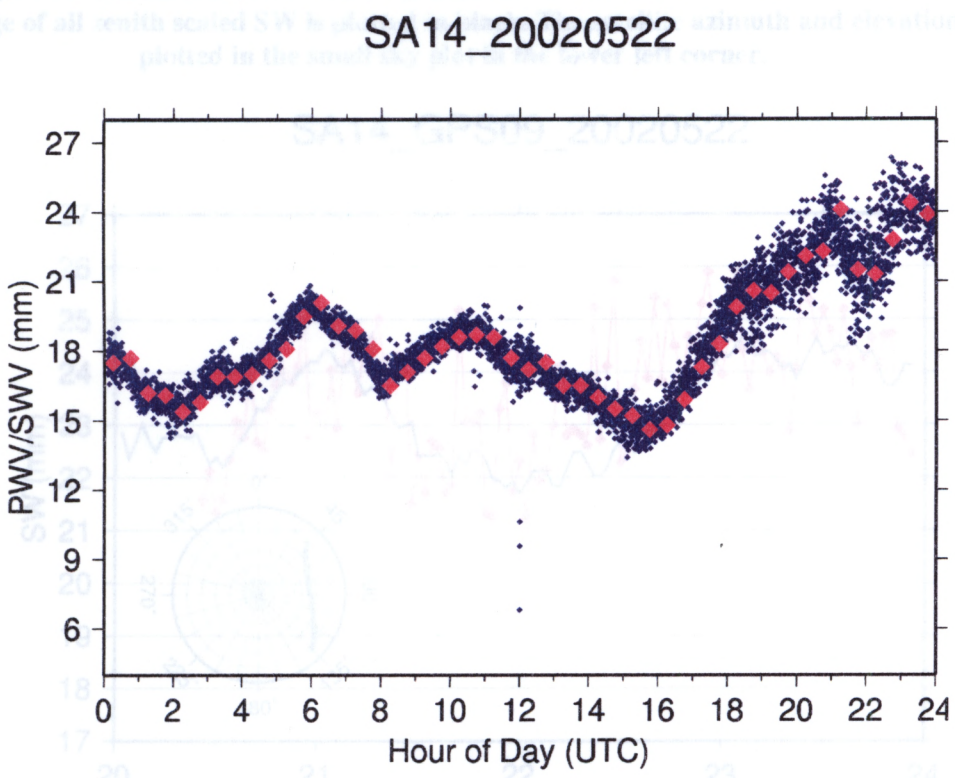

Figure 38: Vertically scaled GPS SW (blue diamonds) from the Oklahoma panhandle station SA14. The half hour GPS PW estimates are in red.

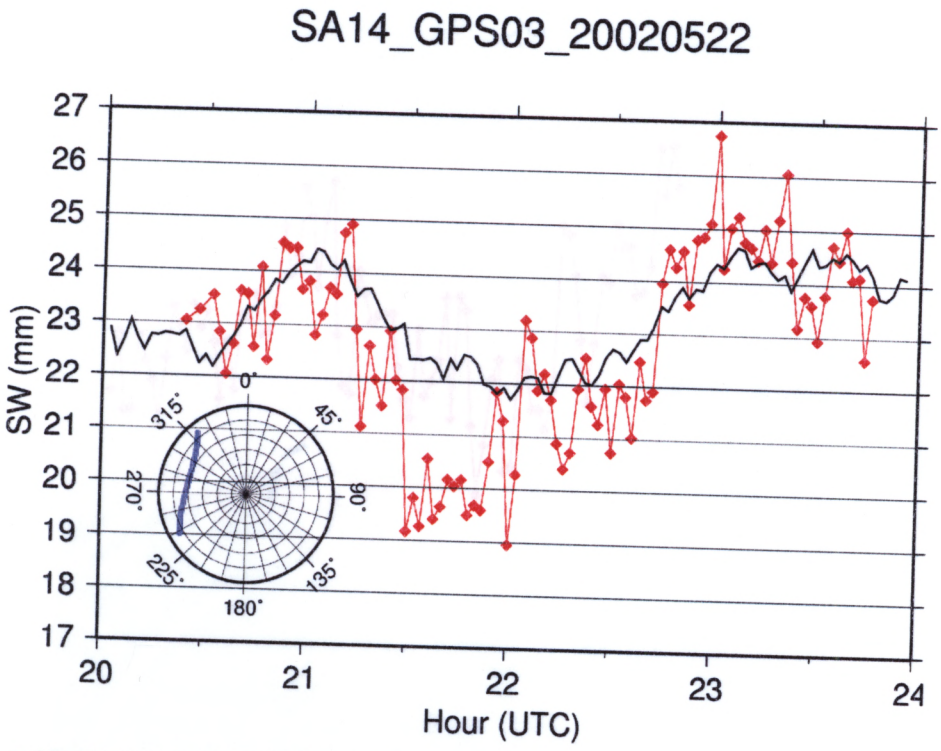

Figure 39: Zenith scaled SW from station SA14 to satellite 3 is shown in red. The average of all zenith scaled SW is plotted in black. The satellite azimuth and elevation is plotted in the small sky plot in the lower left corner.

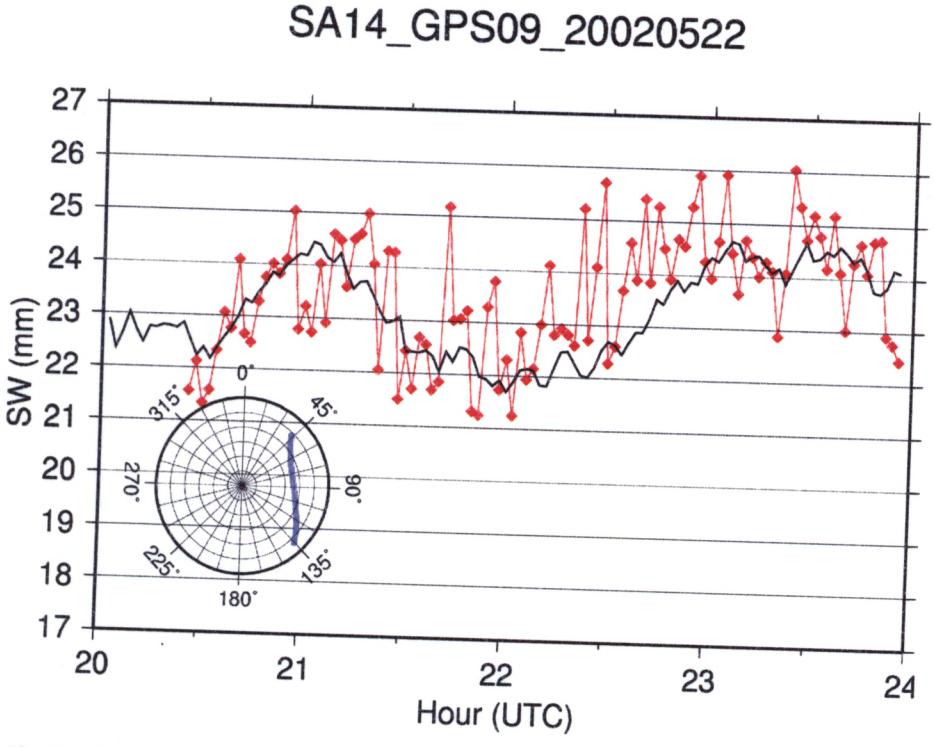

Figure 40: Zenith scaled SW from station SA14 to satellite 9. The data in the plot are represented in the same manner as Figure 39.

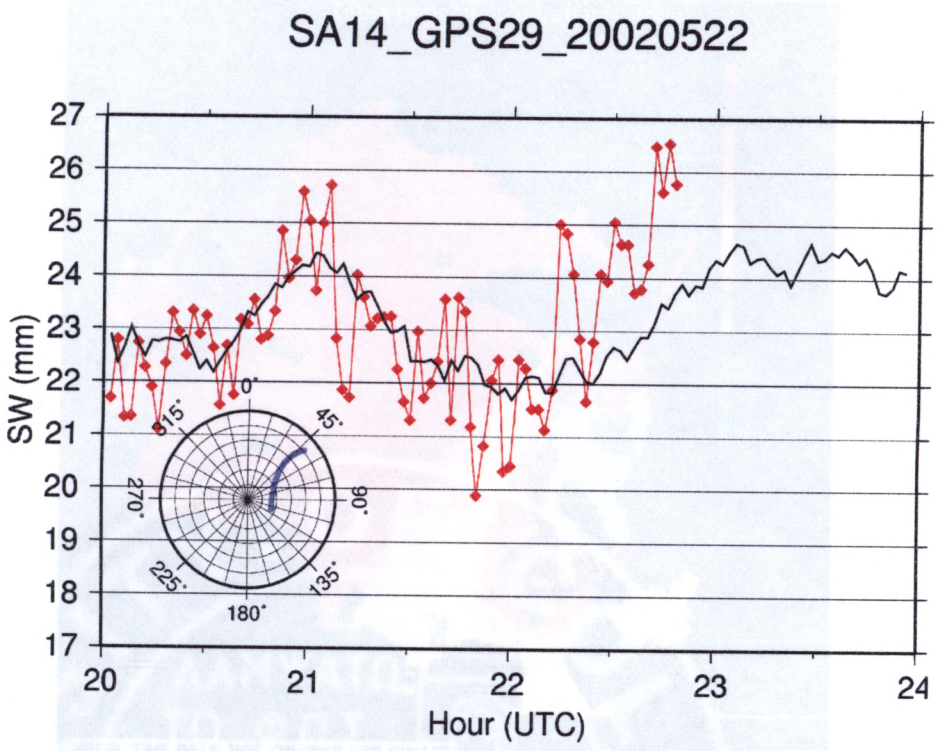

Figure 41: Zenith scaled SW from station SA14 to satellite 29. The data in the plot are represented in the same manner as Figure 39.

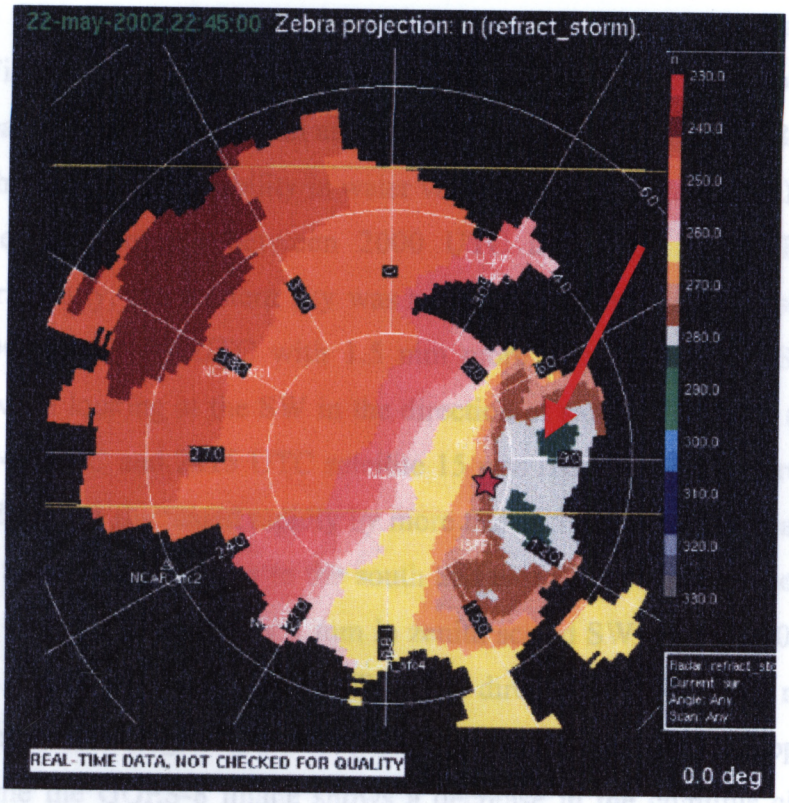

Figure 42: S-Pol surface refractivity field at 2245 UTC (5:45 CST) on May 22, 2002. The location of the GPS station is shown as the red star. As satellite 29 set, it passed through the moist cell identified with the red arrow.

7.3.2 May 30, 2002

The atmospheric conditions on May 30, 2002 were generally quite stable. During the afternoon, the dryline formed and generated a series of small cumulus clouds to the south and east of the boundary. The 1 km resolution GOES-8 imagery at 1908 UTC (2:08 pm local time) is shown in Figure 43 and at 2233 UTC (5:33 pm local time) in Figure 44. At 1900 UTC the Oklahoma mesonet recorded a difference in dew point temperature of more than 15° C (45°-60° C). This difference increased slightly to 17° C (37°-54° C) by 2200 UTC, while the overall dew point dipped from 60° C to 54° C and from 45° C to 37° C. Small cumulus clouds began to form to the south and east of the station around 2000 UTC. The GSFC Raman Lidar showed a deepening of the boundary layer beginning around 1800 UTC (Figure 45). It then recorded sharp changes in mixing ratio between 1945 and 2100 UTC. Shortly after 2100 UTC the Lidar recorded a sudden drying of the boundary layer.

The GPS PW (red diamonds) and zenith scaled SW (blue diamonds) are plotted in Figure 46. As can be seen from the GPS results, the total amount of water vapor decreases from about 26 mm at 1600 UTC to around 22 mm at 1800 UTC. At this point, the azimuthal variability in water vapor increases. Satellite PRN 03 moved through the western sky between 2000 UTC and 2300 UTC (Figure 47). Uncharacteristically, the western sky was relatively wetter than the rest of the sky between 2000 and 2030 UTC with 1.5 mm more of zenith scaled SW. This is confirmed when looking at the SW in the direction of satellite PRN 15 (Figure 48). Between 1945 UTC and 2015 UTC satellite 15 was rising from the northwest. The SW in this direction fluctuated rapidly by more than 2.5 mm in zenith scaled SW. At 2030 UTC, the moisture moves to the south and east of the station. The SW in the direction of PRN 15 increases by 1 mm in zenith scaled SW around 2100 and 2130 UTC. At 2210 UTC the zenith scaled SW in the direction of PRN 15 is more than 3 mm larger than the average SW to all satellites. This increase occurs at approximately the same time the GOES-8 image shows a decrease in the cumulus clouds. This indicates a phase transformation of condensed water into vapor. The equivalent potential temperature profile measured by the Atmospheric Emitted Radiance Interferometer (AERI) [*Feltz and Mecikalski*, 2002] instrument generally warmed throughout the afternoon supporting the concept that the temperature profile of the atmosphere would not support the formation of larger clouds.

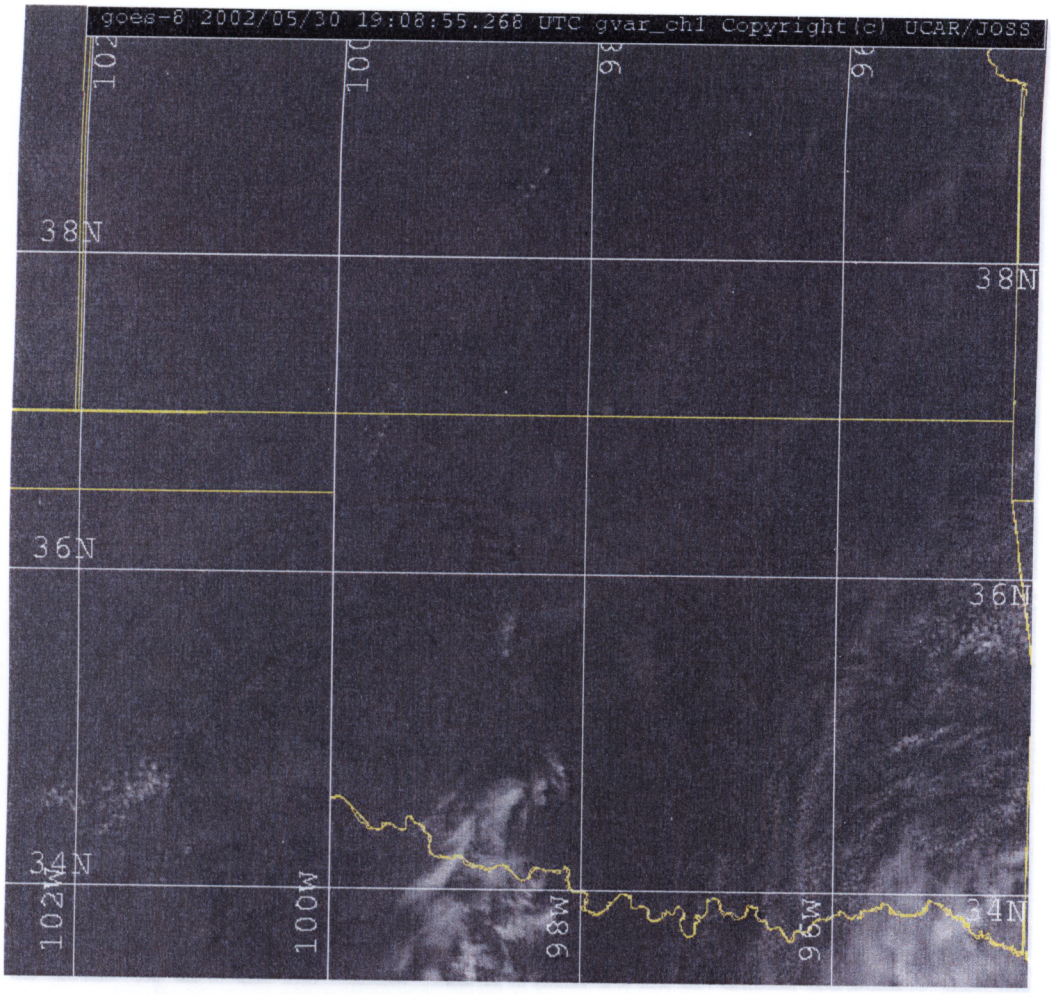

Figure 43: GOES-8 visible imagery at 1 km resolution on 30/May/2002 at 1908 UTC.

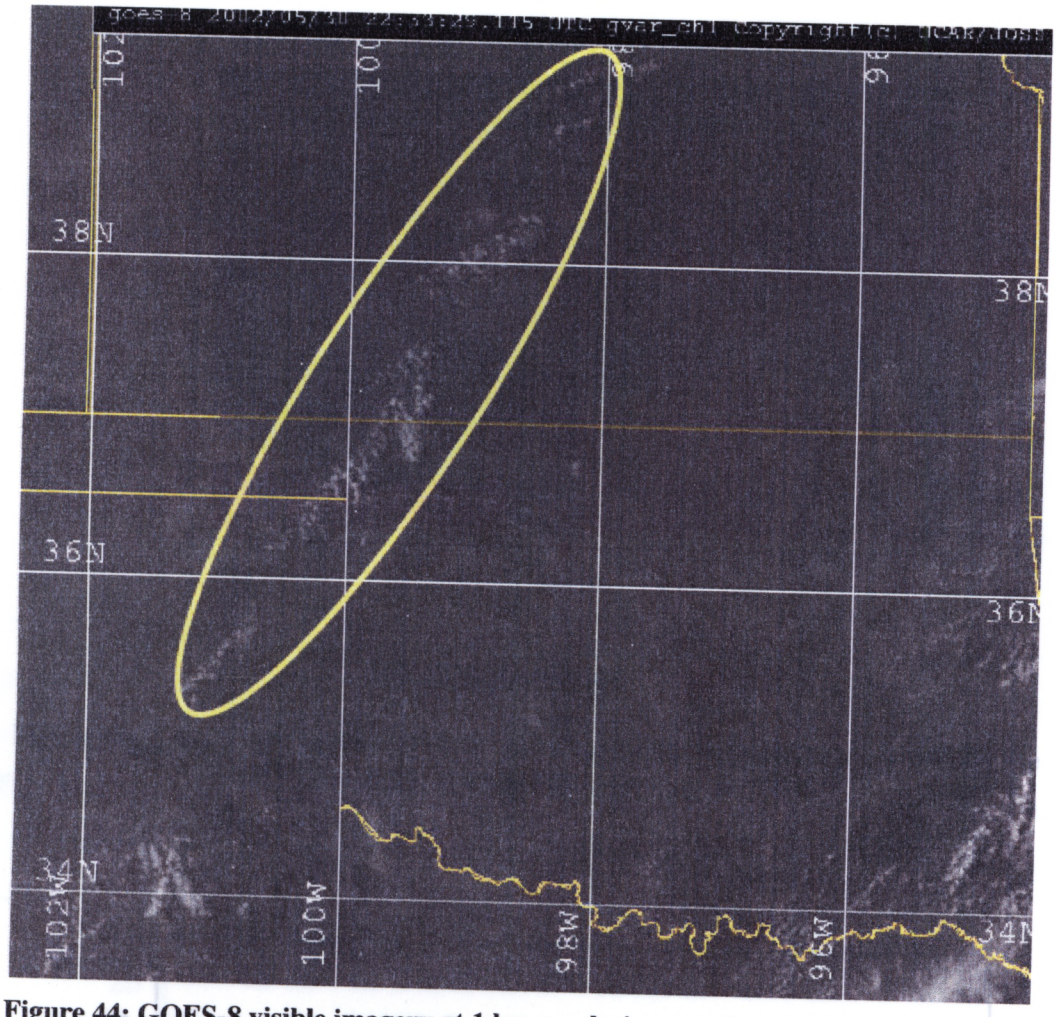

Figure 44: GOES-8 visible imagery at 1 km resolution on 30/May/2002 at 2233 UTC. Small cumulus clouds had formed along the dryline running southwest to northeast through the Oklahoma panhandle.

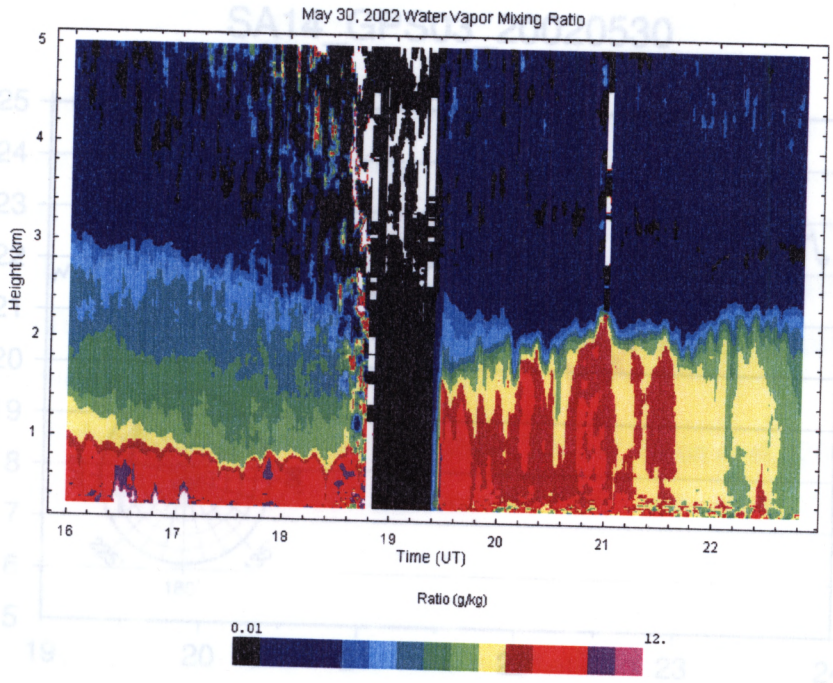

Figure 45: Time-height cross section of water vapor mixing ratio as measured by the GSFC scanning Raman Lidar on May 30, 2002.

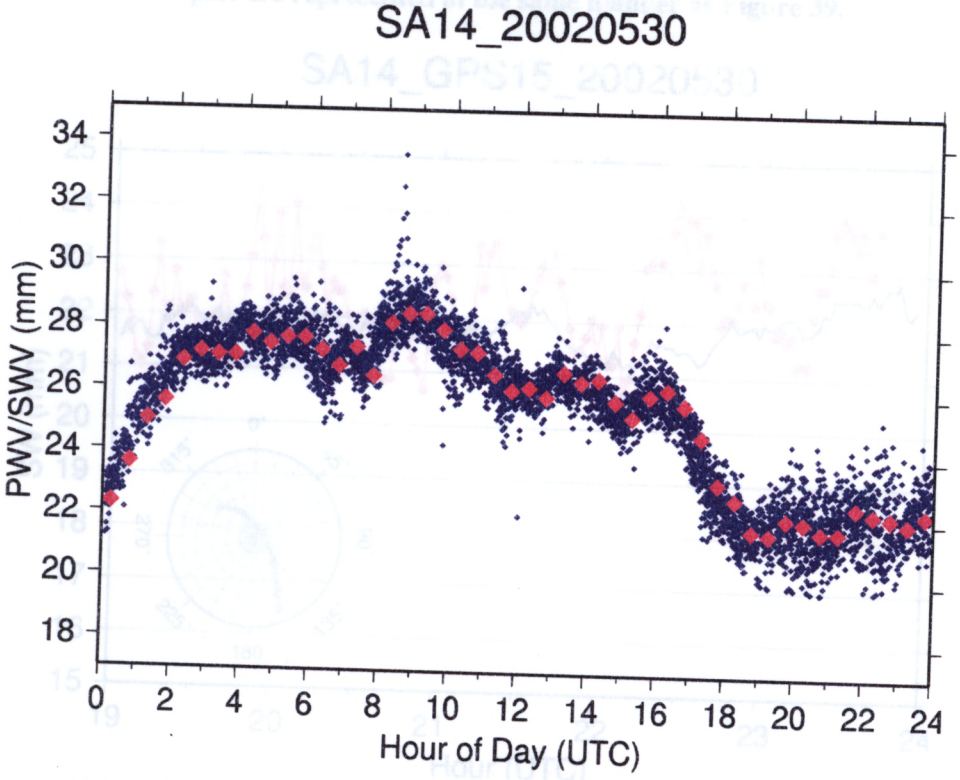

Figure 46: GPS PW (red diamonds) and zenith scaled SW (blue diamonds) at the SA14 station located in the panhandle of Oklahoma.

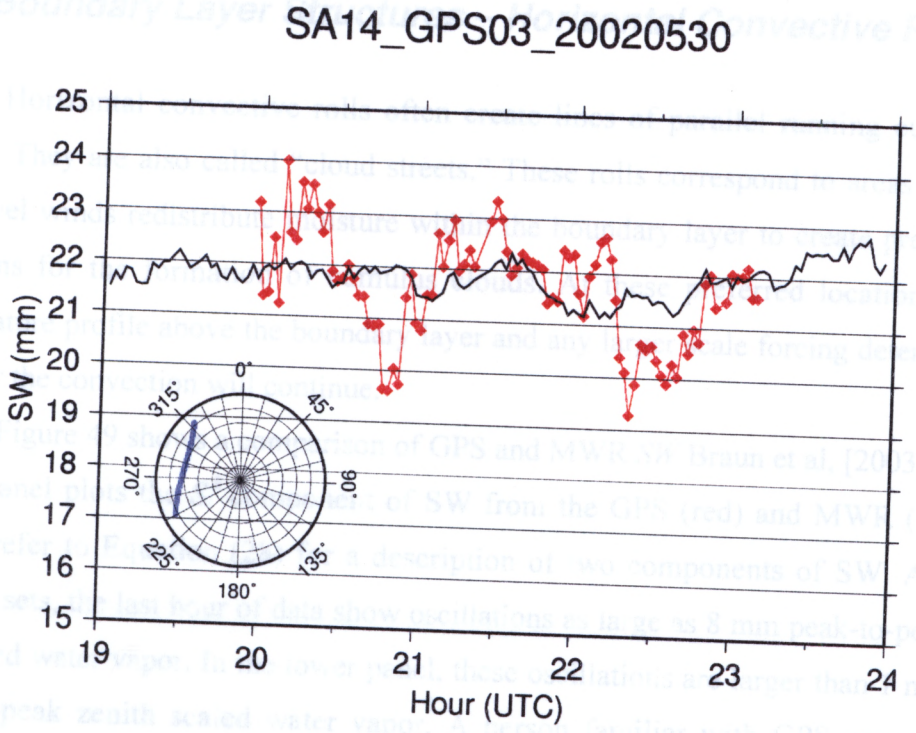

Figure 47: Zenith scaled SW from station SA14 to satellite 3 on May 30, 2002. The data in the plot are represented in the same manner as Figure 39.

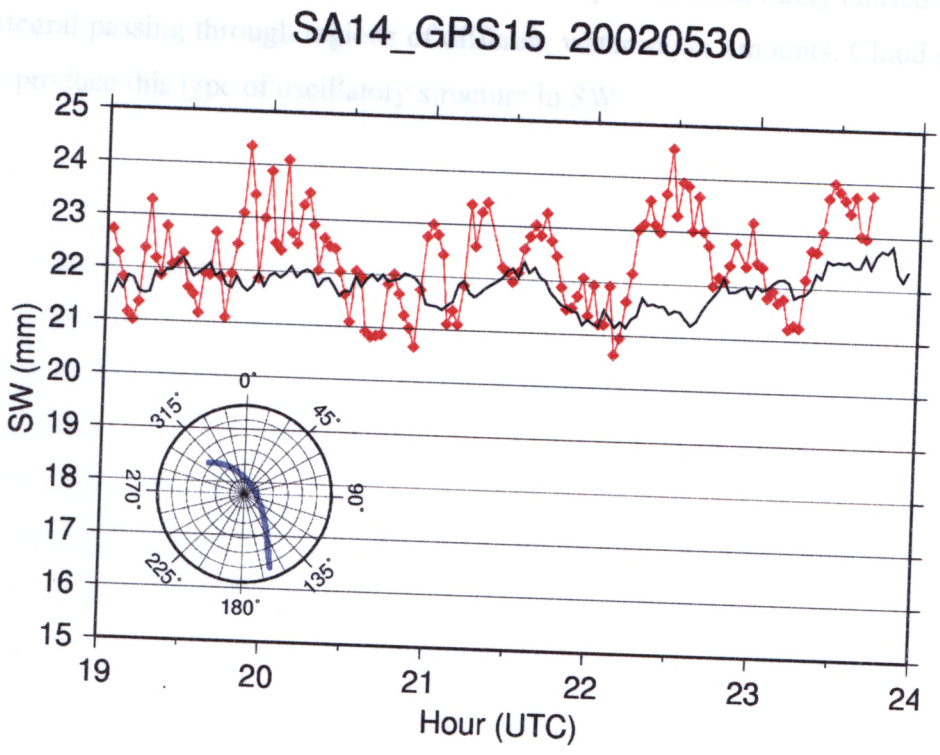

Figure 48: Zenith scaled SW from station SA14 to satellite 15. The data in the plot are represented in the same manner as Figure 39.

7.4 Boundary Layer Structures – Horizontal Convective Rolls

Horizontal convective rolls often create lines of parallel running cumulus clouds. They are also called "cloud streets." These rolls correspond to areas where low-level winds redistribute moisture within the boundary layer to create preferred locations for the formation of cumulus clouds. At these preferred locations, the temperature profile above the boundary layer and any larger scale forcing determines whether the convection will continue.

Figure 49 shows a comparison of GPS and MWR *SW* Braun et al, [2003]. The upper panel plots the S_i^k component of SW from the GPS (red) and MWR (blue). Please refer to Equation (28) for a description of two components of SW. As the satellite sets, the last hour of data show oscillations as large as 8 mm peak-to-peak in integrated water vapor. In the lower panel, these oscillations are larger than 1 mm in peak-to-peak zenith scaled water vapor. A person familiar with GPS processing techniques would generally attribute these oscillations to ground reflected multipath, but the agreement with the MWR confirms that they were most likely caused by the SW integral passing through regions of different water vapor amounts. Cloud streets should produce this type of oscillatory structure in SW.

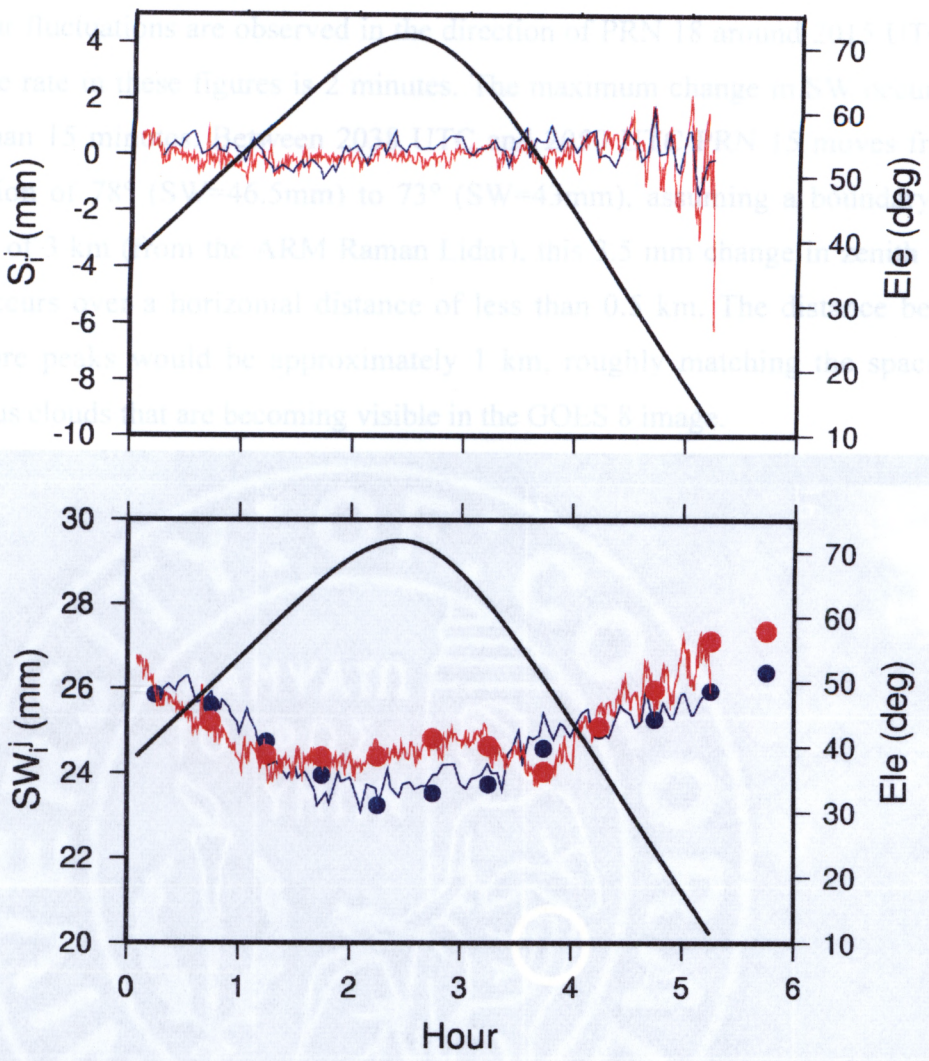

Figure 49: Comparisons of GPS (red) and MWR (blue) from Braun et al 2003 paper. The top panel plots the S_i^k component of SW, the lower panel plots zenith scaled SW.

Convective rolls were observed with 1 km resolution GOES-8 visible imagery on June 9, 2002 (Figure 50). Small cumulus clouds began forming over station SG01 between 2000 UTC and 2100 UTC. The Oklahoma mesonet recorded strong southerly winds between 10 and 20 mph throughout the state (Figure 51), conditions that are generally favorable for the formation of rolls. Zenith scaled SW (Figure 52) varied by more than 4 mm, with an average of approximately 44 mm, throughout the afternoon (1600 to 2400 UTC). Rapid changes of SW in the direction of individual satellites were measured between 2000 UTC and 2200 UTC. Zenith scaled SW in the direction of two satellites are shown in Figure 53 and Figure 54. Peak-to-peak changes as large as 3.5 mm are seen in the direction of PRN 15 around 2045 UTC.

Similar fluctuations are observed in the direction of PRN 18 around 2015 UTC. The sample rate in these figures is 2 minutes. The maximum change in SW occurs over less than 15 minutes. Between 2038 UTC and 2050 UTC PRN 15 moves from an elevation of 78° (SW=46.5mm) to 73° (SW=43mm), assuming a boundary layer height of 3 km (from the ARM Raman Lidar), this 3.5 mm change in zenith scaled SW occurs over a horizontal distance of less than 0.5 km. The distance between moisture peaks would be approximately 1 km, roughly matching the spacing of cumulus clouds that are becoming visible in the GOES 8 image.

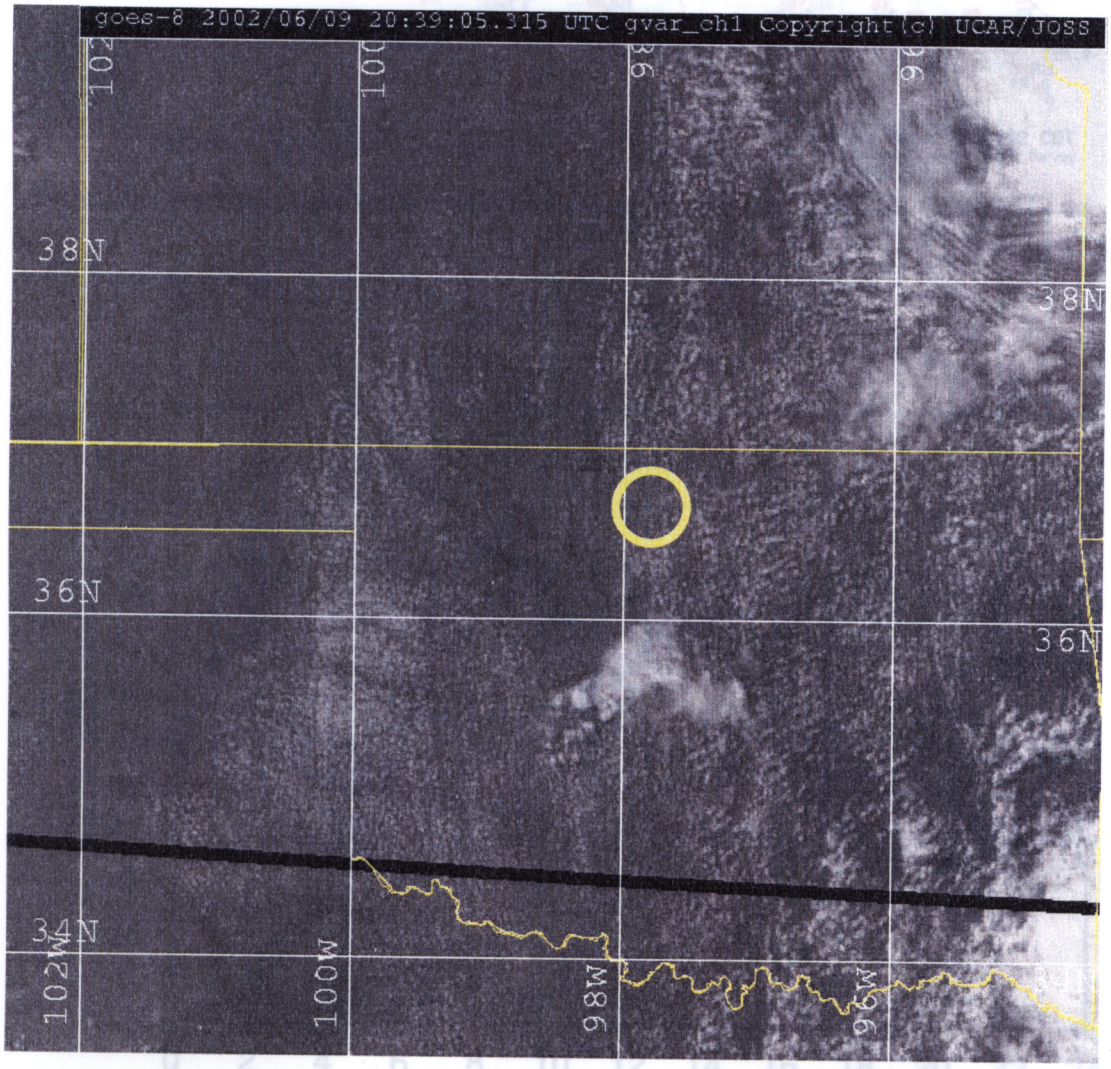

Figure 50: GOES-8 visible imagery at 1 km resolution on June 9, 2002 at 2039 UTC. Horizontal convective rolls exist over large sections of Oklahoma.

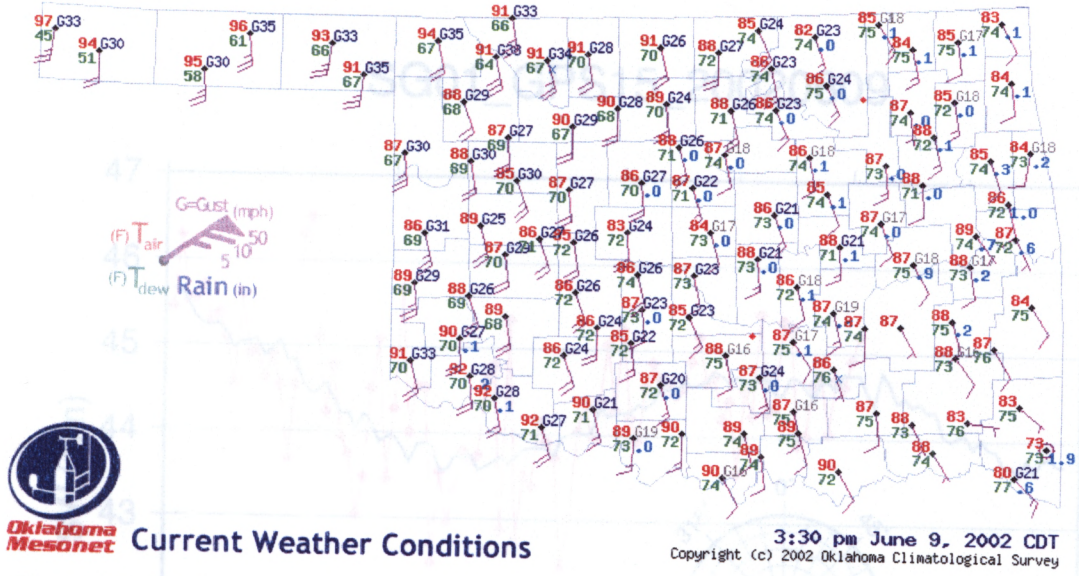

Figure 51: Surface conditions from the Oklahoma Mesonet at 2030 UTC (3:30 CST) on June 9, 2002.

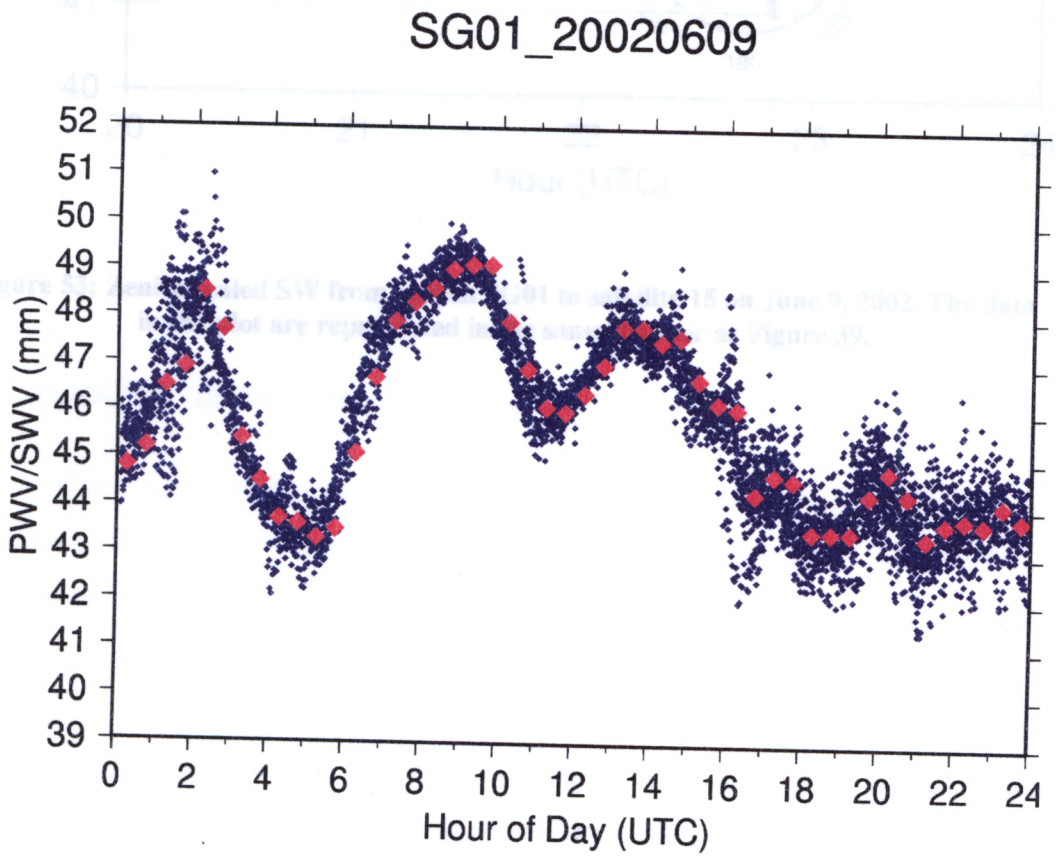

Figure 52: GPS PW (red diamonds) and zenith scaled SW (blue diamonds) station SG01 on June 9, 2002.

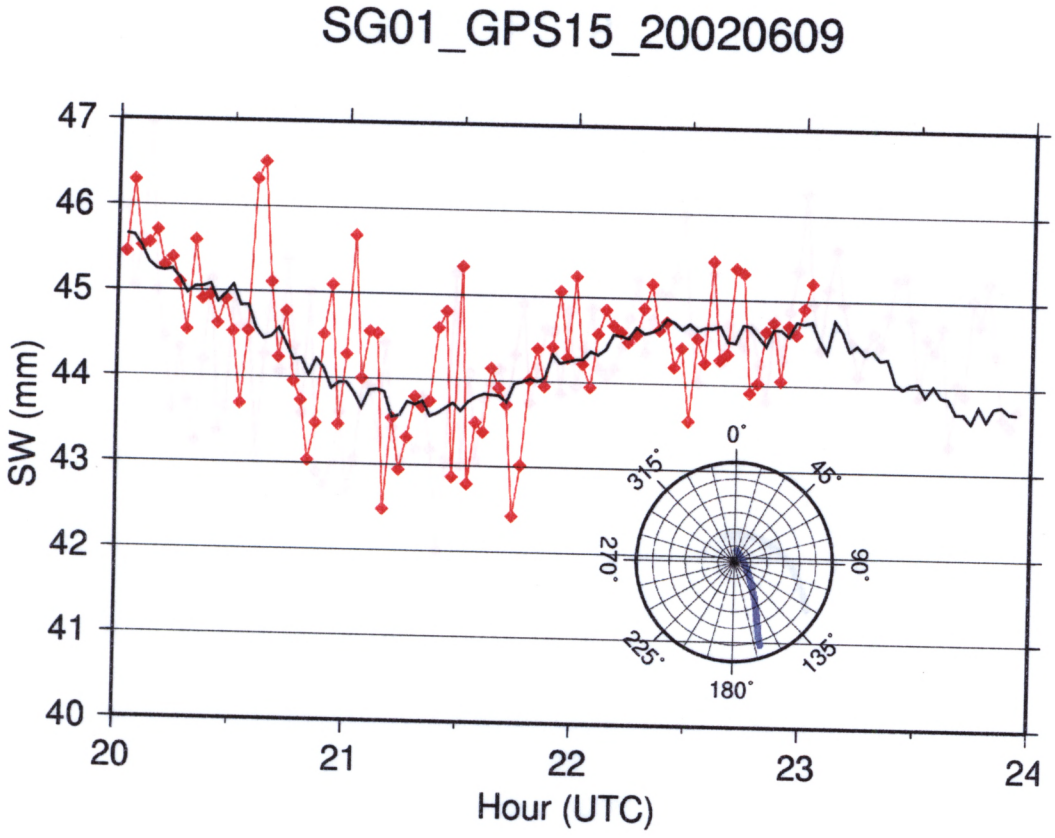

Figure 53: Zenith scaled SW from station SG01 to satellite 15 on June 9, 2002. The data in the plot are represented in the same manner as Figure 39.

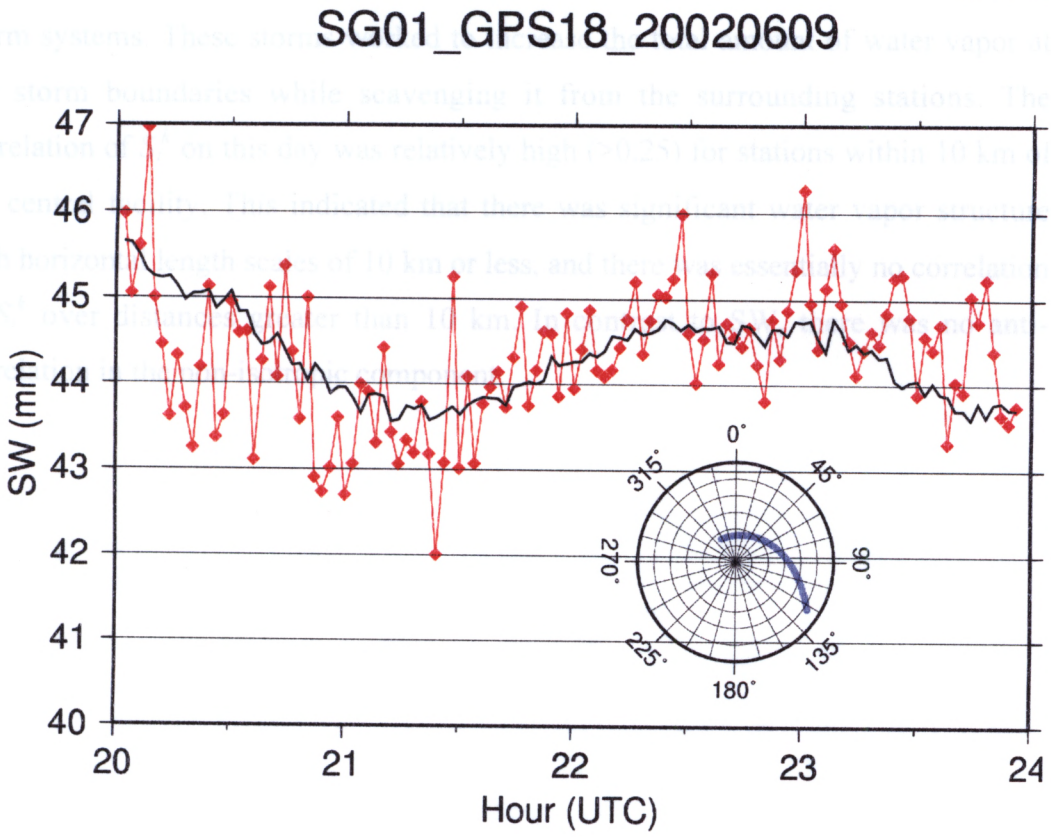

Figure 54: Zenith scaled SW from station SG01 to satellite 18 on June 9, 2002. The data in the plot are represented in the same manner as Figure 39.

7.5 Spatial Correlation of SW and S_i^k

Water vapor is known to be variable over relatively short distances. An analysis of SW during IHOP_2002 is used to quantify "relatively short". Wide differences in the correlations of water vapor from one day to the next were observed. Linear correlations for two days are plotted in Figure 55 (May 23, 2002) and Figure 56 (May 31, 2002). The lower panels plot the linear correlation of SW as a function of station separation. The top panels plot the linear correlation of the non-isotropic component of SW (S_i^k). In these calculations, the GPS station at the ARM central facility was compared against all the other stations in the Central United States.

On May 23, 2002, two significant storm systems moved through the region. For this day, the strength of the SW correlation diminished over distances of less than

100 km. There was significant anti-correlation at distances less than 100 km. This anti-correlation is likely related to moisture fluxes associated with the movement of storm systems. These storms worked to increase the total amount of water vapor at the storm boundaries while scavenging it from the surrounding stations. The correlation of S_i^k on this day was relatively high (>0.25) for stations within 10 km of the central facility. This indicated that there was significant water vapor structure with horizontal length scales of 10 km or less, and there was essentially no correlation of S_i^k over distances greater than 10 km. In contrast to SW, there was no anti-correlation in the non-isotropic component.

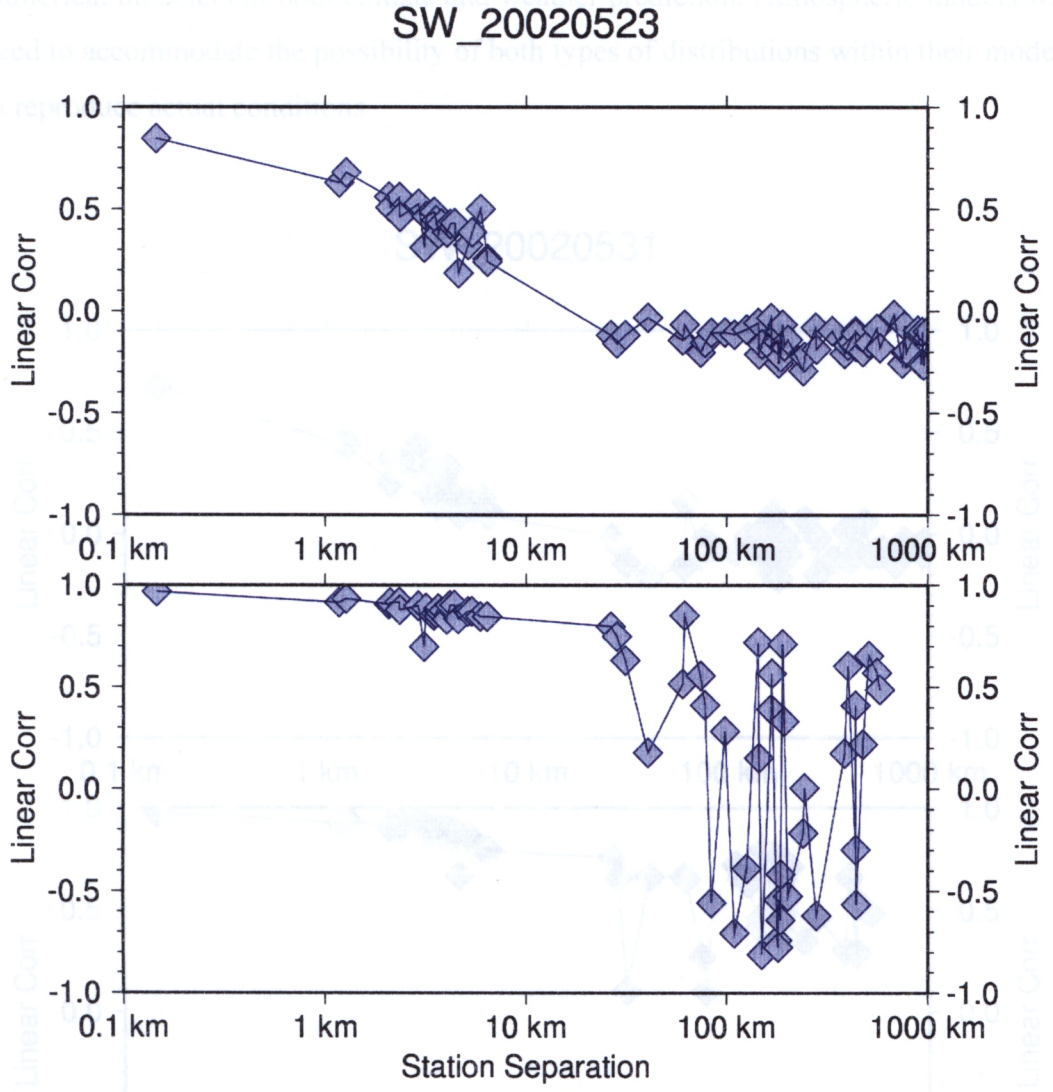

Figure 55: Linear correlation of SW (bottom) and S_i^k (top) as a function of station separation for May 23, 2002.

May 31, 2002, was a relatively calm day in the Southern Great Plains. There was no precipitation, with only small cumulus clouds forming over the southeast portion of Oklahoma in the late afternoon. The correlation of SW was high across all stations (Figure 56). Similar to the May 23 day, the correlation of S_i^k was also relatively high (>0.25) for length scales of less than 10 km. This calm day, and the high correlation across the entire region, is in contrast to May 23 where there was anti-correlation over distances of less than 100 km. The differences in these two days

highlight the large variability in water vapor and represents a significant problem for numerical modelers of both climate and weather prediction. Atmospheric models will need to accommodate the possibility of both types of distributions within their models to reproduce actual conditions.

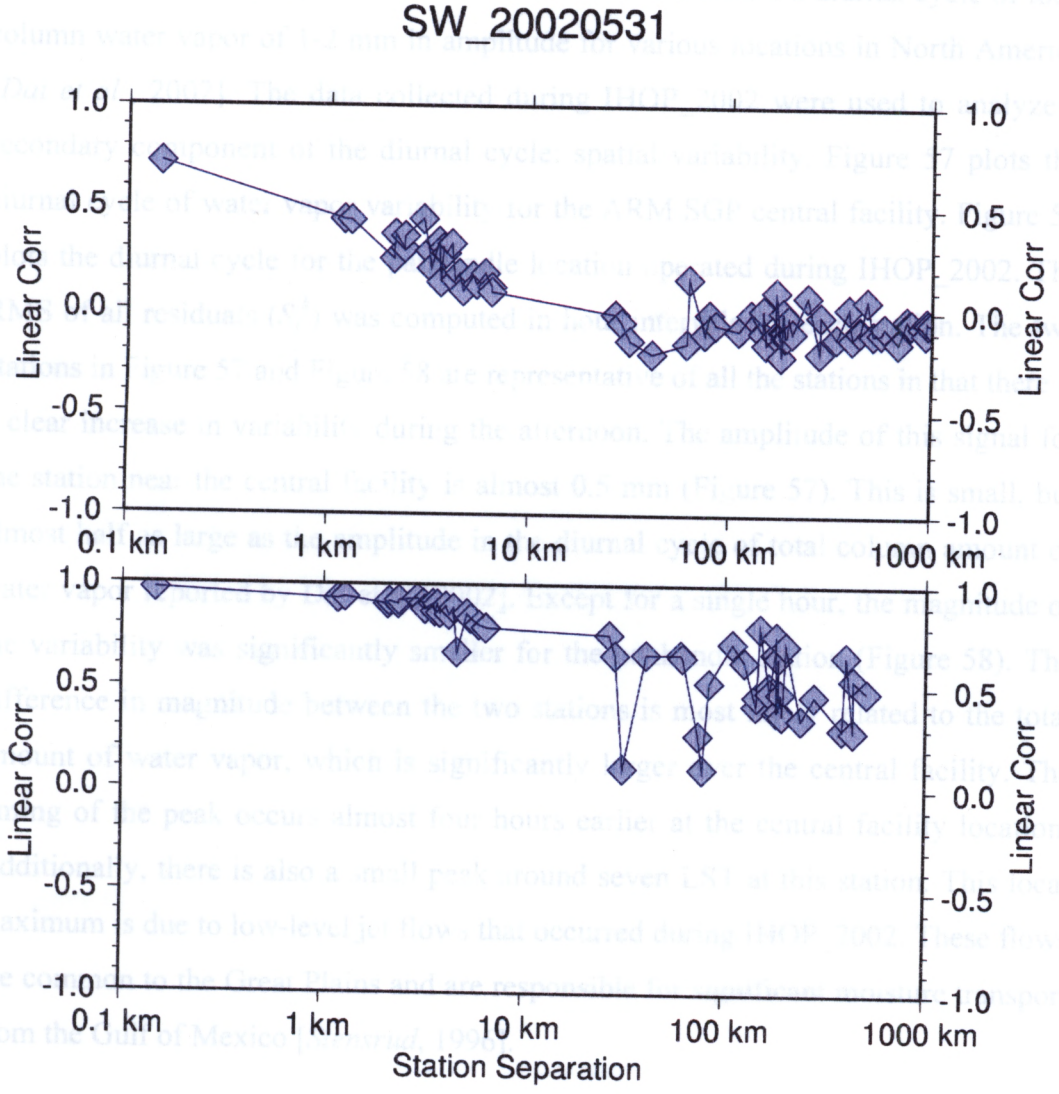

Figure 56: Linear correlation of SW (bottom) and S_i^k (top) as a function of station separation for May 31, 2002.

7.6 Diurnal Evolution of the Boundary Layer

Diurnal cycles in the atmosphere are mainly driven by incident solar radiation, or secondary effects of the daily solar cycle. Water vapor plays a significant role in both short wave (downwelling) and long wave (upwelling) radiation cycles [*Lieberman et al.*, 2002]. GPS PW has been used to measure a diurnal cycle of total column water vapor of 1-2 mm in amplitude for various locations in North America [*Dai et al.*, 2002]. The data collected during IHOP_2002 were used to analyze a secondary component of the diurnal cycle: spatial variability. Figure 57 plots the diurnal cycle of water vapor variability for the ARM SGP central facility. Figure 58 plots the diurnal cycle for the panhandle location operated during IHOP_2002. The RMS of all residuals (S_i^k) was computed in hour intervals for each station. The two stations in Figure 57 and Figure 58 are representative of all the stations in that there is a clear increase in variability during the afternoon. The amplitude of this signal for the station near the central facility is almost 0.5 mm (Figure 57). This is small, but almost half as large as the amplitude in the diurnal cycle of total column amount of water vapor reported by Dai et al [2002]. Except for a single hour, the magnitude of the variability was significantly smaller for the panhandle station (Figure 58). The difference in magnitude between the two stations is most likely related to the total amount of water vapor, which is significantly larger over the central facility. The timing of the peak occurs almost four hours earlier at the central facility location. Additionally, there is also a small peak around seven LST at this station. This local maximum is due to low-level jet flows that occurred during IHOP_2002. These flows are common to the Great Plains and are responsible for significant moisture transport from the Gulf of Mexico [*Stensrud*, 1996].

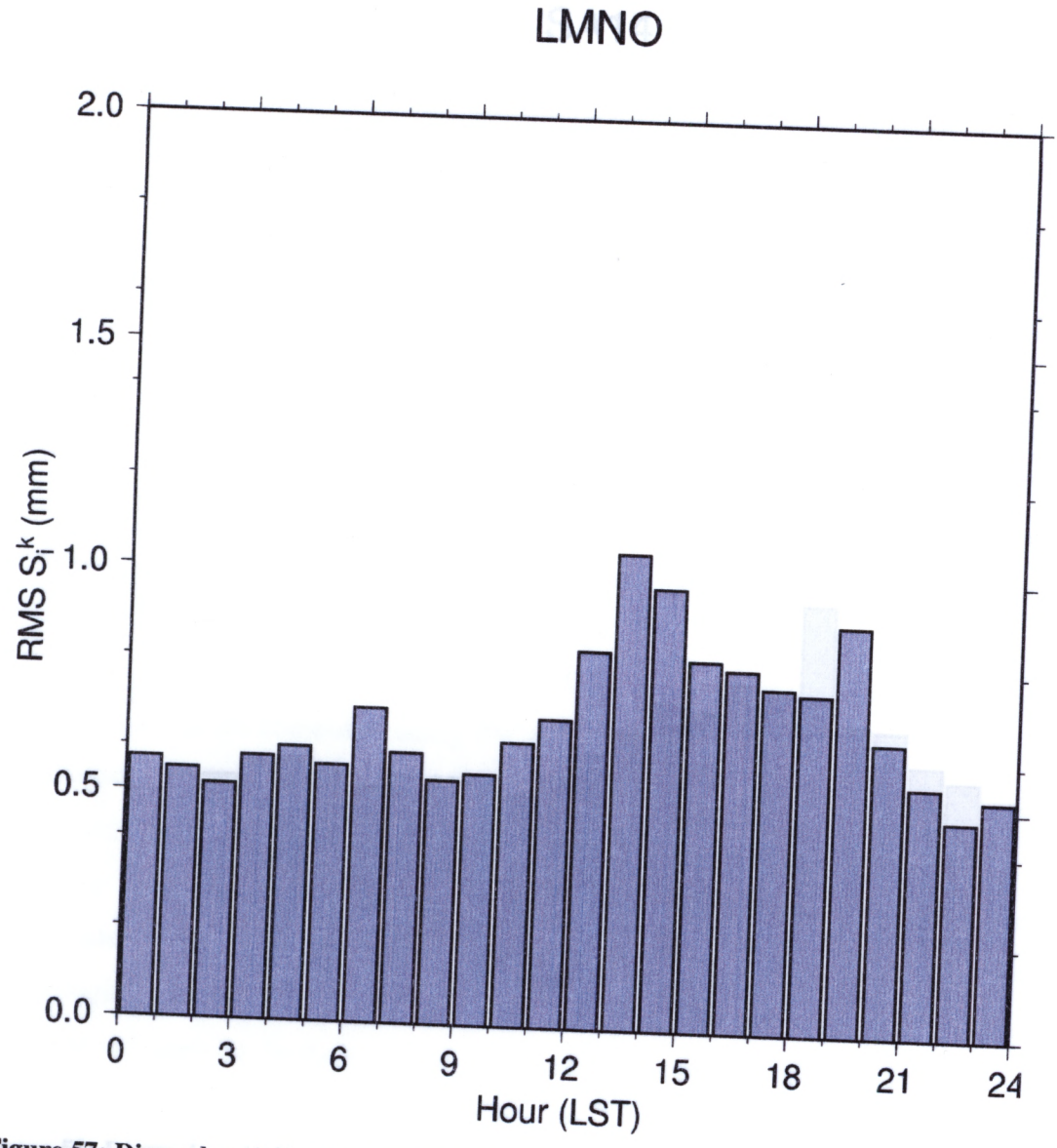

Figure 57: Diurnal variation in the non-isotropic component of SW (S_i^k) for Lamont, OK during the IHOP_2002 campaign.

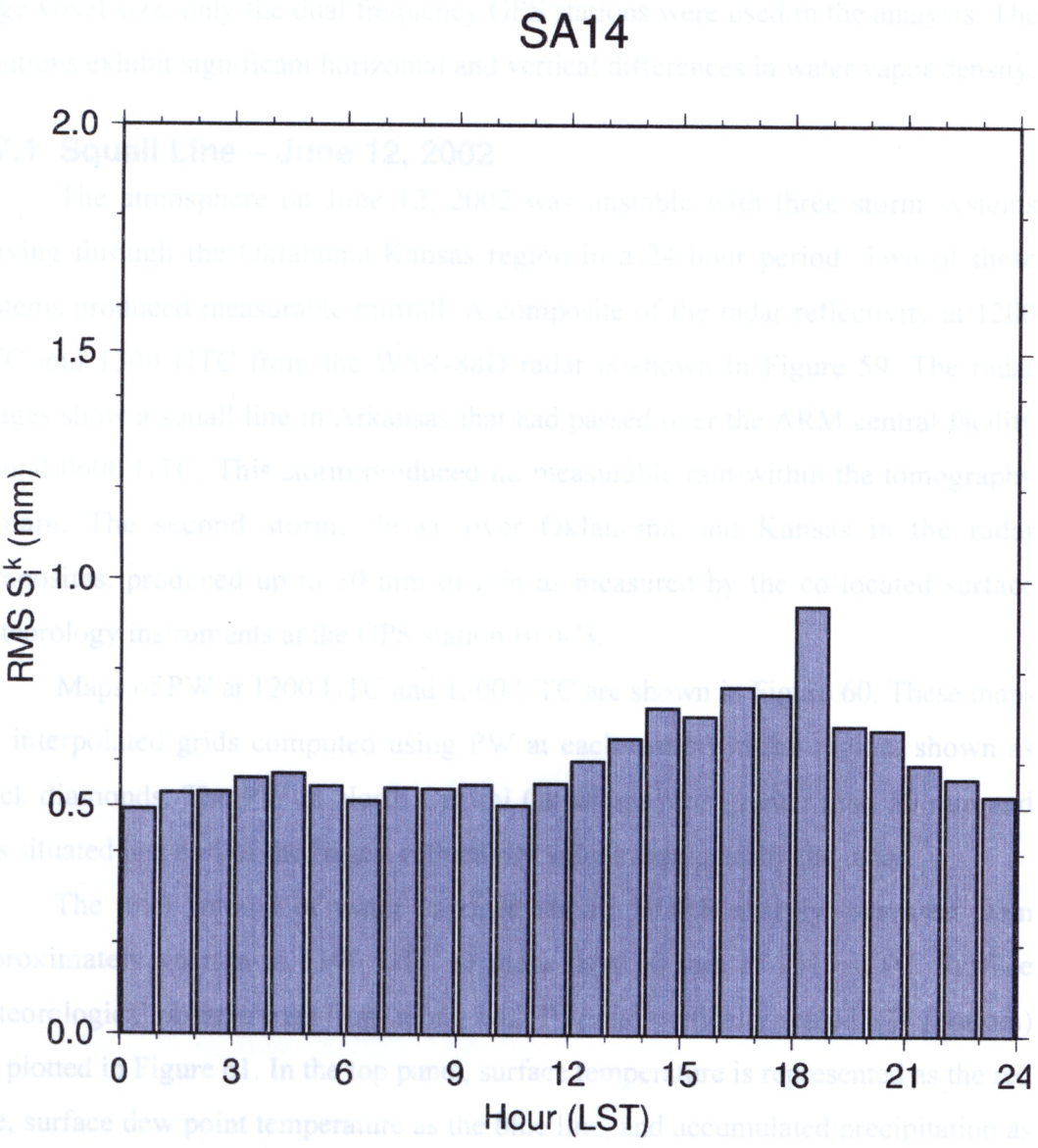

Figure 58: Diurnal variation in the non-isotropic component of SW (S_i^k) for Oklahoma Panhandle station SA14 during IHOP_2002.

7.7 Tomography Solutions

The operation of seven additional GPS stations around the ARM central facility by Joel Van Baelen and CNRS France provided the opportunity to compute tomographic fields over a domain larger than the 40 km^2 sampled with the single frequency network. During IHOP_2002, the region was expanded to a 100 km x 180 km domain, centered on the ARM central facility. The vertical depth of each voxel was 1 km and the horizontal dimension was approximately 20 km x 20 km. With this

large voxel size, only the dual frequency GPS stations were used in the analysis. The solutions exhibit significant horizontal and vertical differences in water vapor density.

7.7.1 Squall Line – June 12, 2002

The atmosphere on June 12, 2002 was unstable with three storm systems moving through the Oklahoma-Kansas region in a 24-hour period. Two of these systems produced measurable rainfall. A composite of the radar reflectivity at 1200 UTC and 1300 UTC from the WSR-88D radar is shown in Figure 59. The radar images show a squall line in Arkansas that had passed over the ARM central facility around 0600 UTC. This storm produced no measurable rain within the tomography domain. The second storm, shown over Oklahoma and Kansas in the radar composites, produced up to 30 mm of rain as measured by the co-located surface meteorology instruments at the GPS station BURB.

Maps of PW at 1200 UTC and 1300 UTC are shown in Figure 60. These maps are interpolated grids computed using PW at each station in the region, shown as black diamonds. The PW in North Central Oklahoma was greater than 50 mm and was situated just east of the largest reflectivity values measured by the radar.

The total amount of water vapor at station BURB sharply increased from approximately 46 mm at 1100 UTC to more than 60 mm at 1315 UTC. Surface meteorological observations (top) along with PW and vertically scaled SW (bottom) are plotted in Figure 61. In the top panel, surface temperature is represented as the red line, surface dew point temperature as the blue line, and accumulated precipitation as the black line. The wind speed is given by the vectors near the top of the panel; wind speed is represented by the length of the vector, and the orientation describes the wind direction. A vector pointing up implies winds moving south to north. The PW and vertically scaled SW increased by almost 20 mm in just over two hours. The maximum amount of vapor peaks just before the onset of rain.

Figure 62 plots the surface observations from station BURB in the top panel and the vertical profile of water vapor density, retrieved from the tomography, in the bottom panel. The profile represents the water vapor density from the voxels above the station, computed at 15-minute increments. Radiosondes were used in these tomography solutions. Station BURB is located approximately 60 km east of the

radiosonde launch site. The balloon launch times are indicated by the vertical dashed lines in the density profile. There is a significant change in the profile between the radiosonde launches at 1130 UTC and 1430 UTC. At 1130 UTC, the lowest level of the profile contained more that 15 g/m^3 of water vapor. The profile was significantly drier through the next 2 km of the boundary layer. Around 1200 UTC, an increase in temperature and dew point temperature indicated that the weak surface winds (less than 3 m/sec) from the south were transporting warm moist air above the station. By 1230 UTC this air had been vertically lifted in front of the rain band and transported up into the boundary layer below 2 km. This moisture extended to an altitude of 4 km by 1300 UTC, almost 30 minutes before rain began falling at the station. The rain associated with this storm system fell quite rapidly. Almost all of the 30 mm fell within 30-minutes. During the rainfall, the tomography profile dried within the lowest 2 km while a significant amount of moisture (nearly 5 g/m^3) remained in the atmosphere between 3 and 4 km.

Station BURB recorded the largest rainfall within the tomography region. An analysis of the solutions across the domain indicates that the vertical transport of moisture at BURB was significantly greater than at other stations. Perhaps the increased moisture that passed into the free troposphere allowed for stronger convection and rain to fall at this station. A third storm passed over the network around 0200 UTC on June 13, 2002. This storm produced more than 60 mm of rain at station BURB. The tomography solutions for June 13 were not initialized with a radiosonde until after the storm had passed, but the elevated moisture near the end of the day on June 12 most likely played a significant roll in this large rainfall. This would agree with simulations indicating that increased moisture above a boundary layer intensifies rain associated with convection [*Park and Droegemeier*, 1999; *Park and Droegemeier*, 2000].

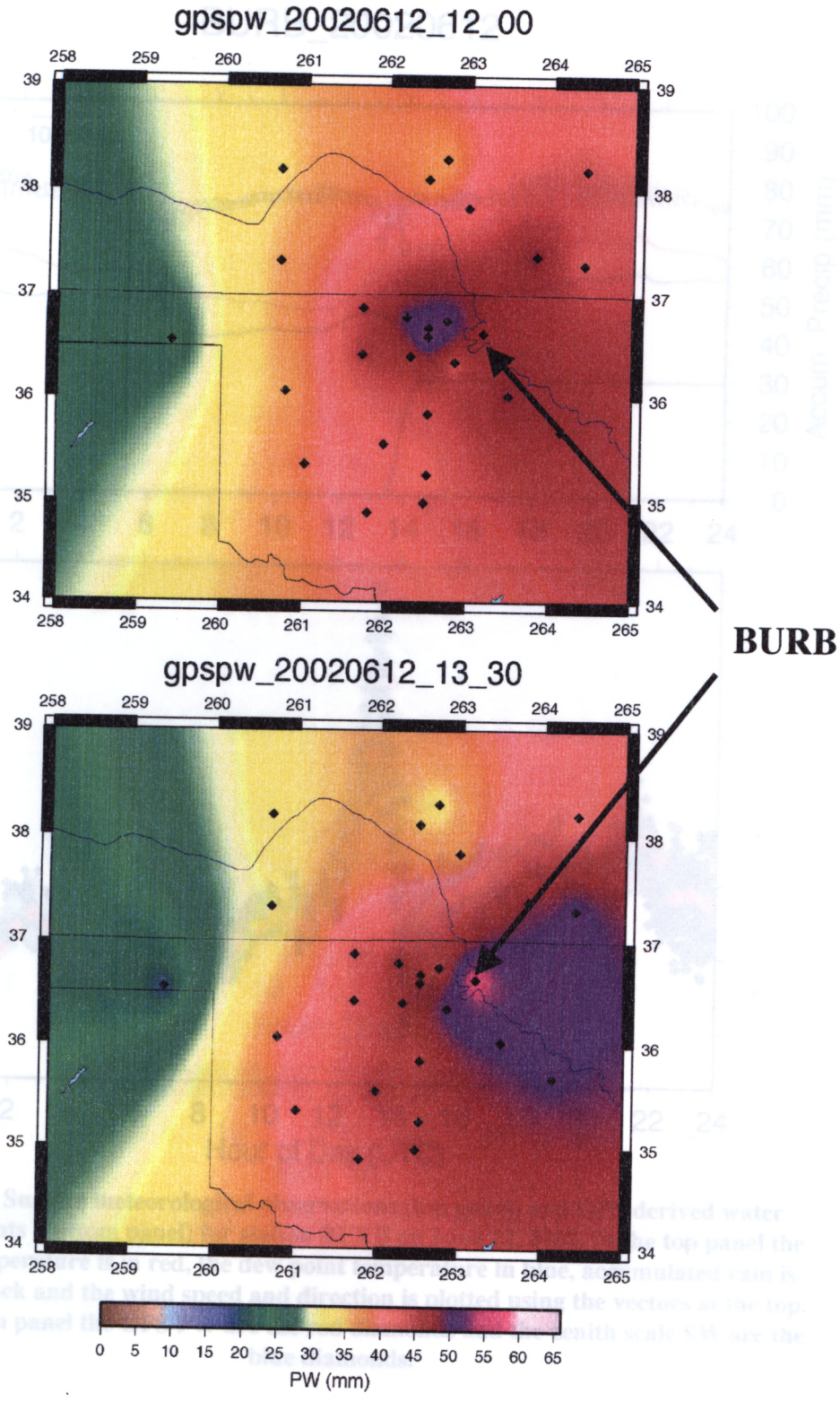

Figure 60: Interpolated maps of 30-minute PW estimates on June 12, 2002 beginning at 1200 UTC (top) and 1330 UTC (bottom). The stations used in the interpolation are shown as diamonds.

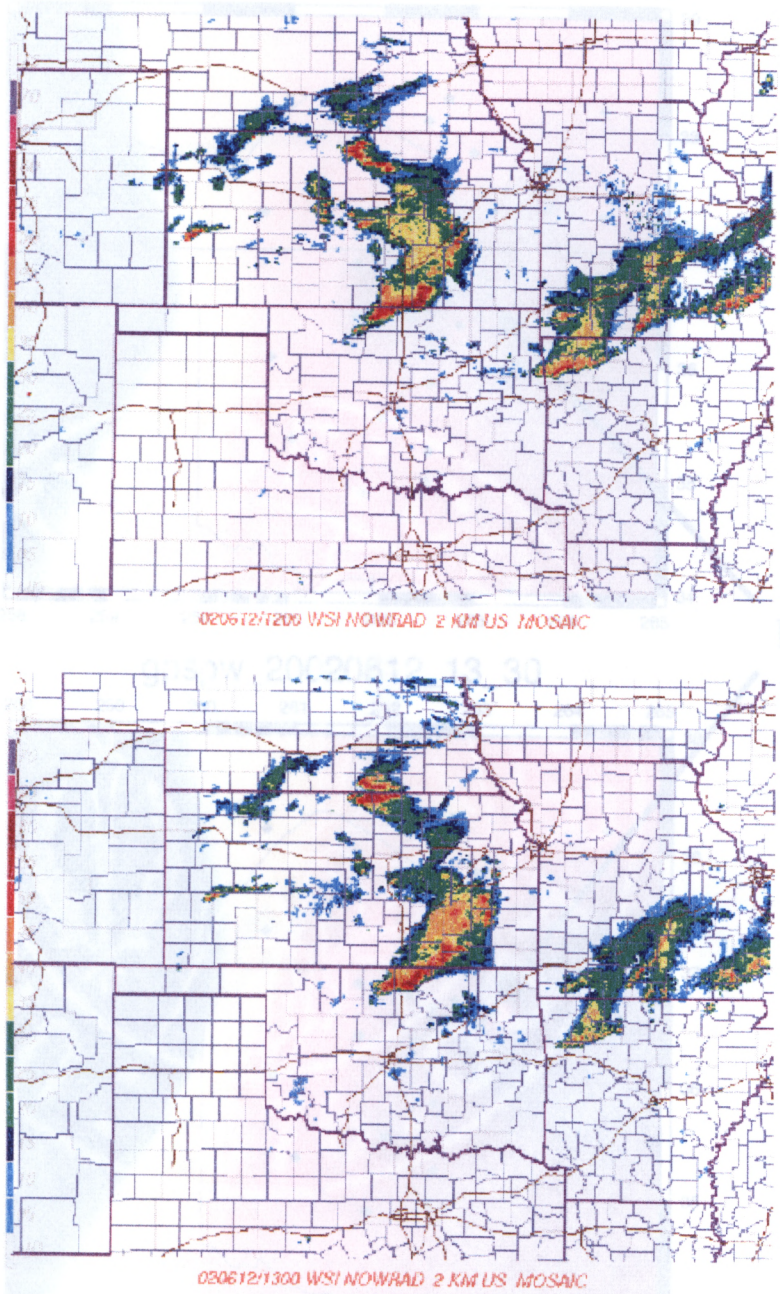

Figure 59: Composite WSR-88D radar reflectivity on June 12, 2002 at 1200 UTC (top) and 1300 UTC (bottom).

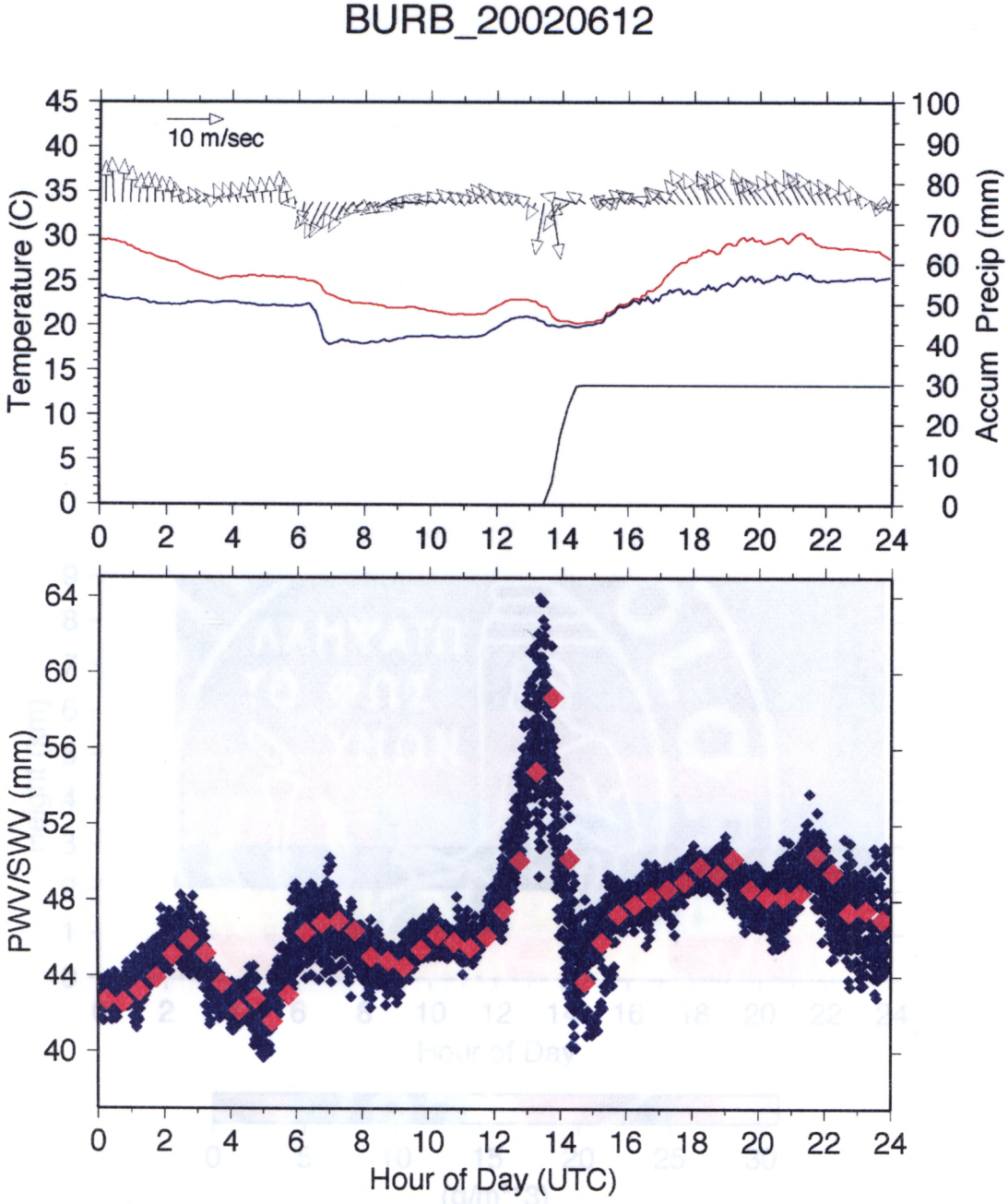

Figure 61: Surface meteorological observations (top panel) and GPS derived water vapor amounts (bottom panel) for station BURB on June 12, 2002. In the top panel the surface temperature is in red, the dew point temperature in blue, accumulated rain is plotted in black and the wind speed and direction is plotted using the vectors at the top. In the bottom panel the GPS PW are the red diamonds and the zenith scale SW are the blue diamonds.

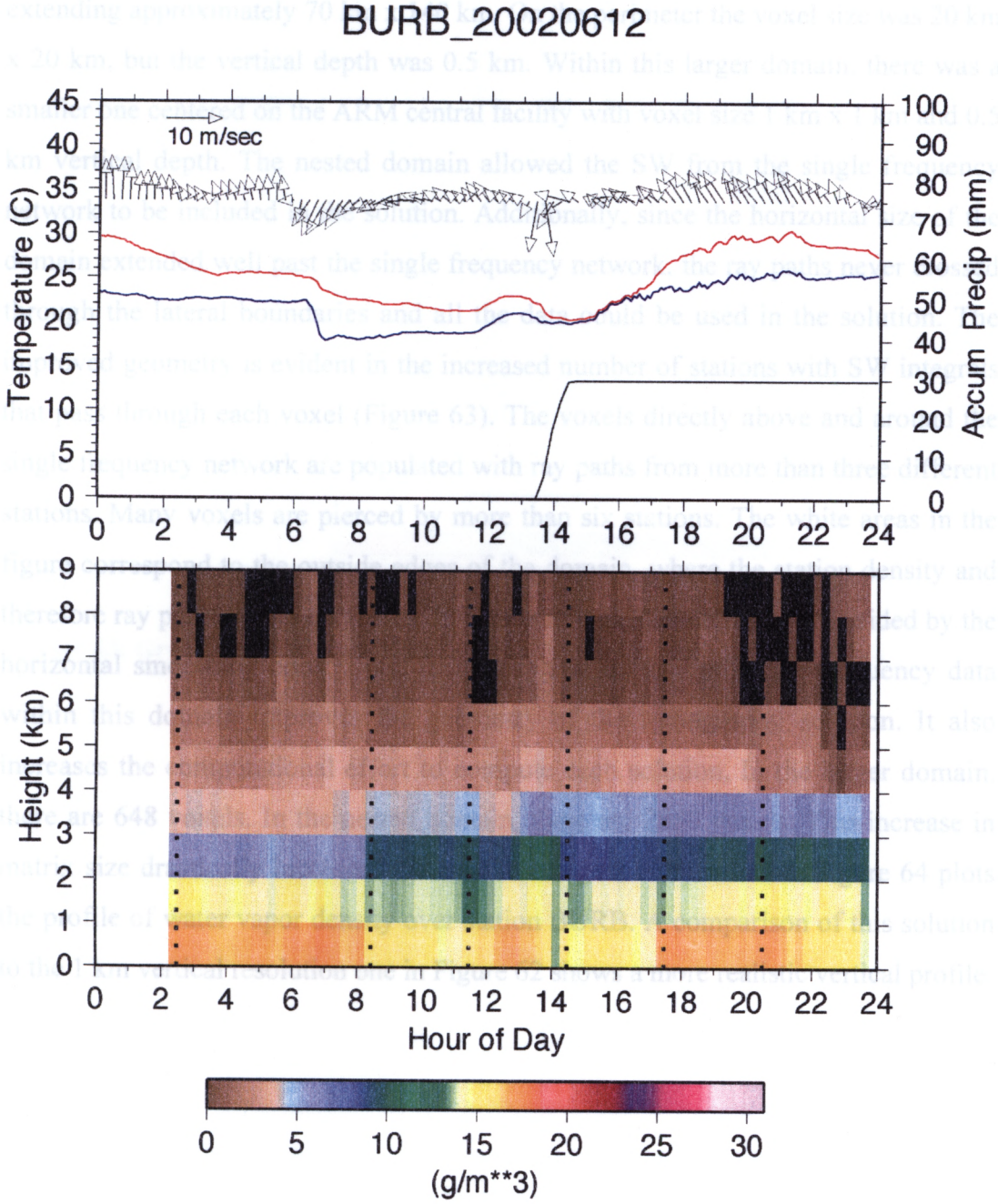

Figure 62: Surface meteorological observations (top) and time-height profile of water vapor density (bottom) for station BURB on June 12, 2002.

7.7.2 Nested Tomography – June 12, 2002

In addition to the relatively large horizontal extent of the domain computed using only the dual frequency GPS stations, a nested domain was configured that combined SW retrieved from both the dual and single frequency stations. The extent of this nested region was somewhat smaller than the dual frequency domain,

extending approximately 70 km x 140 km. On the perimeter the voxel size was 20 km x 20 km, but the vertical depth was 0.5 km. Within this larger domain, there was a smaller one centered on the ARM central facility with voxel size 1 km x 1 km and 0.5 km vertical depth. The nested domain allowed the SW from the single frequency network to be included in the solution. Additionally, since the horizontal size of the domain extended well past the single frequency network, the ray paths never crossed through the lateral boundaries and all the data could be used in the solution. The improved geometry is evident in the increased number of stations with SW integrals that pass through each voxel (Figure 63). The voxels directly above and around the single frequency network are populated with ray paths from more than three different stations. Many voxels are pierced by more than six stations. The white areas in the figure correspond to the outside edges of the domain, where the station density and therefore ray path density decreases. In these sections, the tomography is aided by the horizontal smoothing constraints. It is clear that the use of single frequency data within this domain improves the geometry of the tomography solution. It also increases the computational effort to compute each solution. In the larger domain, there are 648 voxels. In the nested domain, there are 2860 voxels. This increase in matrix size drastically increased the time to compute each solution. Figure 64 plots the profile of water vapor density over station BURB. A comparison of this solution to the 1 km vertical resolution one in Figure 62 shows a more realistic vertical profile.

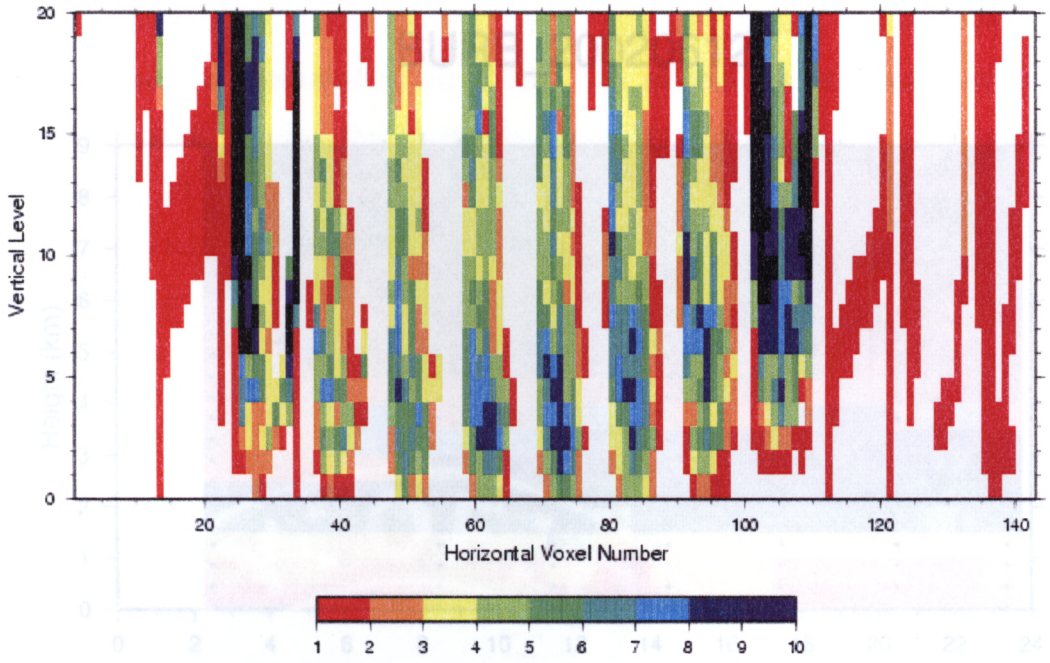

Figure 63: Graphical representation of the number of different stations containing a ray path passing through each voxel.

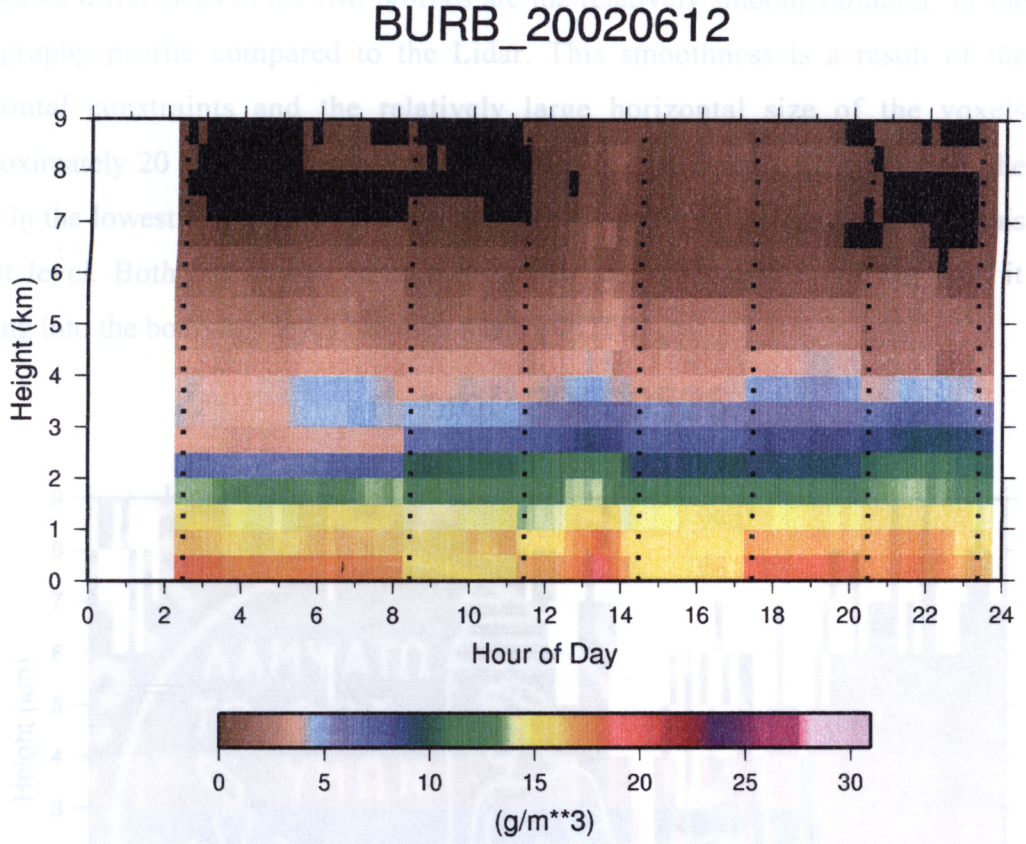

Figure 64: Time vs. height profile of water vapor density using a nested tomography domain and 500 m vertical resolution.

7.7.3 Tomography Solutions – Comparison to Raman Lidar

Figure 65 and Figure 66 plot the vertical profiles of water vapor density as a function of time and height above the ARM SGP central facility on May 26, 2002. Figure 65 is the profile as measured by the CART Raman Lidar [*Turner et al.*, 2000]. This profile has been averaged so that it has a vertical resolution of 1 km, matching the resolution obtained through the tomography estimate with GPS (Figure 66). The GPS tomography solution utilizes radiosonde observations to help initialize and constrain the vertical distribution of water vapor. Radiosonde launches occur at 3-hour intervals. The time of each launch is represented with the dotted line in the GPS profile. The initial tomography solution uses both the radiosonde profile and GPS SW observations. The tomography field is updated with a new estimate every 15 minutes, using the previous estimate as the a priori field. It can be seen from this comparison that the GPS tomography structure is similar to the Raman Lidar profile. The

significant differences in the two profiles are the relatively smooth variations of the tomography profile compared to the Lidar. This smoothness is a result of the horizontal constraints and the relatively large horizontal size of the voxels (approximately 20 km^2). The tomography solution is significantly different from the Lidar in the lowest 1 km. This is due to the poor geometry of the tomography in this lowest level. Both techniques capture the moist layer between 2 - 3 km with it merging into the boundary layer between 8 and 10 UTC.

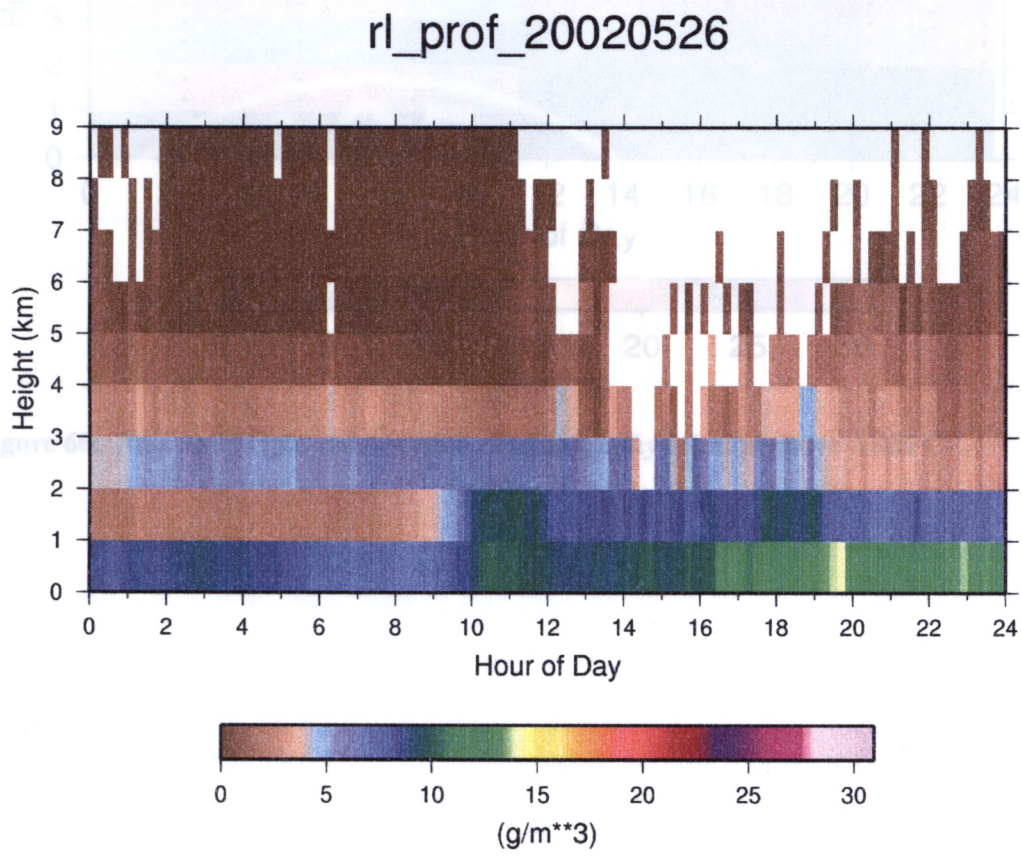

Figure 65: Time and height cross-section of water vapor density measured by the ARM Raman Lidar. The vertical resolution of the Lidar has been smoothed to match the 1 km resolution of the tomography.

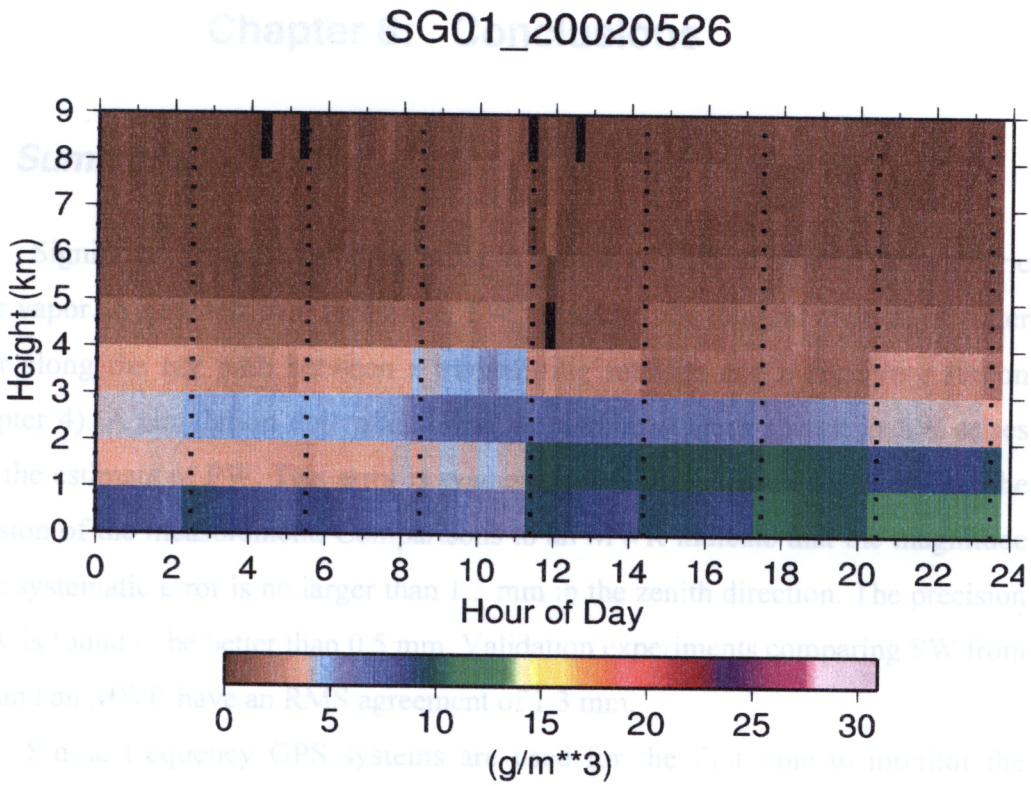

Figure 66: Time and height cross-section of tomography solution above ARM CF.

Chapter 8: Conclusions

8.1 Summary

Significant progress has been made in the use of GPS to observe atmospheric water vapor. A new retrieval technique, SW, measures the integral amount of water vapor along the ray path between a transmitting satellite and a receiving station (Chapter 4). A simulation determined that the dominant error source in SW arises from the estimate of PW. This error is systematic to a station and does not affect the precision of the measurement. Comparisons to an MWR indicate that the magnitude of the systematic error is no larger than 1.5 mm in the zenith direction. The precision of SW is found to be better than 0.5 mm. Validation experiments comparing SW from GPS and an MWR have an RMS agreement of 1.3 mm.

Single frequency GPS systems are used for the first time to monitor the neutral atmosphere (Chapter 5). The effects of the ionosphere are eliminated using GIMs to remove large-scale errors. Double differencing across short distances reduces any remaining small-scale errors to less than the precision of SW (<0.5 mm). A network of GPS stations on a scale of less than 500 km will produce only relative differences of PW. Absolute PW and SW are derived by including a dual frequency GPS station within the network of single frequency ones. This station is also incorporated into a larger continental network to derive absolute water vapor amounts. These new systems are of high geodetic quality. Station coordinate repeatability is found to be better than 2 mm in the horizontal and better than 5 mm in the vertical. The RMS agreement in zenith scaled SW between a dual frequency station and a single frequency one 30 meters away is 0.5 mm.

SW measurements from a network of GPS stations are incorporated into a tomographic inversion to compute three-dimensional fields of atmospheric water vapor (Chapter 6). The use of vertical profile information from an instrument such as a lidar or radiosonde improves the vertical resolution of the solution. Horizontal smoothing constrains voxels that are not pierced by SW ray paths. A simulation reveals that the tomography method resolves horizontal variability of more than 3

g/m^3 in elevated vertical layers. At ground level, the technique is only able to resolve a fraction of the 4 g/m^3 horizontal variability. The lowest level of the solution is hindered by the absence of crossing SW ray paths.

These three new techniques are utilized during the IHOP_2002 field experiment in May and June of 2002 (Chapter 7). Significant atmospheric structure in water vapor is observed in association with boundary layer dynamics. In the panhandle of Oklahoma, a GPS station recorded moisture differences across the dryline (Chapter 7, Section 3). Observations to the west were up to 3 mm drier than the average zenith scaled SW at that moment. This represented more than 13% of the total water vapor in the atmosphere. East of the dryline, fluctuations as large as 2.5 mm over 20 minutes were a result of mixing between dry and moist air at the top of the boundary layer. These differences occurred over horizontal distances of less than 10 km. On another day, the decay of shallow cumulus clouds produced an additional 3 mm in zenith scaled SW relative to the average SW at the station. Zenith scaled SW changed by 3.5 mm during a 15 minute period in the presence of horizontal convective rolls (Chapter 7, Section 4). Over these 15 minutes, the length of the SW ray path extended an additional 1 km through the boundary layer. This roughly matches the cloud pattern observed from the GOES-8 imagery.

In a statistical analysis, correlations in SW and the azimuthal variability of SW were computed (Chapter 7, Section 5). Under stable atmospheric conditions, with very little cloud formation, SW was highly correlated (>0.5) over nearly 1000 km. On stormy days, SW was negatively correlated over distances less than 100 km. The correlation in the azimuthal variability of SW (S_i^k) was less dependent on atmospheric conditions. Rarely was there positive correlation over distances longer than 10 km. Understanding the sensitivity of GPS SW in relation to length scales of boundary layer features might influence the design of future observing networks.

Diurnal changes in water vapor were also detected (Chapter 7, Section 6). During the night, the RMS of azimuthal variability in SW (S_i^k) was nearly 0.5 mm. This increased to almost 1.0 mm during the day. The timing of peak variability differed for stations across the Southern Great Plains. In the Oklahoma panhandle the maximum occurred around 1800 LST. In North-Central Oklahoma, the peak occurred

around 1400 LST. This difference is possibly related to differences in the land characteristics at each location.

Tomography solutions show interesting changes in the moisture field prior to, during, and after squall line passage (Chapter 7, Section 7). The total amount of zenith scaled SW increased from approximately 44 mm to more than 60 mm in under two hours. This increase in moisture stopped at the onset of rainfall. Most of this increase in moisture was transported from relatively weak southerly surface winds. Thirty minutes before rainfall, increased moisture is observed in tomography layers between 2 and 4 km. This elevated moisture remained in the atmosphere after the storm passed.

8.2 Discussion

The techniques developed here are a continuation of over 14 years of research in the application of GPS ground stations to observe the atmosphere. In some respects, this is a well-developed technology. There are now groups all around the world that are using GPS networks to monitor water vapor. These researchers are primarily using PW to accomplish this task. This useful measurement only provides a column average quantity. The research presented here extends the use of GPS to resolve horizontal and vertical variations in water vapor. Examples were given showing how it can successfully resolve important differences in the moisture field.

The measurement of SW has been discussed in detail. Multiple examples and comparisons to an MWR illustrate its usefulness. However, a systematic error has been identified (Chapter 4, Section 5). This error originates from the estimate of PW. A separate study questioned the usefulness of GPS SW in the presence of this systematic error [*Elosegui and Davis*, 2003]. Data assimilation studies and comparisons to other instruments indicate that GPS PW has a positive impact on numerical weather prediction and is a useful observation. The research presented here indicates that the retrieval of SW is at least as accurate as PW. Additionally, SW contains very precise information about the spatial distribution of water vapor around a station. This implies that GPS SW should be at least as valuable as any GPS derived PW value. Further research should be conducted on how this systematic error could

be reduced or eliminated. Improving the absolute accuracy of PW and SW will only increase the value of this technology.

The use of single frequency GPS stations can be considered an unconditional success. The results obtained from the network show no residual ionospheric error and significant structure in the water vapor field has been identified over length scales less than 10 km. The use of these low cost systems allowed for an improved sampling of the atmosphere.

The error characteristics presented here were derived through comparisons to other instruments, commonly an MWR. The tomography solutions do not contain any significant discussion of their errors. The formal errors that originate from the solution of these three-dimensional fields only quantify how well the densities within each voxel are able to reproduce the input SW. Given the smoothing constraints applied to the solution, and the fact that the inverse problem is nearly underdetermined, the formal errors are not useful quantities.

The tomography solutions recreate a realistic version of the atmosphere. It is unclear how accurate these solutions actually are. There are many possibilities to improve this technique. One significant improvement would involve the use of surface moisture measurements to help quantify water vapor amounts in the lowest level. Simply using humidity measurements from collocated surface instruments should improve the tomography fields. Another idea would be to include refractivity measurements from radars. The potential of this combination was illustrated with the S-Pol radar located in the Oklahoma panhandle during IHOP_2002. A second improvement is the density of the GPS stations. The quality of the tomography solution would improve with additional observations. Increases in both the horizontal extent and the density of stations would help. The ultimate realization of this would result in a unique tomographic solution that could be computed without the use of any smoothing constraints.

The next step in this research would is to assess the impact of SW on numerical weather models. An OSSE simulation indicates that SW can have a positive impact on numerical weather prediction [*Ha et al.*, 2002], but many challenges still exist. The results presented here illustrate the rapid temporal and

spatial variations that exist in the water vapor field. Significant changes in moisture are observed over time intervals less than 15 minutes and over horizontal distances of less than 10 km. It is not clear that current models can utilize this information.

Overall, the results in this work are encouraging. The potential of SW to improve the characterization of water vapor is clear. The expansion of continuously operating stations around the country and world should eventually provide the equipment infrastructure where GPS will make a positive impact on atmospheric science for years to come.

Bibliography

Alber, C., R.H. Ware, C. Rocken, and J.J. Braun, Obtaining single path phase delays from GPS double differences, *Geophysical Research Letters*, *27*, 2661-2664, 2000.

Aonashi, K., T. Iwabuchi, Y. Shoji, R. Ohtani, and R.-i. Ichikawa, Statistical study on precipitable water content variations observed with ground-based microwave radiometers, *Journal of the Meteorological Society of Japan*, *82* (1B), 269-275, 2004.

Bar-Sever, Y.E., P.M. Kroger, and J.A. Borjesson, Estimating horizontal gradients of tropospheric path delay with a single GPS receiver, *Journal of Geophysical Research*, *103*, 5109-5035, 1998.

Bates, J.J., and D.L. Jackson, Trends in upper-tropospheric humidity, *Geophysical Research Letters*, *28* (9), 1695-1698, 2001.

Bevis, M., S. Businger, S. Chiswell, T.A. Herring, R.A. Anthes, C. Rocken, and R.H. Ware, GPS Meteorology: Mapping zenith wet delays onto precipitable water, *Journal of Applied Meteorology*, *33*, 379-386, 1994.

Bevis, M., S. Businger, T.A. Herring, C. Rocken, R.A. Anthes, and R.H. Ware, GPS Meteorology: Remote sensing of atmospheric using the Global Positioning System, *Journal of Geophysical Research*, *97*, 15,787-15,801, 1992.

Braun, J.J., C. Rocken, and J. Liljegren, Comparisons of line-of-sight water vapor observations using the global positioning system and a pointing microwave radiometer, *Journal of Atmospheric and Oceanic Technology*, *20*, 606-612, 2003.

Braun, J.J., C. Rocken, and R.H. Ware, Validation of single slant water vapor measurements with GPS, *Radio Science*, *36*, 459-472, 2001.

Crook, N.A., Sensitivity of moist convection forced by boundary layer processes to low-level thermodynamic fields, *Monthly Weather Review*, *124*, 1767-1785, 1996.

Cucurull, L., F. Vandenberge, D. Barker, E. Vilaclara, and A. Rius, Three-dimensional variational data assimilation of ground-based GPS ZTD and meteorological observations during the 14 December 2001 storm event over the western mediterranean sea, *Monthly Weather Review*, *132* (3), 749-763, 2004.

Dabberdt, F., and T.W. Schlatter, Research opportunities from emerging atmospheric observing and modeling capabilities, *Bulletin of the American Meteorological Society*, *77*, 305-323, 1996.

Dai, A., J. Wang, R.H. Ware, and T. Van Hove, Diurnal variation in water vapor over North America and its implications for sampling errors in radiosonde humidity, *Journal of Geophysical Research*, *107* (D10), 2002.

Davis, J.L., G. Elgered, A.E. Niell, and C.E. Kuehn, Ground-based measurement of gradients in the "wet" radio refractivity of air, *Radio Science*, *28*, 1003-1018, 1993.

Davis, J.L., T.A. Herring, I.I. Shapiro, A.E. Rogers, and G. Elgered, Geodesy by radio interferometry: Effects of atmospheric modeling errors on estimates of baseline length, *Radio Science*, *20* (6), 1593-1607, 1985.

De Pondeca, M., and Z. Zou, A Case Study of the Variational Assimilation of GPS Zenith Delay Observations into a Mesoscale Model, *Journal of Applied Meteorology*, *40* (September), 1559-1576, 2001.

Elosegui, P., and J.L. Davis, Accuracy assement of slant path GPS signal delays,, in *International Workshop on GPS Meteorlogy*, Tsukuba, Japan, 2003.

Emanuel, K., Report of the first prospectus development team of the U. S. Weather Research Program to NOAA and NSF, *Bulletin of the American Meteorological Society*, *76*, 1194-1208, 1996.

Emardson, T.R., G. Elgered, and J.M. Johansson, Three months of continuous monitoring of atmospheric water vapor with a network of Global Positioning System receivers, *Journal of Geophysical Research*, *103*, 1807-1820, 1998.

Estey, L.H., and C.M. Meertens, TEQC: The Multi-Purpose Toolkit for GPS/GLONASS Data, *GPS Solutions*, *3* (1), 42-49, 1999.

Fabry, F., C. Frush, I. Zawadzki, and A. Kilambi, On the extraction of near-surface index of refraction using radar phase measurements from ground targets, *Journal of Atmospheric and Oceanic Technology*, *14*, 978-987, 1997.

Feltz, W.F., and J.R. Mecikalski, Monitoring high-temporal-resolution convective stability indices using the ground based atmospheric emitted radiance interferometer (AERI) during the 3 May 1999 Oklahoma-Kansas tornado outbreak, *Weather and Forecasting*, *17*, 445-455, 2002.

Flores, A.J., J.V.-G. de Arellano, L.P. Gradinarsky, and A. Rius, Tomography of the lower troposphere using a small dense network of GPS receivers, *IEEE Trans .Geosci .Remote Sensing*, *39*, 439-447, 2001.

Fritsch, J.M., and R.E. Carbone, Improving quantitative precipitation forecasts in the warm season, *Bulletin of the American Meteorological Society*, *85* (7), 955-965, 2004.

Ha, S.-Y., Y.-H. Kuo, Y.-R. Guo, C. Rocken, and T. Van Hove, Comparison of GPS slant wet delay measurements with model simulations during the passage of a squall line, *Geophysical Research Letters*, *29* (doi: 10.1029/2002GL015891), 2113-2116, 2002.

Haase, J., M. Ge, H. Vedel, and E. Calais, Accuracy and Variability of GPS Tropospheric Dealy Measurements of Water Vapor in the Western Mediterranean, *Journal of Applied Meteorology*, *42*, 1547-1568, 2003.

Hagemann, S., L. Bengtsson, and G. Gendt, On the determination of atmospheric water vapor from GPS measurements, *Journal of Geophysical Research*, *108*, 2003.

Hane, C.E., H.B. Bluestein, T.M. Crawford, M.E. Baldwin, and R.M. Rabin, Severe thunderstorm development in relation to along-dryline variability: A case study, *Monthly Weather Review*, *125*, 231-251, 1997.

Herring, T.A., The Global Positioning System, *Scientific American* (February), 1996.

Hofmann-Wellenhof, B., H. Lictenegger, and J. Collins, *GPS Theory and Practice*, Springer-Verlag Wien New York, 1992.

Hogg, D.C., F.O. Guiraud, and W.B. Sweezy, The short-term temporal spectrum of precipitable water vapor, *Science*, *213*, 1112-1113, 1981.

Hugentobler, U., S. Schaer, and P. Fridez, Bernese GPS software version 4.2, pp. 515, University of Berne, 2001.

Jarlemark, P.O.J., T.R. Emardson, and J.M. Johansson, Wet delay variability calculated from radiometric measurements and its role in space geodetic parameter estimation, *Radio Science*, *33*, 719-730, 1995.

Kaplan, E., D., Understanding GPS: principles and applications, pp. 554, Artech House, Inc, Norwood, MA, 1996.

King, R.W., and Y. Bock, Documentation for the GAMIT GPS Analysis software, Release 10.0, Scripps Institute of Oceanography, 2002.

Kuo, Y.-H., Y.-R. Guo, and E. Westwater, Assimilation of precipitable water measurements into a mesoscale numerical model, *Monthly Weather Review*, *121*, 619-643, 1993.

Kuo, Y.-H., X. Zuo, and Y.-R. Guo, Variational assimilation of precipitable water using nonhydrostatic mesoscale adjoint model, *Monthly Weather Review*, *124*, 122-147, 1996.

Lachapelle, G.C., E. Cannon, K. Keefe, and P. Alves, How will galileo improve positioning performance, *GPS World*, 2002.

Lamb, G., *The TDMA Book*, 211 pp., Cordero Consulting Inc, 1998.

Lieberman, R.S., D.A. Ortland, and E.S. Yarosh, Climatology and interannual variability of diurnal water vapor heating, *Journal of Geophysical Research*, *180* (D3), 2002.

MacDonald, A.E., Y. Xie, and R.H. Ware, Diagnosis of three-dimensinal water vapor using a GPS network, *Monthly Weather Review*, *130* (2), 386-397, 2002.

McCarthy, J., and S.E. Koch, The evolution of an Oklahoma dryline. Part I: A meso- and subsynoptic-scale analysis, *Journal of the Atmospheric Sciences*, *39*, 225-236, 1982.

Niell, A.E., Global mapping functions for the atmosphere delay at radio wavelengths, *Journal of Geophysical Research*, *101* (B1), 3227-3246, 1996.

Niell, A.E., Preliminary evaluation of atmospheric mapping functions based on numerical weather models, *Physics and Chemistry of the Earth*, *26*, 476-480, 2001.

Ohtani, R., and I. Naito, Comparisons of GPS-derived precipitable water vapors with radiosonde observations in Japan, *Journal of Geophysical Research*, *105*, 26917-26929, 2000.

Park, S.K., and K. Droegemeier, Sensitivity analysis of a moist 1D eulerian cold model using automatic differentiation, *Monthly Weather Review*, *127*, 2180-2196, 1999.

Park, S.K., and K. Droegemeier, Sensitivity analysis of a 3D convective storm: Implications for variational data assimilation and forecast error, *Monthly Weather Review*, *128*, 140-159, 2000.

Parkinson, B., W. , J. Spilker, J. Jr., P. Axelrad, and P. Enge, Global Positioning System: Theory and Applications I, in *Progress in Astronotics and Aeronautics*, edited by P. Zarchan, pp. 793, American Institute of Aeronautics and Astronautics, Inc., Washington, DC, 1996.

Parrish, D.F., and J.C. Derber, The National Meteorological Center's Spectral Statistical Interpolation Analysis System, *Monthly Weather Review*, *120*, 1747-1763, 1992.

Parsons, D.B., M.A. Shapiro, R.M. Hardesty, R.J. Zamora, and J.M. Intrieri, The finescale structure of a west Texas dryline, *Monthly Weather Review*, *119*, 1242-1258, 1991.

Peckham, S.E., R.B. Wilhelmson, L. Wicker, J. , and C.L. Ziegler, Numerical Simulation of the Interaction between the Dryline and Horizontal Convective Rolls, *Monthly Weather Review*, *132*, 1792-1812, 2004.

Revercombe, H.E., D.D. Turner, D.C. Tobin, R.O. Knuteson, W.F. Feltz, J. Barnard, J. Bosenberg, S. Clough, D. Cook, R. Ferrare, J. Goldsmith, S. Gutman, R. Halthore, B. Lesht, J. Liljegren, H. Linne, J. Michalsky, V. Morris, W. Porch, S. Richardson, B. Schmid, M. Splitt, T. Van Hove, E. Westwater, and D. Whiteman, The ARM program's water vapor intensive observation periods: Overview, initial accomplishments, and future challenges, *Bulletin of the American Meteorological Society*, *84* (2), 217-236, 2003.

Rocken, C., The global positioning system: A new tool for tectonic studies, Ph. D. thesis, University of Colorado, Boulder, 1988.

Rocken, C., J.M. Johnson, J.J. Braun, H. Kawawa, Y. Hatanaka, and T. Imakiire, Improving GPS surveying with modeled ionospheric corrections, *Geophysical Research Letters*, *27*, 3821-3824, 2000.

Rocken, C., J.M. Johnson, R.E. Neilan, M. Cerezo, J.R. Jordan, M.J. Falls, L.D. Nelson, R.H. Ware, and M. Hayes, The measurement of atmospheric water vapor: Radiometer comparison and spatial variations, *IEEE Transactions on Geosciences and Remote Sensing*, *29*, 3-8, 1991.

Rocken, C., S. Sokolovskiy, J.M. Johnson, and D. Hunt, Improved mapping of tropospheric delays, *Journal of Atmospheric and Oceanic Technology*, *18* (7), 1205-1213, 2001.

Rocken, C., T. Van Hove, J.M. Johnson, F. Solheim, and R.H. Ware, GPS/STORM - GPS sensing of atmospheric water vapor for meteorology, *Journal of Atmospheric and Oceanic Technology*, *12*, 468-478, 1995.

Rocken, C., T. Van Hove, and R.H. Ware, Near real-time GPS sensing of atmospheric water vapor, *Geophysical Research Letters*, *24*, 3221-3224, 1997.

Rocken, C., R.H. Ware, T. Van Hove, F. Solheim, C. Alber, and J.M. Johnson, Sensing atmospheric water vapor with the Global Positioning System, *Geophysical Research Letters*, *20*, 2631-2634, 1993.

Saastamoinen, J., Introduction to practical computation of astronomical refraction, *Bulletin Geodesique*, *106*, 383-397, 1972.

Schaer, S., Mapping and Predicting the Earth's Ionosphere Using the Global Positioning System, PhD thesis, University of Bern, Bern, 1999.

Smith, E.K., and S. Weintraub, The constants in the equation for atmospheric refractive index at radio frequencies, *Journal of Research of the National Bureau of Standards*, *50*, 39-41, 1953.

Soden, B.J., Tracking upper tropospheric water vapor radiances: A satellite perspective, *Journal of Geophysical Research*, *103* (D14), 17,069-17,081, 1998.

Sokolovskiy, S., C. Rocken, and A.R. Lowry, Use of GPS for estimation of bending angles of radio waves at low elevations, *Radio Science*, *36* (3), 473-482, 2001.

Stensrud, D.J., Importance of low-level jets to climate: A review, *Journal of Climate*, *9*, 1698-1711, 1996.

Strang, G., *Linear Algebra and its Applications*, Harcourt Brace Jovanovich Inc., Fort Worth, TX, 1988.

Treuhaft, R.N., and G.E. Lany, The effect the dynamic wet troposphere on radio interferometric measurements, *Radio Science*, *22*, 251-265, 1987.

Turner, D.D., W.F. Feltz, and R. Ferrare, Continuous water vapor profiles from operational active and passive remote sensors, *Bulletin of the American Meteorological Society*, *81*, 1301-1317, 2000.

Weckwerth, T., D.B. Parsons, S.E. Koch, J.A. Moore, M.A. Lemone, B.B. Demoz, C. Flamant, B. Geerts, J. Wang, and W.F. Feltz, An overview of the International H20 project (IHOP_2002) and some preliminary highlights, *Bulletin of the American Meteorological Society*, *85* (2), 253-277, 2004.

Weckwerth, T., J.W. WIlson, R.M. Wakimoto, and N.A. Crook, Horizontal Convective Rolls: Determining the Environmental Conditions Supporting their Existence and Characteristics, *Monthly Weather Review*, *125*, 505-526, 1997.

Weckwerth, T., V. Wulfmeyer, R.M. Wakimoto, R.M. Hardesty, J.W. Wilson, and R.M. Banta, NCAR-UCAR lower-tropospheric water vapor workshop, *Bulletin of the American Meteorological Society*, *80*, 2339-2356, 1999.

Wessel, P., and W.H.F. Smith, New, improved version of Generic Mapping Tools released, *EOS Trans. Amer. Geophys. U.*, *79* (47), 579, 1998.

Whiteman, D., Examination of the traditional Raman Lidar technique II: Evaluating the ratios for water vapor and aerosols, *Applied Optics*, *42* (15), 2593, 2003.

Wolfe, D.E., and S. Gutman, Development of the NOAA/ERL Ground-Based GP SWater Vapor Demonstration Network: Design and Initial Results, *Journal of Atmospheric and Oceanic Technology*, *17*, 426-440, 2000.

Xin, L., and G.W. Reuter, Numerical simulation of the effects of mesoscale convergence on convective rain showers, *Monthly Weather Review*, *124*, 2828-2842, 1996.

Ziegler, C.L., T.J. Lee, and R.A. Pielke, Sr, Convection initiation at the dryline: A modeling study, *Monthly Weather Review*, *1997* (125), 1001-1026, 1997.

Zumberge, J.F., M.B. Heflin, D.C. Jefferson, M.M. Watkins, and F.H. Webb, Precise point positioning for the efficient and robust analysis of GPS data from large networks, *Journal of Geophysical Research*, *201* (B3), 5005-5017, 1997.

Appendix 1

The article "Validation of single slant water vapor measurements with GPS", by J. J. Braun, C. Rocken, and R.H. Ware is included as a portable document file (.pdf) in the accompanying CD.

Appendix 2

The article "Comparisons of line-of-sight water vapor observations using the global positioning system and a pointing microwave radiometer", by J. J. Braun, C. Rocken, and J. Liljegren is included as a portable document file (.pdf) in the accompanying CD.

Remote Sensing of Atmospheric Water Vapor with the Global Positioning System

A Dissertation

John Joseph Braun

B. A., University of Colorado, 1991

M. S., University of Colorado, 1997

A thesis submitted to the

Faculty of the Graduate School of the

University of Colorado in partial fulfillment

of the requirements for the degree of

Doctor of Philosophy

Department of Aerospace Engineering Sciences

2004

This thesis entitled:
Remote Sensing of Atmospheric Water Vapor with the Global Positioning System

Written by John Joseph Braun
Has been approved for the Department of Aerospace Engineering Sciences.

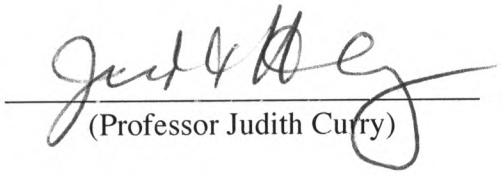

(Professor Judith Curry)

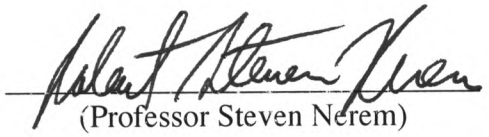

(Professor Steven Nerem)

Date:_____

The final copy of this thesis has been examined by the signatories, and we find that both the content and the form meet acceptable presentation standards of scholarly work in the above mentioned discipline.

Abstract

Braun, John Joseph (Ph. D., Aerospace Engineering Sciences)
Remote Sensing of Atmospheric Water Vapor with the Global Positioning System
Thesis directed by Professor Judith Curry

Signals from the Global Positioning System (GPS) are used to retrieve the integrated amount of water vapor along the path between a transmitting satellite and a receiving station. This integrated quantity is called slant water vapor (SW). Measurements of SW allow for an improved assessment of the spatial distribution of water vapor within the atmosphere. This technique is developed and validated through simulations and comparisons to similar measurements from a pointing microwave water vapor radiometer. Absolute accuracy of zenith scaled SW is found to be 1.5 mm with a relative precision that is better than 0.5 mm. Dual and single frequency GPS stations are used to measure SW. Previously, only dual frequency GPS stations have been used for atmospheric remote sensing. The use of single frequency stations, which are significantly less expensive than dual frequency ones, allows for a denser placement of stations. The effects of the ionosphere on single frequency GPS observations are eliminated using global ionosphere models and double difference processing with short station separation. Networks of GPS stations are deployed in the Southern Great Plains of the United States. Combining SW measurements from all stations within a dense network allows for an estimation of the three dimensional distribution of water vapor above the network. This tomographic technique is improved by including vertical profiles from radiosondes. The retrieval of SW is utilized during the International H_20 Project 2002 (IHOP_2002). Significant water vapor structure is observed within the atmospheric boundary layer, including dryline convergence and horizontal convective rolls. Tomography results computed during squall line passage indicate elevated levels of water vapor in the free troposphere prior to the onset of rainfall. A statistical analysis of the results obtained during IHOP_2002 show coherent water vapor structure across horizontal lengths ranging from less than 1 to almost 100 kilometers. A significant diurnal cycle of atmospheric water vapor variability is also found.

Dedication

To Stephanie, Jackson and Riley.

Acknowledgements

This research was supported through a graduate student fellowship from the Advanced Study Program at the National Center for Atmospheric Research (NCAR); and by the Biological and Environmental Research Program (BER), U. S. Department of Energy Grant DE-FG03-02ER63327.

Various people and groups supplied data that were used in this research. Joel Van Baelen at Centre National de la Recherché Scientifique (CNRS), France provided data from GPS stations deployed by CNRS during the International H_20 Project 2002 (IHOP_2002). Meteorological data were obtained from the Atmospheric Radiation Measurement (ARM) Program sponsored by the U.S. Department of Energy, Office of Science, Office of Biological and Environmental Research, Environmental Sciences Division. Surface meteorological data during IHOP_2002 were used from the Oklahoma Mesonet Network.

Victoria Andreatta and Chuck Kurnik at the University NAVSTAR Consortium (UNAVCO) helped deploy the single frequency GPS stations. Their work was greatly appreciated. "Corky," Fred Mack, and Sandy Mack assisted in contacting farmers, station installation, station maintenance, and the use of their farm as a base of operations was invaluable. The members of the "L1" team at UNAVCO deserve recognition for their help in building and testing the single frequency GPS stations. This included Dr. Chuck Meertens, Dr. Lou Estey, Dave Mencin, and Curt Conquest.

The thesis committee of Dr. Judith Curry, Dr. Steve Nerem, Dr. Kristine Larson, Dr. Peter Molnar, Dr. Christian Rocken, and Dr. Bill Kuo provided useful comments and questions about this research. Their input was greatly appreciated. In particular, Dr. Rocken and Dr. Kuo offered insightful analysis throughout the project.

The researchers in the COSMIC program also deserve recognition for their critique and support of this research. This group includes Stick Ware, Jim Johnson, Teresa Van Hove, So-Young Ha, Doug Hunt and Bill Schreiner.

The majority of the figures were created with the Generic Mapping Tools (GMT) software package [*Wessel and Smith*, 1998].

Contents

Remote Sensing of Atmospheric Water Vapor with the Global Positioning System i
Abstract iii
Dedication iv
Acknowledgements v
Contents vi
List of Tables viii
List of Figures ix
Chapter 1: Introduction 1
1.1 The Significance of Water Vapor in the Atmosphere 1
1.2 Previous Research 1
1.3 Scientific Achievements from this Research 2
1.4 Thesis Organization 3
Chapter 2: Atmospheric Water Vapor 5
2.1 The Need for Improved Observational Techniques 5
2.2 Water Vapor Within the Boundary Layer 5
2.3 Moisture and Convection 6
2.4 Temporal and Spatial Variability of Water Vapor 7
2.5 Chapter Summary 9
Chapter 3: The Global Positioning System 10
3.1 Overview 10
3.2 Satellite Constellation 10
3.3 GPS Signals and Observations 11
3.4 International GPS Service 13
3.5 Observation Equation 15
3.6 Linear Combinations of Observations 15
3.7 Differences of Observations 16
3.8 GPS Analysis Software 17
3.9 Other GNSS Systems 19
Chapter 4: Slant Water Vapor 20
4.1 Overview 20
4.2 The Neutral Atmosphere and GPS 20
4.3 Scaling ZWD to PW 23
4.4 Slant Water Vapor Retrieval 24
4.5 Simulation Experiment 29
4.6 Slant Water Vapor Experiment - Platteville, CO 39
4.7 Slant Water Vapor Experiment - Lamont, OK 41
4.8 Chapter Summary 43
Chapter 5: Single Frequency GPS Stations 45
5.1 Overview 45
5.2 System Components 45
5.2.1 GPS Receiver 46
5.2.2 GPS Antenna 48
5.2.3 Radio Modem 51

5.2.4 Power/Battery Backup 52
5.3 CMC Receiver Performance 53
5.4 Processing Strategy 55
5.5 Network Deployment 57
5.6 Geodetic Results 58
5.7 Atmospheric Results 60
5.8 Ionospheric Error 61
Chapter 6: Tomography of the Atmosphere 63
6.1 Overview 63
6.2 The Inverse Problem 63
6.3 Horizontal Constraints 66
6.4 Improvement of the Vertical Profile 69
6.5 Solution Using Constraints 72
6.6 Simulation 72
6.7 Sequential Estimation 75
Chapter 7: The International H_20 Project (IHOP_2002) 77
7.1 Overview 77
7.2 GPS Network 77
7.3 Boundary Layer Structures – the Dryline 78
7.3.1 May 22, 2002 79
7.3.2 May 30, 2002 85
7.4 Boundary Layer Structures – Horizontal Convective Rolls 91
7.5 Spatial Correlation of SW and S_i^k 96
7.6 Diurnal Evolution of the Boundary Layer 100
7.7 Tomography Solutions 102
7.7.1 Squall Line – June 12, 2002 103
7.7.2 Nested Tomography – June 12, 2002 108
7.7.3 Tomography Solutions – Comparison to Raman Lidar 111
Chapter 8: Conclusions 114
8.1 Summary 114
8.2 Discussion 116
Bibliography 119
Appendix 1 124
Appendix 2 125

List of Tables

Table 1: GPS Satellite Constellation Characteristics 11
Table 2: GPS Signal Characteristics..... 11
Table 3: IGS Derived Data Products 14
Table 4: Significant Components of Single Frequency GPS Stations 45

List of Figures

Figure 1: Map of "global" IGS stations (http://igscb.jpl.nasa.gov) 14
Figure 2: Diagram of processing steps in the computation of GPS SW 28
Figure 3: Model output fields used in the SW simulation – pressure and temperature (top), precipitable water (middle), hourly accumulation of rainfall (bottom) 30
Figure 4: Simulated, zenith scaled, hydrostatic delay (lower), wet delay (middle), and total delay (upper). Each color represents a different satellite. 32
Figure 5: Simulated delays for station NDSK 33
Figure 6: The network of stations used in the SW simulation. Red diamonds represent stations within the 3-km domain. Black diamonds represent stations in the 25-km domain 34
Figure 7: Comparison of Simulated SWD (red) and retrieved SWD (blue) for station LMNO. 35
Figure 8: Simulated SWD (red) and retrieved SWD (blue) for station PRCO 35
Figure 9: Individual satellite traces for LMNO. Simulated SW plotted as the thinner red line. Retrieved SWD plotted as the thinner blue line. Half hour averages of simulated zenith scaled SWD are shown as red dots. Half-hour ZWD estimates are shown as blue dots. 36
Figure 10: Individual satellite traces for station PRCO. The labeling is the same as Figure 9. 37
Figure 11: Linear correlation of simulated SWD against retrieved ZWD (black) and retrieved SWD (red). The error in the ZWD estimate has been removed in the retrieved SWD. 39
Figure 12: SW signal, GPS measurement noise, and MWR measurement noise plotted as a function of satellite elevation angle. Figure originally from Braun et al. 2001 41
Figure 13: GPS antenna (left) and MWR (right) collocated at ARM Central Facility 42
Figure 14: Examples of retrieved SW from Braun 2003 et al. 43
Figure 15: Single frequency GPS stations operating in north-central Oklahoma. The station on the right continued operation after being vandalized with a shotgun. 46
Figure 16: Zero difference residuals from single frequency receiver. The 50-point running standard deviation is plotted as the red line. 47
Figure 17: Zero difference residuals from dual frequency receiver. The 50-point running standard deviation is plotted as the red line. 48
Figure 18: Signal-to-Noise (SNR) values in dBm for Micropulse patch antenna without multipath suppression 50
Figure 19: SNR values in dBm of Micropulse antenna with rolled edge ground plane. 50
Figure 20: Data collection statistics for station 1N1W 52
Figure 21: Diagram of baseline formation using single frequency stations (green) and dual frequency stations (red). 57
Figure 22: Map of single frequency GPS stations (black diamonds) relative to ARM SGP central facility (red star). 58
Figure 23: Time series of coordinate solutions for single frequency station 0N1E. 59

Figure 24: Time series of coordinate solutions for single frequency station 2N2W...60
Figure 25: Scatter plot of dual frequency SW vs. single frequency SW collected during IHOP_2002.....61
Figure 26: Scatter plot of zero difference residuals from a single frequency station and the rate of change of the ionosphere.....62
Figure 27: Cartoon representation approximating SW measurement within voxels...65
Figure 28: Graphical representation of the number of different stations containing a ray path passing through each voxel.....67
Figure 29: A ground based GPS station would measure the same integrated SW for a homogeneous layer of water vapor located at any height.....69
Figure 30: Improvement in Vertical Profile Using Additional Information.....71
Figure 31: Scatter plot (left) of simulated vs. retrieved densities for each voxel. Density plotted as function of altitude (right) for simulated (black) and retrieved (red) values.....74
Figure 32: Simulated (left) and retrieved (right) water vapor fields for layer from ground level to 0.5 km.....74
Figure 33: Simulated (left) and retrieved (right) water vapor fields between 1.5 and 2.0 km altitude.....75
Figure 34: GPS stations in the Southern Great Plains region during the IHOP_2002 experiment.....78
Figure 35: Surface conditions from the Oklahoma Mesonet at 21:30 UTC (4:30 CST) on May 22, 2002.....81
Figure 36: S-Pol surface refractivity field at 2145 UTC (4:45 CST) on May 22, 2002. The location of the GPS station is shown as the red star.....81
Figure 37: Time-height cross section of water vapor mixing ratio as measured by the GSFC scanning Raman Lidar on May 22, 2002.....82
Figure 38: Vertically scaled GPS SW (blue diamonds) from the Oklahoma panhandle station SA14. The half hour GPS PW estimates are in red.....82
Figure 39: Zenith scaled SW from station SA14 to satellite 3 is shown in red. The average of all zenith scaled SW is plotted in black. The satellite azimuth and elevation is plotted in the small sky plot in the lower left corner.....83
Figure 40: Zenith scaled SW from station SA14 to satellite 9. The data in the plot are represented in the same manner as Figure 39.....83
Figure 41: Zenith scaled SW from station SA14 to satellite 29. The data in the plot are represented in the same manner as Figure 39.....84
Figure 42: S-Pol surface refractivity field at 2245 UTC (5:45 CST) on May 22, 2002. The location of the GPS station is shown as the red star. As satellite 29 set, it passed through the moist cell identified with the red arrow.....85
Figure 43: GOES-8 visible imagery at 1 km resolution on 30/May/2002 at 1908 UTC. 87
Figure 44: GOES-8 visible imagery at 1 km resolution on 30/May/2002 at 2233 UTC. Small cumulus clouds had formed along the dryline running southwest to northeast through the Oklahoma panhandle.....88
Figure 45: Time-height cross section of water vapor mixing ratio as measured by the GSFC scanning Raman Lidar on May 30, 2002.....89

Figure 46: GPS PW (red diamonds) and zenith scaled SW (blue diamonds) at the SA14 station located in the panhandle of Oklahoma. 89
Figure 47: Zenith scaled SW from station SA14 to satellite 3 on May 30, 2002. The data in the plot are represented in the same manner as Figure 39. 90
Figure 48: Zenith scaled SW from station SA14 to satellite 15. The data in the plot are represented in the same manner as Figure 39. 90
Figure 49: Comparisons of GPS (red) and MWR (blue) from Braun et al 2003 paper. The top panel plots the S_i^k component of SW, the lower panel plots zenith scaled SW. 92
Figure 50: GOES-8 visible imagery at 1 km resolution on June 9, 2002 at 2039 UTC. Horizontal convective rolls exist over large sections of Oklahoma. 93
Figure 51: Surface conditions from the Oklahoma Mesonet at 2030 UTC (3:30 CST) on June 9, 2002. 94
Figure 52: GPS PW (red diamonds) and zenith scaled SW (blue diamonds) station SG01 on June 9, 2002. 94
Figure 53: Zenith scaled SW from station SG01 to satellite 15 on June 9, 2002. The data in the plot are represented in the same manner as Figure 39. 95
Figure 54: Zenith scaled SW from station SG01 to satellite 18 on June 9, 2002. The data in the plot are represented in the same manner as Figure 39. 96
Figure 55: Linear correlation of SW (bottom) and S_i^k (top) as a function of station separation for May 23, 2002 98
Figure 56: Linear correlation of SW (bottom) and S_i^k (top) as a function of station separation for May 31, 2002 99
Figure 57: Diurnal variation in the non-isotropic component of SW (S_i^k) for Lamont, OK during the IHOP_2002 campaign 101
Figure 58: Diurnal variation in the non-isotropic component of SW (S_i^k) for Oklahoma Panhandle station SA14 during IHOP_2002. 102
Figure 59: Composite WSR-88D radar reflectivity on June 12, 2002 at 1200 UTC (top) and 1300 UTC (bottom) 105
Figure 60: Interpolated maps of 30-minute PW estimates on June 12, 2002 beginning at 1200 UTC (top) and 1330 UTC (bottom). The stations used in the interpolation are shown as diamonds. 106
Figure 61: Surface meteorological observations (top panel) and GPS derived water vapor amounts (bottom panel) for station BURB on June 12, 2002. In the top panel the surface temperature is in red, the dew point temperature in blue, accumulated rain is plotted in black and the wind speed and direction is plotted using the vectors at the top. In the bottom panel the GPS PW are the red diamonds and the zenith scale SW are the blue diamonds 107
Figure 62: Surface meteorological observations (top) and time-height profile of water vapor density (bottom) for station BURB on June 12, 2002 108
Figure 63: Graphical representation of the number of different stations containing a ray path passing through each voxel. 110
Figure 64: Time vs. height profile of water vapor density using a nested tomography domain and 500 m vertical resolution 111

Figure 65: Time and height cross-section of water vapor density measured by the ARM Raman Lidar. The vertical resolution of the Lidar has been smoothed to match the 1 km resolution of the tomography..... 112
Figure 66: Time and height cross-section of tomography solution above ARM CF. 113

Chapter 1: Introduction

1.1 The Significance of Water Vapor in the Atmosphere

Water, in its three phases, is a foundation for life on Earth. The transitions of water from one phase to another regulate the temperature of the Earth's surface making it hospitable for mankind. The global transport of water acts to redistribute energy around the world and is a driving force in its climate and weather system. The research presented here improves the characterization of one component of the Earth's hydrological cycle, atmospheric water vapor.

Water vapor is both the most abundant and most variable green house gas in the atmosphere. It affects the Earth's radiation budget, energy transfer, cloud formation, and precipitation distribution. For radiation transfer, water vapor absorbs both downwelling solar and upwelling longwave radiation. For energy transfer, the latent heat of evaporation is a principal path for the transport of energy from the equator to higher latitudes. The energy released when vapor condenses to form clouds affects the dynamics of the atmosphere. Through this interaction, the vertical stability of the atmosphere is modified, influencing weather systems and their associated precipitation patterns.

While being such a key element in the atmosphere, accurate measurements of water vapor are not readily available. Improving and expanding the techniques to measure water vapor has been identified as a key area of research by the U.S. Weather Research Program [*Dabberdt and Schlatter*, 1996; *Emanuel*, 1996]. The lack of detailed and accurate measurements hinders our ability to model and predict the Earth's climate and forecast weather.

1.2 Previous Research

The Global Positioning System (GPS) provides a relatively inexpensive method to remotely sense atmospheric water vapor in all weather conditions. Initial investigations focused on the measurement of the vertically integrated amount of

water vapor as observed by a ground based GPS station [*Bevis et al.*, 1992; *Rocken et al.*, 1991; *Rocken et al.*, 1995]. Vertically integrated water vapor is commonly termed precipitable water vapor (PW). GPS methods to remotely sense PW are now well developed and the technique has been implemented in an operational mode [*Hagemann et al.*, 2003; *Ohtani and Naito*, 2000; *Rocken et al.*, 1997; *Wolfe and Gutman*, 2000].

GPS PW has been used to investigate the accuracy of moisture fields in numerical weather models [*Haase et al.*, 2003]. GPS PW has also been directly assimilated into models to improve their predictive capability [*Cucurull et al.*, 2004; *De Pondeca and Zou*, 2001; *Kuo et al.*, 1993; *Kuo et al.*, 1996]. Additionally, continuous time series of GPS PW are now being used to detect and quantify spatial and temporal variations in water vapor on seasonal and diurnal time scales [*Dai et al.*, 2002; *Hagemann et al.*, 2003].

1.3 Scientific Achievements from this Research

There are three significant achievements presented in this thesis. First, a new technique to measure atmospheric water vapor is developed. This technique measures the integrated amount of water vapor along the path between a transmitting GPS satellite and a receiving antenna. This integral, termed slant water vapor (SW) differs from PW in that it quantifies the amount of water vapor in a specific direction. While PW is a column average of atmospheric water vapor over both space and time, SW provides an instantaneous measurement to individual satellites visible from a station and therefore provides an improved sampling of the spatial distribution of atmospheric water vapor. The remote sensing technique used to obtain SW is described and verified through a simulation and comparisons to other instruments.

The second innovation is the use of single frequency GPS stations as atmospheric remote sensing instruments. These single frequency stations were developed, built, installed, and operated as part of this research. These stations are low cost and can be deployed in relatively large quantities to form a dense array. Special processing methods have been developed to minimize errors associated with the ionosphere. A network of stations is currently in operation in the Southern Great

Plains of the United States. Their primary purpose is to observe the variability of water vapor on horizontal scales of 1-2 km or less.

The third innovation is the combination of data collected from a network of GPS stations to derive the three dimensional distribution of water vapor with horizontal scales of less than 100 km and vertical scales of less than 1 km. SW measurements are combined into four-dimensional estimates of the water vapor field using tomographic inversion techniques. The spatial density of the stations allows for the resolution of mesoscale and microscale variations of the water vapor field.

The results presented were primarily obtained in the Southern Great Plains region of the Central United States. The variation and severity of the weather events in this area makes it an ideal test bed for evaluating new measurement techniques. The precise location is around the Department of Energy's (DOE) Atmospheric Radiation Measurements (ARM) Southern Great Plains (SGP) central facility near Lamont, OK. The meteorological instruments at this facility are used for validation and to provide constraints on the vertical structure of the atmosphere around the network. The results are primarily from instrument comparisons from the summer of 2000 and during the International H_20 Project in May and June of 2002 (IHOP_2002). The objective of IHOP_2002 was to characterize the water vapor field using state of the art instrumentation and quantify how useful these observations are in helping to improve warm season rainfall prediction, a forecast where numerical weather prediction lacks the most skill.

1.4 Thesis Organization

Following the introduction in this chapter, Chapter 2 outlines the need and application of GPS sensed water vapor observations. Chapter 3 describes the basics of GPS with an emphasis on the elements that are relevant to this research. Chapter 4 details the technique of retrieving SW from GPS, outlining a simulation experiment as well as a summary of two validation experiments which are more completely presented in Appendices 1 and 2. Chapter 5 describes the single frequency GPS stations that were developed. Chapter 6 presents the tomographic technique that was implemented. Chapter 7 presents a summary of results from the IHOP_2002

experiment. Finally, Chapter 8 summarizes this research and outlines areas of improvement and application for further studies.

Chapter 2: Atmospheric Water Vapor

2.1 The Need for Improved Observational Techniques

The primary goal of the research presented here is to improve the capability to measure atmospheric water vapor. This topic was discussed in the "NCAR-UCAR Lower Tropospheric Water Vapor Workshop" summarized by Weckwerth et al [1999]. The meeting highlighted the need for observations covering all time and space scales, temporally ranging from seconds to days and spatially varying from a few meters to hundreds of kilometers. There were six major recommendations contained within this summary. The research conducted in this thesis directly addresses two of the recommendations. (1) "*The community should explore ground-based tomography techniques for four- dimensional water vapor analyses.*" and (2) "*The community should develop a low-cost ($100,000 - $200,000), continuously operating, moderate resolution water vapor profiler to operate as part of a network.*" Areas of atmospheric research that were mentioned in the report that could benefit from the techniques developed here include boundary layer studies, atmospheric chemistry, climate, polar research, and numerical weather prediction (including precipitation, severe weather forecasts and convection initiation). This chapter reviews three fields of research in atmospheric science that benefit from this thesis.

2.2 Water Vapor Within the Boundary Layer

The boundary layer represents the lowest 1-3 km of the atmosphere and typically contains the majority of water vapor within the column. Moisture observations are not readily available within this region. Surface measurements are strongly related to land-air interactions and do not accurately represent the entire boundary layer, while conventional satellite sounding instruments do not work well at low altitudes. The boundary layer is most commonly measured using (1) ground based sounding instruments such as radiosondes and Lidars, (2) towers with meteorological sensors placed at various altitudes, and (3) in-situ aircraft

measurements. These techniques are all relatively expensive, and are not suitable for continuous monitoring over significant time and/or space scales. Detailed observations of boundary layer moisture are needed to validate and understand the processes that occur and how they affect the broader atmospheric system.

Horizontal convective rolls can be described as horizontal vortices whose spin axes are aligned with the boundary layer wind field [*Peckham et al.*, 2004; *Weckwerth et al.*, 1997]. They can have wavelengths of 2-10 km and initiate convection by concentrating and lifting water vapor within the boundary layer. Convective rolls have been directly observed with measurements from aircrafts, towers, and sounding instruments such as Lidars and radiosondes. Previous simulations and observational studies indicate that rolls can alter the water vapor mixing ratio by as much as 1-2.5 g/kg within the boundary layer. Under proper conditions, this increase can induce cloud formation and possibly convection.

The dryline, and it's strong influence on weather events has been discussed in numerous papers [*Hane et al.*, 1997; *McCarthy and Koch*, 1982; *Parsons et al.*, 1991; *Ziegler et al.*, 1997]. The dryline that commonly occurs in the Southern Great Plains is essentially a low level atmospheric boundary between dry air that undergoes adiabatic heating as it subsides from the Rocky Mountains and moist air that is advected north and west from the Gulf of Mexico. It is often times associated with intense convection and severe weather. The horizontal boundary of a dryline can vary in width between 2 and 20 km, and model analysis indicates it can be as deep as 4-5 km in areas where strong low-level convergence has occurred. Analysis of moisture variability of dryline events has mostly involved surface dew point measurements from surrounding mesonet stations and aircraft observations for specific experiments. In a numerical modeling study of three storms initiated along drylines [*Ziegler et al.*, 1997], mixing ratio variations of up to 8 g/kg over horizontal and vertical length scales of a few km were computed.

2.3 Moisture and Convection

Convection in the absence of external forcing is directly related to the convergence of moisture in the planetary boundary layer. This convergence of

moisture aids in the removal of convective inhibition (CIN) in a strict parcel lifting theory of convection. Xin and Reuter [1996] simulated a convective storm in the absence of vertical wind shear using an axisymetric model. The result of this simulation was to reveal that rainfall is controlled by the moisture convergence below clouds. They also showed that the timing and quantity of rainfall varied with the depth of the convergence zone, given a fixed vertical mass flux. This can be explained that for a given mass flux in the boundary layer, the moisture flux tends to be largest in the lowest levels of the convergence field. Shallow convergence zones injected more moisture above the level of free convection and subsequently increased the rainfall within the simulation. In another study of convection in the absence of larger scale forcing, Crook [1996] determined that once convection was well developed, the strength of the convection (defined as the maximum vertical velocity (w_{max})) was 2.5 times more sensitive to variations in moisture than temperature in the convective boundary layer.

Severe storm prediction is limited by moisture observations throughout the troposphere. Sensitivity studies [*Park and Droegemeier*, 1999; *Park and Droegemeier*, 2000] indicate that a lack of accurate observational moisture measurements throughout the troposphere limits the forecast of severe storms over time scales as short as 30 minutes. In these studies, a 1% variation in water vapor within and around a storm cell had a significant and measurable affect on storm intensity. It was also reported that the variation in water vapor above the convective boundary layer directly affected the entrainment and vertical velocity characteristics of the storm.

2.4 Temporal and Spatial Variability of Water Vapor

There is relatively little information available on the variability of water vapor over short time (shorter than a few hours) and spatial scales (smaller than a few hundreds of kilometers). Knowledge of realistic spatial and temporal variations of moisture allows climate and weather modelers to compare statistics of their simulated moisture fields to realistic observations. These comparisons are essential in quantifying how well the models perform.

Radiosondes, being the most frequently used platform to measure atmospheric water vapor, do not possess either the temporal or the spatial resolution to infer information about the state of the atmosphere smaller than synoptic scales. Satellites provide measurements of upper troposphere humidity [*Bates and Jackson*, 2001; *Soden*, 1998] and can continuously monitor the atmosphere, but do not have the spatial resolution to observe features smaller than a few tens of kilometers. Generally, the studies of small-scale atmospheric water vapor utilize either microwave water vapor radiometers (MWRs) or GPS estimates of total column water vapor. These studies mostly focus on the measurement of precipitable water (PW) measured in units of mm, relating the integrated amount of water vapor in a column of air to an equivalent column of liquid water.

The temporal structure of the atmosphere has been studied by Hogg et al., [1981] and Jarlemark et al., [1995]. Both studies tried to find a power structure relationship between PW variability and time ($S(\tau) = c\tau^{\alpha}$, where $S(\tau)$ is the variance and τ is the period), spanning time periods of up to one or two days. In both studies, they found that the exponential term that best fit the variability was very nearly one. They found a linear relationship between the magnitude of the PW variability and time. A similar analysis on the spatial structure of water vapor was conducted by Emardson et al. [1998]. Using the Swedish GPS network (SWEPOS), they studied the structure of water vapor variance over scales of 10 to 100's of km and fit the variance according to a power law ($S(r) = cr^{\alpha}$, where r is the distance between stations). As was the case for the temporal variations, the structure function that worked best was one that varied linearly with distance (instead of some type of geometric scaling). These results differ somewhat from theoretical results discussed by Treuhaft and Lanyi [1987]. In their research, they assumed that the water vapor field should behave according to Kolmogorov turbulence theory. This theory implies that the variability of the water vapor structure function should behave according to a 5/3-power law over time scales less than a few minutes and space scales shorter than 1 km and smoothly transition into a 2/3-power law variation as the time and length scales increase.

Studies by Rocken et al., [1991] and Davis et al., [1993] observed variations in the PW content by scanning the sky at various elevation and azimuth angles. These investigations involved the use of MWR instruments that were configured so that they would measure the equivalent amount of PW in predefined directions, normally taking measurements at a specific elevation angle, and then stepping through a series of azimuth angles to observe the sky variability. These studies found that there can be azimuthal asymmetries as large as 25% of the total PW measurement. In the paper by Davis et al., they utilized a radiometer that measured the equivalent amount of PW in 10° azimuth steps at an elevation angle of 30°. For one particular example, they observed 5 mm of azimuthal PW variability with a mean estimate of approximately 20 mm. Assuming that most of the water vapor was contained within the first 2 km of the atmosphere, and a scanning elevation angle of 30°, the 5 mm of variability was distributed over a diameter of approximately 7 km.

2.5 Chapter Summary

Improved measurements of water vapor are needed in many topics of atmospheric research. Multiple reports and prospectuses highlight this need. Boundary layer studies require water vapor measurements to quantify the moisture convergence associated with convective rolls and drylines. Studies of convection initiation and severe storms show that accurate water vapor measurements improve the intensity and onset forecasting of storms. A detailed spatial and temporal sampling of atmospheric water vapor allows for improved statistical description of moisture to help validate and improve atmospheric models. The results of the research conducted in this thesis improve the observational capabilities available for all these topics.

Chapter 3: The Global Positioning System

3.1 Overview

The Global Positioning System is the most widely used constellation of satellites within the broader definition of Global Navigation Satellite Systems (GNSS). The GPS constellation is a United States Department of Defense (DoD) satellite system whose primary mission is to provide timing and ranging information to military users. Military applications of GPS include troop tracking and missile guidance systems. Civilian applications of GPS technology include land surveying, vehicle guidance and control, as well as high precision science [*Herring*, 1996]. There are three components to the GPS system: a space segment (the satellite constellation), a control segment (the network of monitoring and tracking stations which are operated by the military), and a user segment. For the user segment, GPS is designed to be a passive system. There is no interaction from the user segment to the satellite or control segment and there can be an infinite number of users of the system. There are numerous books describing the concepts of GPS. Notable to this list are works by Hofmann-Wellenhof et al. [1992], Kaplan [1996] and Parkinson et al. [1996]. This chapter reviews the key components of GPS that are relevant to this research. Those interested in pursuing a more detailed description of GNSS systems should refer to one of the references in the bibliography.

3.2 Satellite Constellation

Originally designed to be a constellation of 24 satellites, distributed in six orbital planes with four satellites in each plane, the current constellation consists of 28 satellites within the original six orbital planes. The characteristics of the satellite constellation are shown in Table 1. A list of satellites and their relative location within the constellation is available from the URL: ftp://tycho.usno.navy.mil/pub/gps/gpsb2.txt.

The constellation was designed to provide a global distribution of satellites so that at least four would be visible from any location on Earth. This minimum geometry allows for a unique and independent triangulation for position and time determination. With the current distribution, users at mid-latitudes are typically able to track at least six satellites at any moment.

Table 1: GPS Satellite Constellation Characteristics

Number of Satellites	24 (planned), 28 (current)
Number of Orbital Planes	6
Satellites per Orbital Plane	4
Orbital Period	~12 Hours
Orbital Radius	~26,400 Km
Inclination	~55°
Eccentricity	~0.0

3.3 GPS Signals and Observations

GPS satellites can be considered to be orbiting atomic oscillators. The fundamental frequency (f_0) of these oscillators is 10.23 MHz and all GPS signals are derived from f_0. GPS transmits on two L-band frequencies, generally referred to as the L_1 (1575.2 MHz or ~19 cm) and L_2 (1227.6 MHz or ~24 cm) carrier frequencies. Two different pseudorandom codes are modulated on top of the carrier frequencies. The first code is the Clear Acquisition code (C/A-code), which is only modulated on the L_1 carrier. Users of C/A-code observations are primarily civilians. The second code, known as the precise code (P-code), is modulated on both carrier frequencies and can be encrypted so that only military users have access to the signal. When encrypted, it is called the Y-code. Advanced civilian GPS receivers are now able to provide Y-code measurements, although at reduced accuracy compared to military receivers. Table 2 lists the characteristics of the basic GPS signals.

Table 2: GPS Signal Characteristics

Observation Name	Frequency Multiplier	Frequency	Wavelength	Precision
C/A	$f_0/10$	1.23 MHz	300 m	~10 m
P1 (Y1), P2(Y2)	$1* f_0$	10.23 MHz	30 m	~3 m
L1	$154* f_0$	1.23 MHz	19.0 cm	~ 1-2 mm
L2	$120* f_0$	1227.60 MHz	24.4 cm	~1-2 mm

The measurements of the pseudorandom codes (C/A, P_1, and P_2) are measures of the travel time between the satellite and receiver. The GPS receiver generates its own copy of the pseudorandom code and compares it to the one arriving from the satellite. An autocorrelation function computes the time offset between the received pseudorandom code and the one generated by the receiver. This offset is a combination of the time for the signal to travel from the satellite to receiver and the mis-synchronization of the satellite and receiver clocks. These measurements are called pseudorange measurements. Pseudorange measurements typically have a precision on the order of 1-10 meters.

In addition to the pseudorange, the two GPS carrier frequencies (L_1 and L_2) can also be used to make a phase measurement. In this method, the receiver first removes the pseudorandom codes from the carrier phase and combines the received signal with one generated internally using a phase lock loop (PLL) algorithm. The carrier frequency from the transmitting satellite is shifted when it arrives at the receiving GPS antenna. This Doppler shift is caused by the movement of the satellite relative to the receiving station. The integration of the synthesized signal output from the PLL represents the range (distance) between the satellite and receiver. The precision of this measurement is on the order of 1-2 mm. There is an ambiguity in this precise measurement. The receiver is not able to determine the initial distance to the satellite, it is only able to account for the change in range relative to the moment it begins tracking. To utilize the carrier phase, this ambiguity must be estimated in the inversion of the observation equations to derive station position, atmospheric delay and other geophysical properties.

The choice of L-band frequencies makes GPS an all-weather instrument. The tracking characteristics of the system are not dependent on atmospheric conditions (there is no significant attenuation), but the signal is delayed and bent according to the index of refraction of the atmosphere. A careful analysis of the GPS observations allows for the determination this delay and bending. These methods are the basis of atmospheric remote sensing with GPS and will be discussed in more detail in Chapter 4.

3.4 International GPS Service

The International GPS Service (IGS) is a volunteer collection of research groups, mainly consisting of government agencies and participating universities. Their goal is to provide high quality data and products for use in high precision science applications. The key components of the IGS include a network of continuously operating GPS stations, data centers who collect and distribute data through the Internet, analysis centers who produce products based on data collected from the network, and a governing body (including working groups and a central bureau) to guide the development and progress of the IGS.

The IGS collects data from more than 360 stations worldwide. Of these stations, 130 are considered global stations. The IGS definition of a global station is one whose data is used by more than three analysis centers, with one of the centers being located on a different continent than the station. The list of global stations is a compromise between location, distribution with respect to other stations, the latency of the data availability, and other issues such as receiver tracking performance and monument stability. A map of the "global" stations is plotted in Figure 1. This network is the backbone of the IGS and is the basis for which it generates its products. Individual institutions voluntarily operate and contribute the data collected by their station to the IGS for analysis.

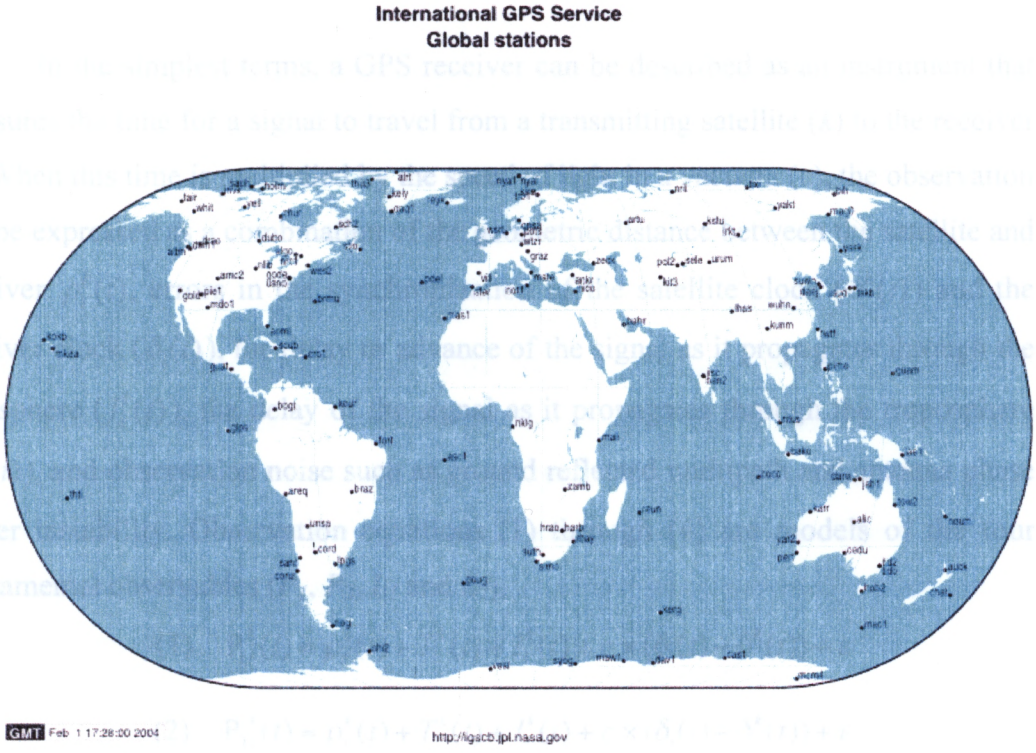

Figure 1: Map of "global" IGS stations (http://igscb.jpl.nasa.gov)

The data collected from the global stations are used by the analysis centers to compute products for general scientific use. A list of IGS products is shown in Table 3.

Table 3: IGS Derived Data Products

IGS Product Type	Accuracy (units)	Comment
Satellite Ephemeredes	2 (cm)	Final orbits available with about 2 week latency
Earth Rotation Parameters	0.05 (mas) Polar Motion 0.02 (ms) Length of Day	Polar Motion, Polar Motion Rate, and Length of Day.
Zenith Tropospheric Path Delay	4 (mm) Zenith Path Delay	ZTD at IGS global stations estimated with 2-hour time steps.
Total Electron Content	2-8 (TECU)	Global grid with 5° x 2.5° resolution
Geocentric Coordinates and Velocities	3 (mm) horizontal 6 (mm) vertical	Referenced to the ITRF

3.5 Observation Equation

In the simplest terms, a GPS receiver can be described as an instrument that measures the time for a signal to travel from a transmitting satellite (k) to the receiver (i). When this time is multiplied by the speed of light in a vacuum (c), the observation can be expressed as a combination of the geometric distance between the satellite and receiver $\rho_i^k(t)$, errors in the synchronization of the satellite clock ($\delta^k(t)$) and the receiver clock ($\delta_i(t)$), the delay or advance of the signal as it propagates through the ionosphere ($I_i^k(t)$), the delay of the signal as it propagates through the troposphere ($T_i^k(t)$), and observation noise such as ground reflected multipath and antenna phase center instability. Observation equations (1) through (4) are models of the four fundamental observables (P_1, P_2, L_1 and L_2).

$$(1)\quad \mathrm{P}_{1i}^k(t) = \rho_i^k(t) + T_i^k(t) + I_i^k(t) + c \times (\delta_i(t) - \delta^k(t)) + \varepsilon$$

$$(2)\quad \mathrm{P}_{2i}^k(t) = \rho_i^k(t) + T_i^k(t) + I_i^k(t) + c \times (\delta_i(t) - \delta^k(t)) + \varepsilon$$

$$(3)\quad L_{1i}^k(t) = \rho_i^k(t) + N_{1i}^k\lambda_1 + T_i^k(t) - I_i^k(t) + c \times (\delta_i(t) - \delta^k(t)) + \varepsilon$$

$$(4)\quad L_{2i}^k(t) = \rho_i^k(t) + N_{2i}^k\lambda_2 + T_i^k(t) - I_i^k(t) + c \times (\delta_i(t) - \delta^k(t)) + \varepsilon$$

The carrier phase equations (L_1 and L_2) include a term ($N_{f_i}^k$) called the ambiguity. This ambiguity was discussed previously in the section on GPS signals. It represents the distance between the satellite and receiver when it begins tracking the satellite. The affect of the ionosphere is opposite in sign for the pseudorange measurements (P_1 and P_2) and carrier phase measurements (L_1 and L_2). The ionosphere induces a delay of the signal in pseudorange measurements and an advance of the carrier phase. This difference in sign is related to the phase and group velocity of the microwave signal as it passes through the ionosphere.

3.6 Linear Combinations of Observations

The pseudorange and carrier phase observables (P_1, P_2, L_1 and L_2), expressed in units of distance (meters), can be linearly combined to eliminate and isolate certain

components of the observation equation. For instance, a linear combination can be formed to remove the effect of the ionosphere. Similarly, a linear combination can be formed that isolates the ionosphere. These combinations are listed below, followed by a brief description.

$$(5) \quad L_3 = \frac{1}{f_1^2 - f_2^2}(f_1^2 L_1 - f_2^2 L_2)$$

Equation (5) eliminates the phase advance of the ionosphere on the carrier phase observables. The disadvantage of this linear combination is that the noise from the L_1 and L_2 carrier phase measurements is increased by nearly a factor of three. For receivers that have dual frequency capability, the L_3 combination is usually the preferred method to use in geodetic and atmospheric applications. The only times when L_1 or L_2 observations are used individually are when networks of stations are operated over such short distances that ionospheric effects can be eliminated through differencing or other methods.

$$(6) \quad L_4 = L_1 - L_2$$

Equation (6) differences away the geometric, tropospheric, and clock synchronization components of the carrier phase equation. The effect of the ionosphere and the ambiguities remain. This linear combination is used to estimate global, regional, and high resolution ionosphere models [*Rocken et al.*, 2000].

$$(7) \quad L_5 = \frac{1}{f_1 - f_2}(f_1 L_1 - f_2 L_2)$$

Equation (7) is called the widelane linear combination. The combined wavelength of L1 and L2 carrier phase measurements is 84 cm. This long wavelength simplifies ambiguity resolution. It is commonly used in the analysis of stations that are separated by more than a few tens of km.

3.7 Differences of Observations

In addition to the linear combinations of different observables, observations from pairs of stations and satellites can be differenced. Differencing is commonly used to eliminate satellite and receiver clock errors. The three most common

differencing equations used are the single difference, the double difference and the triple difference. A single difference observation is the combination of observations from two stations and one satellite. It is used to eliminate the receiver clock errors.

$$(8) \quad L_{Fi,j}^{k} = L_{Fi}^{k} - L_{Fj}^{k}$$

A double difference is the difference of two single differences. It is the combination of observations from two stations and two satellites. In this combination, satellite clocks are eliminated.

$$(9) \quad L_{Fi,j}^{k,l} = L_{Fi,j}^{k} - L_{Fi,j}^{l}$$

A third combination is the triple difference; it is the time derivative of sequential double difference observations (equation (9)). It is primarily used to check for continuous carrier phase observations. These breaks are known as cycle slips and must be identified, repaired, and/or removed to ensure accurate modeling of the observations.

3.8 GPS Analysis Software

There are only a handful of GPS software packages available for atmospheric and geodetic scientific applications. The most commonly used packages are GAMIT [*King and Bock*, 2002], GIPSY [*Zumberge et al.*, 1997], and Bernese [*Hugentobler et al.*, 2001]. GAMIT uses the double difference measurement as the fundamental observable. GIPSY uses the un-differenced one-way phase measurement. Bernese can analyze data using both un-differenced and double differenced observations. As mentioned earlier, differencing removes satellite and receiver clock errors. In order for GIPSY and Bernese to use un-differenced observations, the software estimates the clock errors as additional random walk parameters.

Although the software packages are different in terms of the types of observations used (un-differenced or double-differenced) and in the implementation of the estimator (Kalman filter, or Least Squares Estimator), they all use a similar method in designing the inversion problem. First, the observations (y_i, i = 1, n) are collected into a single column matrix (**y**). The observations could be one-way observations, differenced observations, or linear combinations of observations. The

observation model is then linearized about some a priori state ($\mathbf{x_0}$) using a Taylor expansion.

$$(10)\quad \mathbf{y} = \mathbf{y}(\mathbf{x_0}) + \mathbf{A}\mathbf{x}$$

$$(11)\quad \mathbf{l} = \mathbf{y} - \mathbf{y}(\mathbf{x_0}) = \mathbf{A}\mathbf{x}$$

The apriori state vector is a column matrix of the parameters that will be estimated from the observations. It consists of any and possibly all components of the observation model represented in equations (1) - (4). Common parameters that are estimated include station position, satellite orbital elements, ambiguities, satellite and receiver oscillator offsets, and tropospheric delays. The matrix **A** represents the Jacobian, or matrix of partial derivatives, of the observation model with respect to the state vector.

$$(12)\quad \mathbf{A} = \begin{bmatrix} \delta y_1(x_o)/\delta x_1 & \delta y_1(x_o)/\delta x_2 & \cdots & \delta y_1(x_o)/\delta x_m \\ \delta y_2(x_o)/\delta x_1 & \ddots & & \\ \vdots & & \ddots & \\ \delta y_n(x_o)/\delta x_1 & & & \delta y_n(x_o)/\delta x_m \end{bmatrix}$$

The software used in the research presented here is Bernese. It uses the method of weighted least squares [*Strang*, 1988] to solve equation (11). With this method, the solution of the system (**x**) that minimizes the variance of the residuals is given by the following equation.

$$(13)\quad \mathbf{x} = (\mathbf{A}^T\mathbf{P}\mathbf{A})^{-1}\mathbf{A}^T\mathbf{P}\mathbf{l}$$

The matrix **P** represents the weighting matrix of the observations and can be diagonal or have off diagonal terms that represent the correlations between parameters. Since the original observations were first linearized, the estimate is only the improvement to the a priori state (**x**). The a priori and the estimate must therefore be combined.

$$(14)\quad \hat{\mathbf{x}} = \mathbf{x_0} + \mathbf{x}$$

The residuals (**r**) to the solution can also be computed.

$$(15) \quad \mathbf{r} = \mathbf{Ax} - \mathbf{l} = \mathbf{Ax} - (\mathbf{y} - \mathbf{y}(\mathbf{x}_0))$$

They represent the un-modeled component, if any, of the observation equation and measurement noise. Because of the statistical properties of Least Square Estimation algorithms, these residuals will be zero mean and have a Gaussian distribution. This is an important point, and one that will be utilized in the retrieval of SW.

3.9 Other GNSS Systems

While GPS is the largest and most complete GNSS system, there are others including the now decommissioned TRANSIT system, the Russian GLONASS system, and there are plans for a European Union system named Galileo [*Lachapelle et al.*, 2002]. The TRANSIT system consisted of six satellites, with a nearly circular orbit whose radius was approximately 1100 km. The TRANSIT system was decommissioned in 1996. The GLONASS and proposed Galileo constellations are similar to GPS in their use of L-band frequencies, and orbital parameters. In fact, combined GPS-GLONASS systems are now available and the IGS is computing GLONASS based products such as satellite orbits and time transfer information. The GLONASS system has been severely limited due to the lack of available funds within the Russian government, but the constellation is still in operation and does provide reliable data. The Russian government recently made a commitment to continue funding and support of the constellation and it appears that it will undergo an expansion in the upcoming years. The Galileo constellation is being principally funded by the European Union (with some support from China and other countries) as an alternative to GPS, whose program operation is controlled by the United States Department of Defense. It should be noted that the Galileo system is being designed to work in harmony with GPS, which provides the possibility to double the number of satellites available to users. This is a positive development for atmospheric sensing with GNSS systems in that it will allow a denser sampling of the atmosphere.

Chapter 4: Slant Water Vapor

4.1 Overview

Slant water vapor is the integral amount of water vapor along the path between two points. When used in the context of GPS, these two points are the transmitting satellite and the receiving antenna. The development and validation of GPS SW retrieval techniques is presented in this chapter. To make the chapter more complete, the retrieval of precipitable water vapor and its relationship to atmospheric delay is described first. The development and validation of SW has lead to two published manuscripts [*Braun et al.*, 2003; *Braun et al.*, 2001]. They are included as appendices and summarized here. In addition, a simulation experiment is presented to illustrate the capabilities and limitations of the techniques used to measure SW.

4.2 The Neutral Atmosphere and GPS

The technique of measuring atmospheric water vapor with GPS relates the delay and bending of a GPS signal as it propagates through the atmosphere to the integral of the water vapor density. The excess delay (ΔL) caused by the neutral atmosphere can be expressed as the integral of the refractivity ($N(s)$) along the path (S) between the transmitting GPS satellite and the receiving GPS antenna.

$$(16) \quad \Delta L = 10^{-6} \int_S N(s) ds + S - G$$

The term excess delay describes the additional delay of a signal when compared to one propagating through a vacuum (G). Refractivity is related to the index of refraction (n).

$$(17) \quad N = 10^6 (n - 1)$$

The refractivity is a function of atmospheric pressure (p, expressed in millibars), vapor pressure (e_w, in millibars) and temperature (T, in Kelvin) and is approximated by equation (18) [*Smith and Weintraub*, 1953].

$$(18)\quad N \approx 77.6(\frac{P}{T}) + 3.73\times 10^5(\frac{e_w}{T^2})$$

This relationship between refractivity and atmospheric composition is considered accurate to approximately 0.5%. See Bevis et al., [1992] and Bevis et al., [1994] for further discussion on the mathematical expression of refractivity. Substituting equation (18) into equation (16) yields the following integral.

$$(19)\quad \Delta L = 10^{-6}\int_S \left[77.6(\frac{P}{T}) + 3.73\times 10^5(\frac{e_w}{T^2})\right]ds + S - G$$

If atmospheric bending is ignored, a reasonable assumption for satellites above 5° elevation angle [*Sokolovskiy et al.*, 2001], Equation (19) can be simplified to contain only the integral of refractivity.

$$(20)\quad \Delta L = 10^{-6}\int_S \left[77.6(\frac{P}{T}) + 3.73\times 10^5(\frac{e_w}{T^2})\right]ds$$

The delay described by the first term in the integral is called the slant hydrostatic delay (SHD). The second term is known as the slant "wet" delay (SWD). The summation of the two is the slant total delay (STD=SHD+SWD). Equation (19) represents the T_i^k term in observation equations (1)-(4).

The integral in equation(19) is dependent on both the atmospheric composition and the path of the signal. As the elevation angle of a satellite decreases, the length of the path through the neutral atmosphere increases. Scaling the slant path delay to its equivalent delay if the satellite was at zenith is expressed below.

$$(21)\quad ZTD = ZHD + ZWD = \frac{SHD}{m_h(\theta)} + \frac{SWD}{m_w(\theta)}$$

Where ZTD is the zenith total delay, ZHD is the zenith hydrostatic delay, and ZWD is the zenith-wet delay. ZTD is equivalent to the vertical integral of equation (19). ZHD and ZWD are the vertical integrals of each component of equation (19). The terms $m_h(\theta)$ and $m_w(\theta)$ are called the hydrostatic mapping function and the wet mapping function. Analytic expressions of these mapping functions have been formulated by Davis et al. [1985] and Niell [1996]. They are based on the continued fraction of 1/sin(θ).

$$(22)\quad m(\theta)=\frac{\dfrac{1}{1+\dfrac{a}{1+\dfrac{b}{1+c}}}}{\sin(\theta)+\dfrac{a}{\sin(\theta)+\dfrac{b}{\sin(\theta)+c}}}$$

In the case of Niell, the coefficients in equation (22) were computed by ray tracing through the U.S. Standard Atmosphere. These coefficients vary as a function of station latitude, day of year, and altitude. Rocken et al [2001] and Niell [2001] developed a method where the mapping function is computed for a specific time and location using a numerical weather model. The advantage of this "direct mapping" or "dynamic mapping" should be in its improved representation of current atmospheric conditions.

Hydrostatic and wet mapping functions are similar but not identical. The wet mapping function is slightly larger and much more variable. The difference is related to the scale heights of water vapor (2-3 km) and the neutral atmosphere (closer to 8 km). At 10° elevation angle, the hydrostatic mapping function is between five and six. At 5° elevation it is approximately 10.

In standard GPS analysis packages, the tropospheric delay is assumed to be adequately defined with either a time varying zenith value that is the same for all satellites, or a time varying delay with an additional linear horizontal gradient [*Bar-Sever et al.*, 1998; *Davis et al.*, 1993]. The ZHD can be computed using a surface pressure measurement [*Davis et al.*, 1985; *Saastamoinen*, 1972] and can be scaled to a SHD using the $m_h(\theta)$ mapping function.

The amount of water vapor in the atmosphere is poorly correlated to surface humidity measurements. Therefore, the ZWD (and therefore SWD) cannot be accurately computed using surface measurements. ZWD is therefore included as an estimated parameter in the inverse modeling of the observation equations [*Rocken*, 1988]. The output of the estimation results in a time varying ZWD value that represents the following integral.

$$(23)\quad ZWD=(3.73x10^5)(10^{-6})\int\frac{e_w}{T^2}dz=(3.73x10^5)(10^{-6})R_v\int\frac{\rho_v}{T}dz$$

Where R_v is the gas constant for water vapor and ρ_v is the water vapor density.

4.3 Scaling ZWD to PW

Precipitable water (PW) is defined as the integrated water vapor density (IWV) divided by the density of liquid water. The path of the integral is in the zenith direction, directly above a location.

$$(24)\quad PW = \frac{1}{\rho} IWV = \frac{1}{\rho}\int \rho_v dz = \frac{1}{\rho R_v}\int \frac{e_w}{T} dz$$

The units of IWV are typically expressed as (kg/m^2). The units of PW are expressed as millimeters of liquid water. The ratio of equations (23) and (24) can be computed and simplified.

$$\Pi = \frac{PW}{ZWD} = \frac{\frac{1}{\rho R_v}\int \frac{e_w}{T} dz}{\left(3.73\times 10^5\right)\left(10^{-6}\right)\int (e_w/T^2) dz} = \frac{1}{0.373 \rho R_v} T_m$$

(25) where

$$T_m = \frac{\int \frac{e_w}{T} dz}{\int \frac{e_w}{T^2} dz} = \frac{\int \rho_v dz}{\int \frac{\rho_v}{T} dz}$$

The ratio of the two vertical integrals in (25) is called the weighted "mean temperature" T_m. Bevis et al. [1992] used approximately 9,000 radiosonde observations from the United States to derive a relationship between T_m and surface temperature (T_s).

$$(26)\quad T_m = 70.2 + 0.72 \times T_s$$

Using Equation (26) for locations within the continental United States should yield T_m values that are accurate to approximately 2%. Equation (27) provides a simple relationship to scale the estimated GPS quantity of ZWD to PW.

$$(27)\quad PW = \frac{IWV}{\rho} = \Pi \bullet ZWD$$

The ratio of PW to ZWD is typically somewhere near 0.15. This implies that a PW value of 1 mm will correspond to a ZWD of 6.5 mm.

The methods described above have been used extensively to show that GPS is an accurate, all-weather, instrument for measuring PW [*Rocken et al.*, 1995; *Rocken et al.*, 1997]. Instruments like microwave water vapor radiometers (MWR) are able to measure PW with better than 5% accuracy [*Revercombe et al.*, 2003]. Comparisons between GPS and MWRs indicate their agreement to approximately 5%. In an absolute comparison, this represents a root mean square agreement of 1.5 mm for stations in mid-latitudes where PW amounts commonly range from 10-50 mm and average around 30 mm. Comparisons of GPS PW to data collected from radiosondes also show agreement of approximately 1.5 mm or better. For a mid-latitude, continental location, PW values can range between 10 and 50 mm throughout a year.

The relatively good agreement between GPS and MWR techniques is encouraging in that the fundamental physics in the two methods are different. An MWR relies on the emission of radiation from atmospheric water vapor to derive a brightness temperature measurement, which is then related to PW. GPS relates path delay to PW. In addition to the different physical principles implemented in the retrieval methods, there is another difference between PW derived from an MWR and GPS. The two instruments sample vastly different volumes of atmosphere. The beam width of an MWR is between 5° and 10°. The small solid angle associated with this narrow beam width ensures that an MWR provides a true measure of the water vapor directly over an instrument. This is in contrast to GPS. GPS software packages frequently use all observations collected above an elevation angle of 5° or 10°. This low elevation mask creates a volume of atmosphere that is quite large and often times contain significant variations. When there is significant variability in water vapor amounts, the GPS PW estimate might not accurately represent what is directly above a station. Enhancing the GPS method to resolve the water vapor amount in each satellite direction provides the opportunity to characterize the atmosphere in a more detailed and precise manner. This leads to the concept of SW.

4.4 Slant Water Vapor Retrieval

The method of using GPS to estimate PW is described above. To summarize, a GPS receiver measures the elapsed time for a signal to propagate from a satellite to

the receiving antenna. As part of this travel time, the signal is delayed and bent by the atmosphere. A portion of this atmospheric delay, the hydrostatic portion, can be calculated and removed using a surface pressure measurement. The remaining portion of the delay, which corresponds to the wet component of the excess delay, is estimated as a parameter in the inversion of the observation equations. This inversion assumes that the wet delay to all satellites can be accurately modeled using a time varying zenith parameter that is scaled to the elevation angle of the satellite by a mapping function $m_w(\theta)$. Most GPS analysis packages try to improve on this simple, horizontally homogeneous, model with the additional estimation of horizontal atmospheric gradient terms [*Bar-Sever et al.*, 1998; *Davis et al.*, 1993]. While gradients do provide some increased spatial resolution of the water vapor fields, the atmospheric structure is often times highly variable and cannot accurately be described with this simple linear model. This has been confirmed in a recent analysis by Aonashi [2004] which indicates that when estimating horizontal gradients with a pointing MWR, the residuals from the estimate represent a larger portion of the azimuthal variability than the estimated gradient term.

At first glance, it seems that the optimal method of determining SW would be to estimate it directly during the inversion of the observation equations. This is not possible using traditional, over-determined least squares techniques. The estimation of station coordinates and ambiguities makes the independent parameterization of rapidly changing delays in the direction of individual satellites impossible. If this method were implemented, it would lead to a parameterization with an underdetermined set of linearly independent observations. This is especially true when satellite and receiver clock errors are not removed through double differences. Instead, the retrieval of SW combines the ZWD estimate and the un-modeled residuals (S_i^k) from the estimation to create the slant-wet delay. The SWD is scaled to SW through the same Π factor that is used to scale ZWD to PW. The expression of SW can be represented by equation (28).

$$(28) \quad SW_i^k = \Pi \times (m_w(\theta) \times ZWD + S_i^k)$$

The term (S_i^k) corresponds to the residual that is saved in the estimation step and is equivalent to **r** in equation (15). If the observations are accurately modeled, and the estimated parameters are not biased, the residuals contain information on how the model differs from the actual observations. By constraining the estimate of the station coordinates to precisely determined values, resolving ambiguities, and using precise IGS satellite orbit products, the parameter that is modeled most inaccurately is the ZWD parameter. The resulting residuals then contain information on how well (or poorly) the observations matched the model. If the residual of an observation is negative, the ray to that satellite path passes through atmosphere that contains less water vapor compared to the mapped ZWD estimate. If the residual is positive, it represents a ray that traveled through a volume of atmosphere that is wetter than the ZWD estimate. Combining the ZWD value with the residual produces the SW value.

The use of double difference observations eliminates the errors associated with satellite and receiver clock errors. This makes the double difference observation more accurate than one between a single satellite and receiver. However if there are N ground stations, and M satellites at any instance in time, there can only be (N-1) x (M-1) linearly independent double difference observations. The direct transformation from double-difference residuals to one-way residuals is therefore impossible. The use of constraints has been used to unwrap the double difference residuals into so called "zero difference" residuals. The term "zero difference" is used because they are derived from double difference residuals. The transformation of double-difference residuals to zero difference residuals is described in Alber et al. [2000].

The steps involved in transforming GPS observations into estimates of SW are diagramed in Figure 2. The GPS observations are collected and stored in individual files grouped by station. The observations are combined into double differences to remove satellite and receiver clock errors. These double differences are scanned (by computing the time derivative) for data outliers and blunders. Where possible, the double difference observations are repaired. Once outliers have been edited and repaired, the double difference observations are used as input in the parameter estimation routine. Initially, the observations are processed by individual baseline (all observations between two stations) to resolve carrier phase ambiguities. Ambiguities

are estimated as parameters (first using the L_5, then the L_3 linear combination) and stored with the observations so that they can be reintroduced as known values later. Ambiguities are solved in a separate step because they are essentially nuisance parameters that are not correlated between stations. In the final analysis step, the following parameters are estimated: station coordinates, unresolved phase ambiguities, and zenith wet troposphere delays. The station coordinate parameters are tightly constrained to the previous week's coordinate solution. Constraining the coordinates to these accurate a priori values improves the estimation of the ZWD parameters. Once the ZWD values are estimated, they are used as input to compute the un-modeled double difference residuals. These residuals are stored and inverted into one way residuals using the zero mean assumptions [*Alber et al.*, 2000]. The ZWD values and the zero difference residuals are then combined to create SWD values that can be scaled to SW using the Π factor.

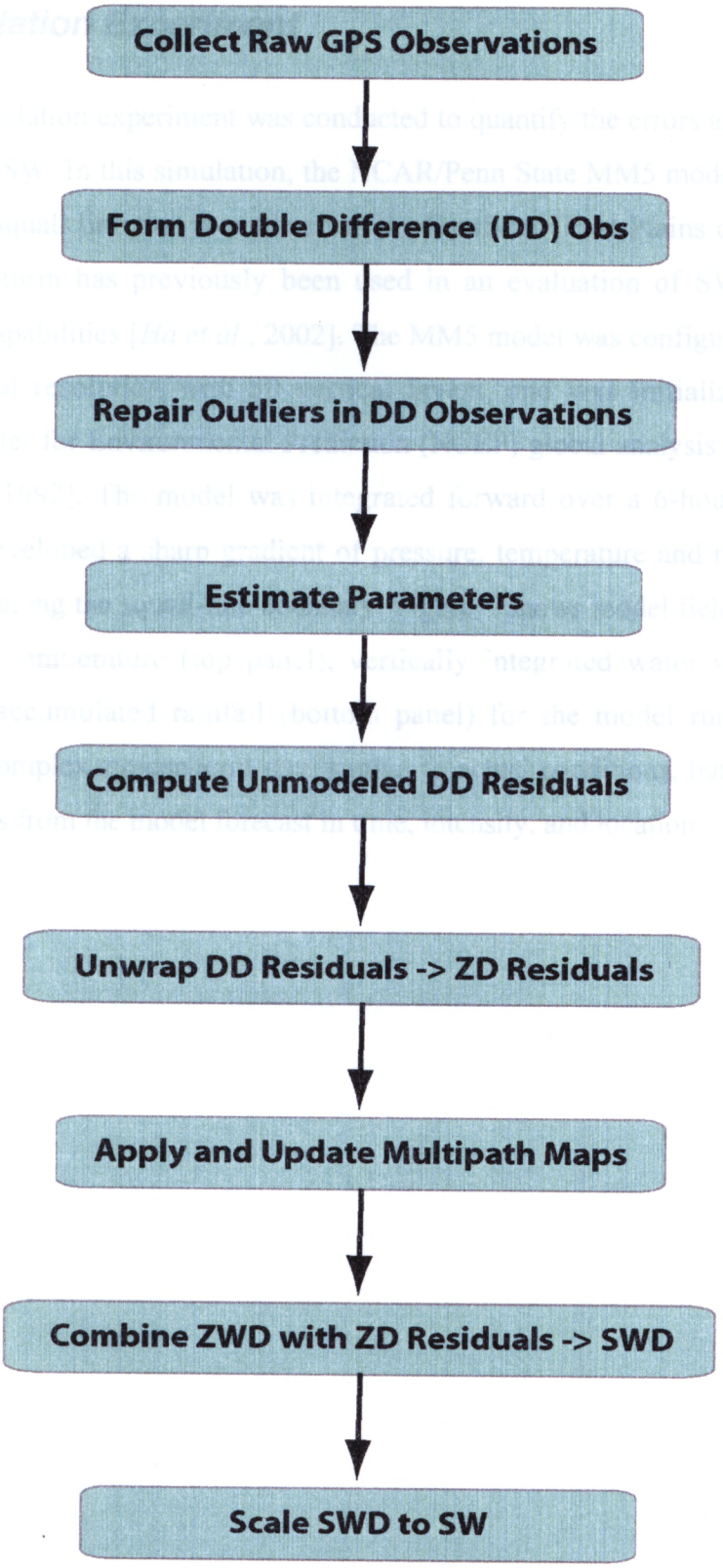

Figure 2: Diagram of processing steps in the computation of GPS SW.

4.5 Simulation Experiment

A simulation experiment was conducted to quantify the errors associated with GPS derived SW. In this simulation, the NCAR/Penn State MM5 model was used to reproduce a squall line that moved across the Southern Great Plains on October 30 1999. This storm has previously been used in an evaluation of SW to improve forecasting capabilities [*Ha et al.*, 2002]. The MM5 model was configured to run at 3 km horizontal resolution with 50 vertical layers, and was initialized using the National Center for Environmental Prediction (NCEP) global analysis field [*Parrish and Derber*, 1992]. The model was integrated forward over a 6-hour period. The squall line developed a sharp gradient of pressure, temperature and moisture, with rain forming along the squall-line boundary. Figure 3 shows model fields of sea level pressure and temperature (top panel), vertically integrated water vapor (middle panel), and accumulated rainfall (bottom panel) for the model run. The model generates a complex atmospheric state similar to actual conditions, but the observed rainfall differs from the model forecast in time, intensity, and location.

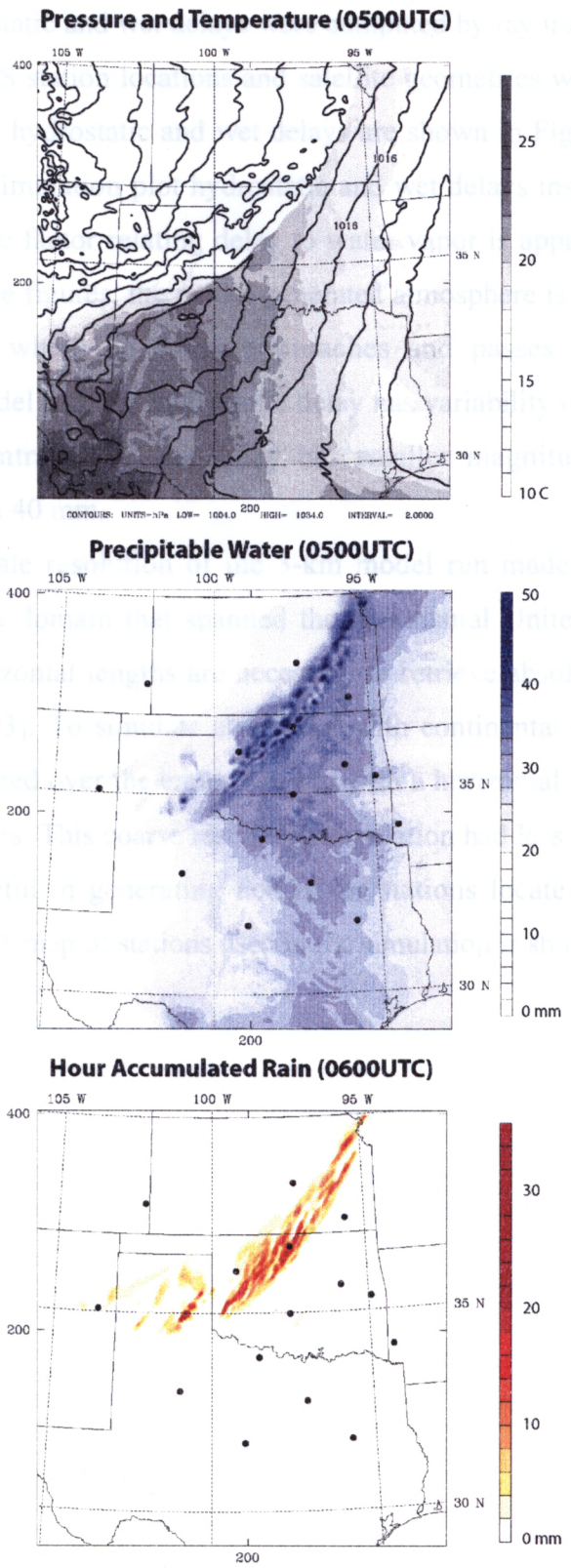

Figure 3: Model output fields used in the SW simulation – pressure and temperature (top), precipitable water (middle), hourly accumulation of rainfall (bottom).

Slant hydrostatic and wet delays were computed by ray tracing through model fields. Realistic GPS station locations and satellite geometries were used. Examples of the zenith scaled hydrostatic and wet delays are shown in Figure 4 and Figure 5. All figures in this simulation plot hydrostatic and wet delays instead of SW or PW. Recall that the scale factor relating delay to water vapor is approximately 0.15. As can be seen from the figures, the model-generated atmosphere is quite variable. This is especially true when the storm approaches and passes over each station. Throughout the model run, the hydrostatic delay has variability of less than 5 mm at any instant. In contrast, the wet delay has smaller magnitude, but displays a variability of almost 40 mm.

The fine scale resolution of the 3-km model run made it computationally difficult to create a domain that spanned the continental United States. Networks spanning large horizontal lengths are necessary to retrieve absolute ZWD estimates [*Rocken et al.*, 1993]. To simulate a network with continental coverage, a second model run was created over the entire US, but with a horizontal resolution of 25 km and 23 vertical layers. This coarse resolution simulation had less variability in model fields, but was useful in generating delays for stations located outside the 3 km resolution domain. A map of stations used in the simulation is shown in Figure 6.

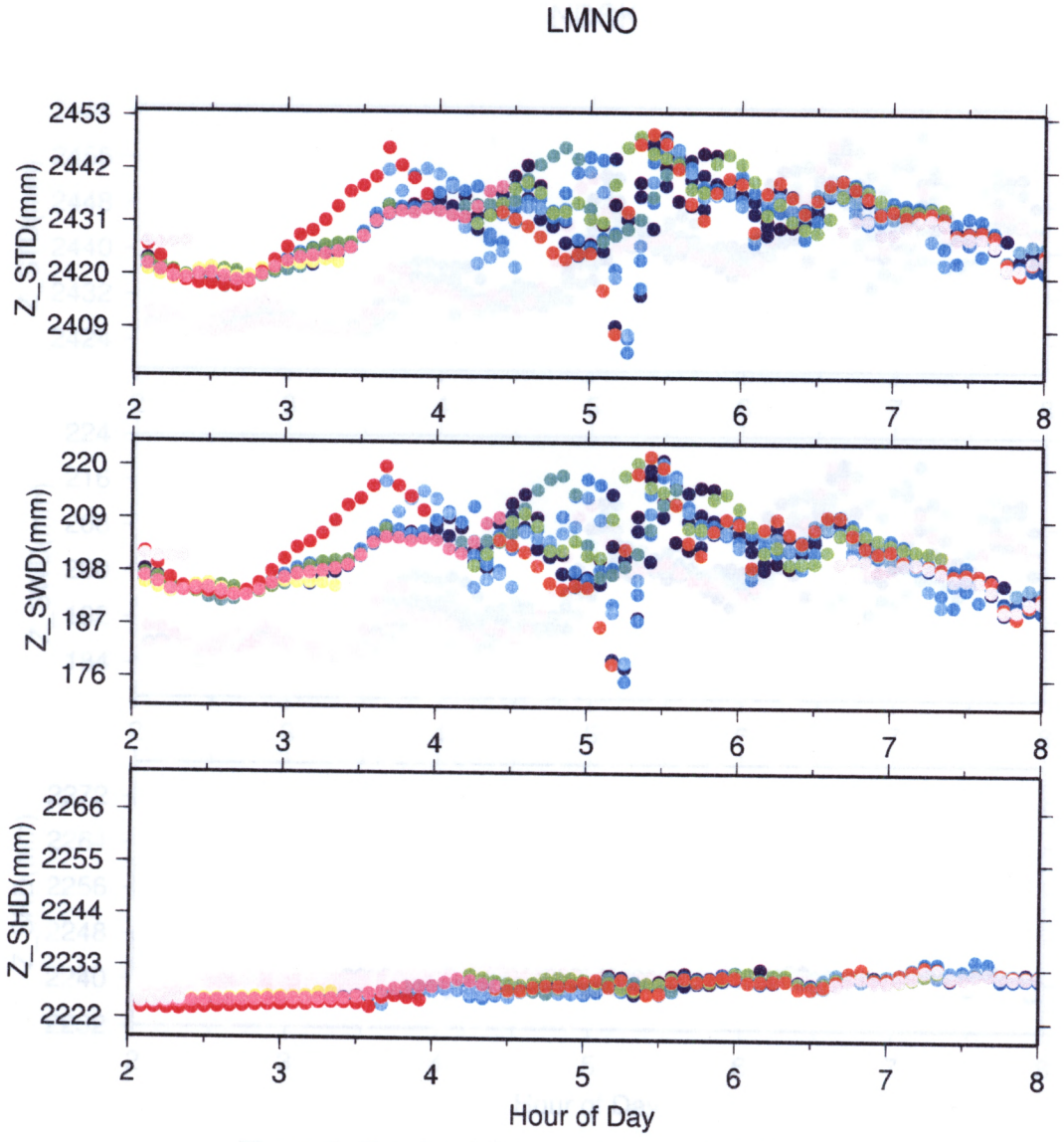

Figure 4: Simulated, zenith scaled, hydrostatic delay (lower), wet delay (middle), and total delay (upper). Each color represents a different satellite.

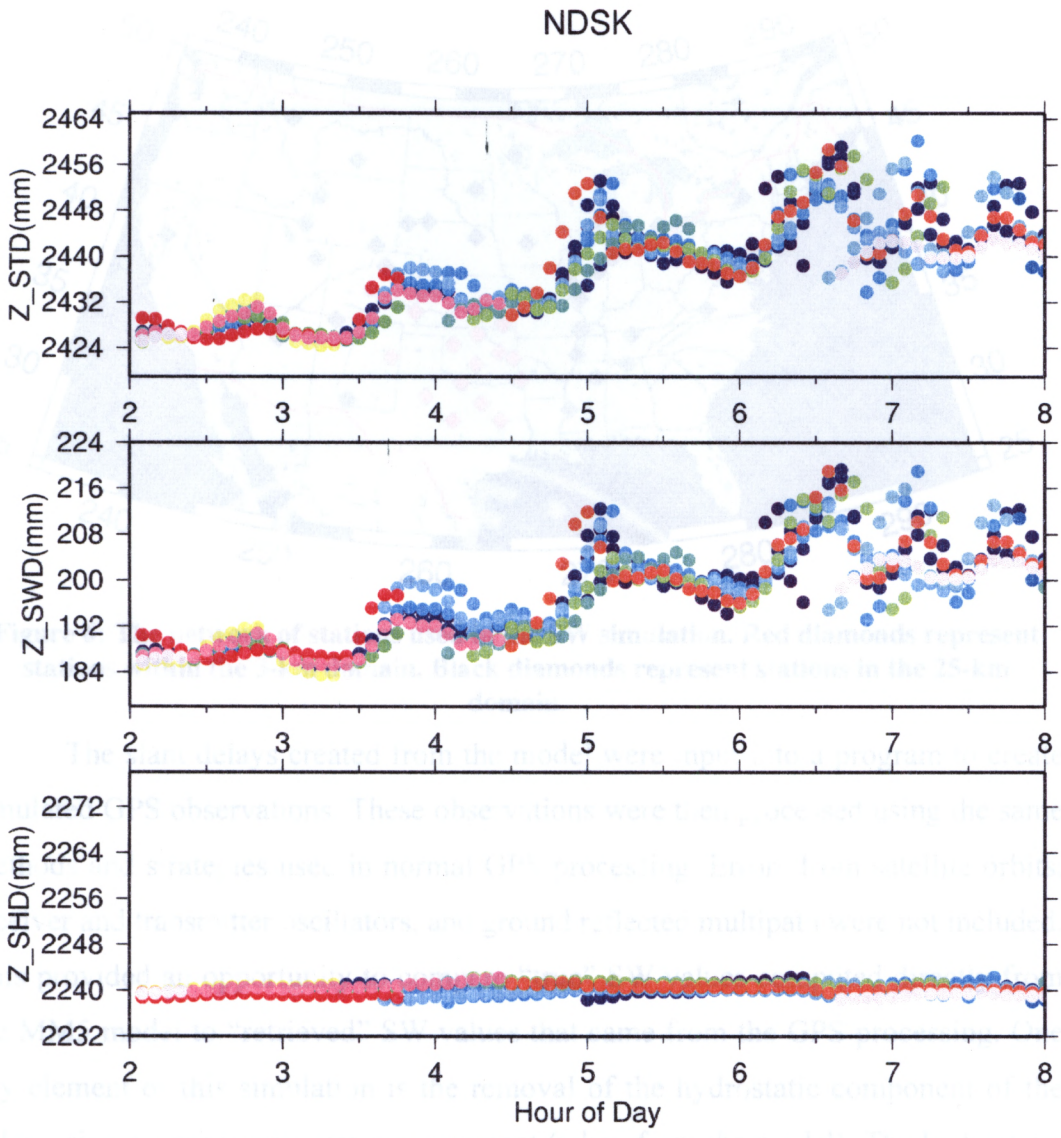

Figure 5: Simulated delays for station NDSK.